SUBCOOLED FLOW BOILING OF FLUOROCARBONS

R. W. Murphy
A. E. Bergles

Report No. DSR 71903-72

International Business Machines Corp.
Poughkeepsie, New York

Engineering Projects Laboratory
Department of Mechanical Engineering
Massachusetts Institute of Technology
Cambridge, Massachusetts 02139

January 1971

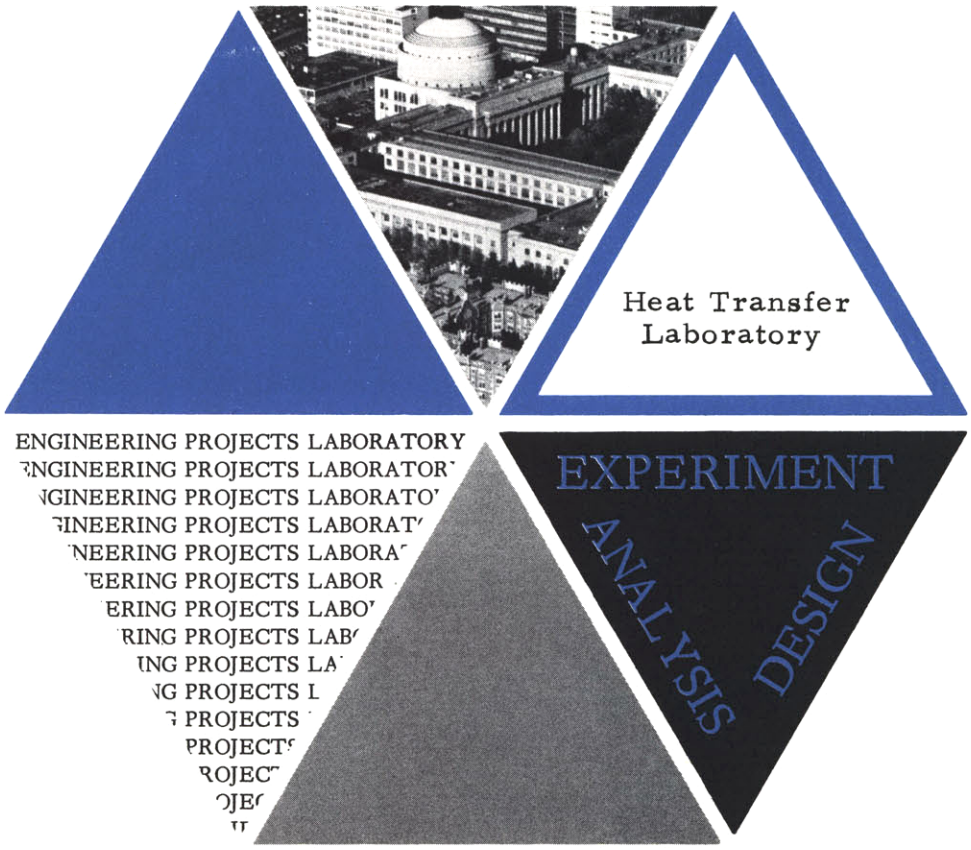

TECHNICAL REPORT NO. 71903-72

SUBCOOLED FLOW BOILING OF FLUOROCARBONS

Richard W. Murphy
Arthur E. Bergles

for

Heat Transfer Development Laboratory
Systems Development Division
International Business Machines Corporation
Poughkeepsie, New York 12602

January 1971

DSR Projects 71340 and 71903

Heat Transfer Laboratory
Engineering Projects Laboratory
Department of Mechanical Engineering
Massachusetts Institute of Technology
Cambridge, Massachusetts 02139

ABSTRACT

A study was conducted of heat transfer and hydrodynamic behavior for subcooled flow boiling of Freon-113, one of a group of fluorocarbons suitable for use in cooling of high-power-density electronic components. Problems arising from the excellent wetting characteristics and large solubility constants of fluorocarbons were also examined. The primary configuration was vertical upflow through a 0.500-in. ID stainless steel tube with direct resistance heating of the tube wall. Operating parameter ranges included up to 4.28 ft/sec velocity, 22.3 psia pressure, 61°F subcooling, 0.40 void fraction, 1.08×10^{-3} moles/mole dissolved gas, and 10^5 Btu/hr ft^2 heat flux.

Single-phase heat transfer was adequately correlated by standard methods. Boiling curves had a unique form dominated by large, discontinuous jumps in wall temperature at the incipient point on increasing heat flux traverses. Effects of velocity and subcooling on two-phase heat transfer followed conventional trends. Techniques were devised for accurate determination of the temperature dependence of the air-Freon-113 solubility constant and for measurement and control of dissolved gas content in the main loop. Dissolved gas effects were found to increase heat transfer significantly in the partial boiling mode. Data in the fully-developed boiling mode were successfully described by modifications of existing correlations. A conventional correlation provided, at best, an upper bound for the critical heat flux data. Models and analyses were formulated for predicting delayed nucleation and dissolved gas effects on incipience. Delayed nucleation and hysteresis were successfully eliminated by means of a special surface coating. Transition in gassy boiling heat transfer from gas-dominated to vapor-dominated modes was postulated with reference to adjusted saturation temperatures.

Single-phase pressure drop was adequately correlated by standard methods. Parametric effects on two-phase total pressure drop were investigated and described. Three novel techniques--photographic, trap, and capacitance--were employed to obtain accurate void fraction measurements. It was found that dissolved gas drastically retarded bubble collapse rates. Parametric effects on void fraction were examined and approximately correlated on quality coordinates. Modification of an existing analysis for predicting the point of net vapor generation gave reasonable agreement with void data. Void information was used to estimate the gravity component of pressure drop. The remaining friction-acceleration component data were plotted on coordinates suggested in an existing correlation. Alteration of the coordinates to account for dissolved gas resulted in fair agreement of data with the correlation curve. A qualitative description of the gas-dominated to vapor-dominated transition in pressure drop performance, analogous to that for heat transfer, was developed.

ACKNOWLEDGMENTS

This study was sponsored by the Heat Transfer Development Laboratory, Systems Development Division, International Business Machines Corporation, Poughkeepsie, New York. Mr. Richard C. Chu and Mr. John H. Seely, representing the sponsors, provided assistance throughout the investigation.

Professors Warren Rohsenow, Peter Griffith, and Kenneth Smith have given generously of their time to offer helpful suggestions and fresh ideas on the project.

Mr. Fred Johnson's know-how and efforts aided immensely in the apparatus construction. Miss Anne Hsu provided able secretarial assistance and typed the manuscript. Mr. Jeffrey Horowitz lent his drafting skills to the production of the figures. Valuable assistance was received from numerous other student and staff members of the Heat Transfer Laboratory and the Engineering Projects Laboratory.

Machine computations were performed on the I.B.M. 1130 computer of the Mechanical Engineering Department.

TABLE OF CONTENTS

LIST OF FIGURES

LIST OF TABLES

NOMENCLATURE

A	area
c	specific heat
C	capacitance
C	thermal entrance function
C_l	hydrodynamic entrance function
d	thickness
D	diameter
f_D	Darcy friction factor
f_F	Fanning friction factor
$f(\beta)$	Staub proportionality constant
g	gravitational acceleration
g_c	conversion factor (32.174 lb_m ft/lb_f sec^2)
G	mass flux
h	enthalpy
h_{fc}	forced convection heat transfer coefficient
k	thermal conductivity
K	Gambill proportionality constant
K	Henry's Law constant
L	length
N/A	number per unit area
p	pressure
q/A	heat flux
r	radius
s	entropy

T	temperature
V	velocity (liquid-only flow)
V	volume
X	mole fraction
y	coordinate perpendicular to the heated wall
Y	dimensionless turbulent profile coordinate perpendicular to the heated wall
z	coordinate parallel to the heated wall
α	void fraction
Δp	pressure drop
ΔT	temperature difference
ε	dielectric constant
μ	chemical potential
μ	dynamic viscosity
ρ	density
σ	surface tension
χ	quality (enthalpy-based)

Subscripts

b	bulk liquid condition
c	tube centerline condition
crit	critical heat flux condition
d	departure condition

f	final condition
fg	liquid-vapor phase change condition
g	vapor condition
in	inlet condition
inc	incipient condition
ℓ	liquid condition
o	initial condition
sat	one-component saturation condition
satg	two-component saturation condition
sub	subcooled condition
TP	two-phase condition
w	heated wall condition

Dimensionless Groups

Nu	Nusselt Number
Pr	Prandtl Number
Re	Reynolds Number

Chapter 1

INTRODUCTION

1.1 Background of Electronic Cooling

In the field of electronics, as in many other fields, there has come a point where further advances are limited by considerations lying outside the scope of the mother technology. This fact was recognized as early as 1942 by Mouromtseff [1], who observed that "in designing electronic tubes there are many more mechanical, metallurgical, and heat engineering problems than those of pure electronic character." Although the past thirty years have seen the appearance of "tubeless" electronics, the transistor, the laser, the maser, micro-miniaturized circuits, and countless other advances, dependence on other disciplines has, in fact, merely changed character and increased. In particular, thermal considerations are of increasing importance. Thermal design requirements, previously satisfied by borrowing from existing engineering knowledge, have changed so drastically in recent years as to prompt the development of a whole new technology to meet them.

Heat production is a normal result of the irreversible processes involved in the operation of all electronic devices. This heat causes an increase in temperature of the device until the condition is reached

that the driving force (difference between device temperature and ambient temperature) is just adequate to transfer the given energy as heat from the device to an available thermal sink. The electronic component designer's job is to tailor the overall device so that each element can operate within its proper electronic rating range.

For purposes of illustration, the history of heat transfer in electronics can be grouped very roughly into past, present, and future. The past may be represented by the vacuum tube, which was cooled quite adequately by natural convection of air for typical heat fluxes of 25 Btu/hr ft^2. Present equipment employing solid-state devices operates successfully with forced convection of air for heat fluxes of approximately 1000 Btu/hr ft^2. But future electronic designs may call for fluxes of up to 100,000 Btu/hr ft^2, making the use of liquid cooling a virtual necessity.

1.2 Restrictions Imposed on Cooling Fluids and Modes

The above requirements may not seem especially demanding to those familiar with current heat-exchange equipment since, for example, present boiling water nuclear reactor systems operate successfully at heat fluxes of the order of 400,000 Btu/hr ft^2. Unfortunately, heat flux range is only one of several considerations important to the designer of electronic components. It is usually necessary for such applications that the heat transfer fluid be dielectric, chemically stable, and inert, at least with respect to the materials with which it has direct contact. There are

considerable advantages in design and construction to be realized by operating near atmospheric pressure. Another desirable goal is to maintain as uniform a device temperature as possible. Success here facilitates the estimation of performance in components whose electronic characteristics are temperature-dependent. Other factors to be considered include fluid toxicity, availability, and cost.

Fluorocarbons comprise a class of fluids which are admirably well-suited to satisfy the above requirements related to dielectric and chemical properties, toxicity, availability, and cost. The two best-known subgroups of the class are the perfluorinated fluids represented by the "FC" series of the 3M Company and the chlorofluorocarbons represented by the Refrigerant series of the DuPont Company ("Freons") and Allied Chemical Company ("Genetrons").

For typical applications, where the ultimate heat sink used is near room temperature, a liquid-based cooling system at atmospheric pressure requires the use of a fluid whose saturation temperature at this pressure is somewhat higher than room temperature. Furthermore, if bulk temperature of the coolant has room temperature as a lower limit and if mass velocities are limited to reasonable values by natural convection-based forces or by practical pumping considerations, it becomes apparent that, for the high heat fluxes of present interest, boiling will probably occur. Since heat transfer (and device temperature) in boiling is strongly related to the local saturation temperature and since, in general, higher reliability and longer life of electronic components are enhanced by

lower device temperatures, the best fluids would probably be those with the lowest saturation temperatures which are still higher than room temperature. Two members of the fluorocarbon class, FC-78 of the former subgroup (T_{sat} = 122°F) and Refrigerant-113 of the latter subgroup (T_{sat} = 117°F) are fluids that might be considered.

It is well known that the heat transfer characteristics in certain modes of boiling are little affected by local variations in velocity, bulk temperature, and heat flux. Thus, efforts should be concentrated toward establishing the proper mode on the heated device boundary and using the characteristic to promote a uniform device temperature. It is appropriate at this point to review the generalized boiling picture and enumerate the various modes.

1.3 The General Boiling Picture

Pool boiling is the type of boiling which occurs when a heater is submerged in a pool of initially stagnant liquid. When the heated surface temperature is sufficiently above the local saturation temperature of the liquid, nucleation begins, and a complex natural circulation pattern is set up. Thus, the situation is not strictly a static one, and, although many investigators have cautioned against direct extensions, it may be qualitatively regarded as a limiting case of flow boiling. Because of simplicity in experiments, pool boiling is often the starting point for studies whose ultimate goal is the description of flow boiling phenomena.

For purposes of illustration of the general flow boiling situation, consider a vertical, uniformly-heated channel through which flows a coolant (upflow) which is subcooled relative to local saturation conditions at the inlet. "Subcooled" in the present sense implies that the temperature (and enthalpy) of the liquid at the inlet is less than that for saturation at the inlet pressure level. Assume further that the heat flux is adequate to cause boiling along part of the heated length.

A representative sketch of the situation outlined above is shown in Figure 1. Upstream of point A no bubbles are present, and the mode is pure forced convection. At point A, the so-called "incipient point," the first bubbles appear. In the region between points A and B bubbles are generally small and confined to a thin "boundary layer" (see References [2] and [3]). As the bulk subcooling decreases along the channel, the boiling surface begins to support a rapid increase in void fraction. The term "void fraction" is used here to denote the ratio of local gas-phase volume to the total local volume in a differential element at a given channel cross-section, that is,

$$\alpha = \frac{V_{\text{gas-phase}}}{V_{\text{total}}} = \frac{V_{\text{gas-phase}}}{V_{\text{gas-phase}} + V_{\text{liquid-phase}}} \qquad (1\text{-}1)$$

The location where the rapid increase starts (point B in Figure 1) is known as the "point of net vapor generation."

Bulk temperature and void fraction continue to increase until, at some point C, saturation conditions are achieved. Strictly, this means that the heat added to the fluid up to the point is sufficient to bring

the average bulk enthalpy to the saturation value corresponding to the local pressure, that is,

$$h(z) = h_{in}(T_{in}) + \frac{q/A}{G} 4 \frac{z}{D} = h_{\ell_{sat}} [p(z)] \qquad (1\text{-}2)$$

Point C is sometimes known as the boiling boundary or zero quality point since, for the enthalpy-based quality,

$$\chi(z) = \frac{h(z) - h_{\ell_{sat}} [p(z)]}{h_{fg} [p(z)]} = 0 \qquad (1\text{-}3)$$

Further, the point provides the convenient dividing line between two types of flow boiling — the upstream portion being known as the subcooled flow boiling region and the downstream portion as the bulk boiling or vaporization region.

Void fraction increases quite rapidly as the positive quality region is entered, and the liquid portion of the flow becomes limited to a thinning layer along the wall. Finally, at point D the liquid film thickness goes to zero and "dryout" occurs.

Of course, progressive flow regime changes take place in the flow from bubbly to slug to annular with all sorts of intermediate types possible also. It should be emphasized here that this is an illustrative example and that the existence and location of the various points and regimes is highly dependent on specific conditions.

In order to give a complete characterization of the specified situation, one must be able to fill in the details pertaining to variation in void fraction, bulk temperature (enthalpy), pressure level, saturation temperature (enthalpy), and wall temperature along the heated length. Schematic plots of these variables for the example situation are given in Figure 1. The total problem as seen from the designer's point of view may be best summarized as determination of heat transfer and pressure drop performance.

1.4 Areas Covered in Previous Investigations

Although some members of the fluorocarbon family have been used for years in refrigeration, aerosol, and cleaning applications, relatively few fundamental studies of their boiling behavior have been conducted. Pool boiling experiments with Freon-113 by Corty and Foust [4] provided boiling curves and indication of delayed nucleation effects. Haley and Westwater [5] used Freon-113 in their work on the performance of pool boiling fins. Armstrong [6] incorporated data on various organic fluids including Freon-12 and Freon-113 into a general correlation for the fully-developed pool boiling curve. Danilova [7] has collected the bulk of Russian pool boiling data on Freons-11, 12, 21, 22, and 113 and has attempted a general corrleation.

A survey by Gouse [8] on evaporators concentrates on positive quality flow boiling investigations and cites such work conducted with Freons-11, 12, 22, and 113. A second survey by Gouse [9] of work up to 1964 on flow boiling

stability includes some studies using Freon-113. Since the survey, further stability investigations were conducted by Gouse, Evans, Deane, and Crowley [10]; Crowley, Deane, and Gouse [11]; and Yadigaroglu and Bergles [12] — all employing Freon-113 as the working fluid.

Considerable recent interest has focused on the use of fluorocarbons as scaling and modeling fluids for high pressure water flow boiling situations. Zuber et al. [13] used Freon-22 for stability-modeling studies which also yielded detailed void fraction information and some data on heat transfer and pressure drop, primarily for positive quality flow boiling. Crowley and Bergles [14] also studied stability modeling with particular reference to Freon-113.

Critical heat flux modeling was investigated by Barnett et al. [15] and Stevens et al. [16] with Freon-12 and Freon-21 and by Dix [17] with Freon-114. Baker [18] considered flow regime modeling with Freon-11. Staub et al. [19] used Freon-22 as a model fluid for a study of detailed void fraction behavior in subcooled flow boiling and collected some related pressure drop and heat transfer measurements.

A natural and important part of the surge of boiling and two-phase flow research in recent years has been the development many theories and correlations. Although a large portion of these were oriented toward steam-water applications, some number of predictions were anchored securely enough in fundamentals to be of use for various other fluids. However, in most cases, the validity of the methods has not been convincingly demonstrated for fluorocarbons.

In general, it appears that there is a lack of fundamental heat transfer and hydrodynamic data on boiling of the fluorocarbons and that generalized theories and correlations have not been adequately verified for this class of fluids. One could justifiably ask why the boiling behavior of fluorocarbons as a class might be expected to differ to any great extent from that encountered by previous experimenters with water, liquid metals, and cryogens. Some evidence for uniqueness can be found in the individual properties of fluorocarbons. A sample comparison is given between Freon-113 and water in Table A. Notable properties of the fluorocarbon include very low thermal conductivity, very large solubility constant for dissolved gases, low surface tension, and (related) excellent wetting characteristics for all known surfaces. Although such absolute values are probably not as dependable in characterizing a particular situation as are the relevant dimensionless groups, Crowley and Bergles [14] have recently noted that "nuisance properties" such as those mentioned above may be inadequately accounted for in dimensionless similarity models and may produce misleading results in some cases.

1.5 Basis for the Present Research Program

From the previous discussion and additional practical considerations, it is clear that there remain several important questions to be answered to provide design information for cooling applications of boiling fluorocarbons. How can one properly construct the fluorocarbon boiling curve?

What effects do nuisance properties have on it? How can one predict the hydrodynamics and resulting pressure drop? How do the individual components and properties interact to produce the result?

In order to answer questions like these, the I.B.M. Corporation, in September 1966, initiated a research program at the M.I.T. Heat Transfer Laboratory to investigate thermal and hydrodynamic characteristics of dielectric liquids suitable for cooling of high-power-density electronic components. For reasons noted earlier, attention was focused on Freon-113 and FC-78.

The first two years of this program were carried out by Bergles, Bakhru, and Shires [20]. Heat transfer data were taken for both single-phase and flow boiling of Freon-113 in a short, horizontal, rectangular channel with one side heated at relatively high flux. Several different surfaces were tried with this arrangement, including stainless steel and copper with various surface treatments. FC-78 was also used for some runs in an effort to verify close correspondence of this fluid to Freon-113. Other aspects of the investigation included heat transfer with vertical flow through an annulus, pool boiling from tubular heaters, and bubble dynamics in a horizontal tube heated at low flux, all conducted with Freon-113 as the working fluid.

From experience gained in this preliminary investigation, it was judged most productive to concentrate the attention of the present study on a fundamental investigation of the subcooled flow boiling mode using a tubular heated channel in a vertical upflow orientation. Freon-113

was chosen as the prime test fluid for the necessary experiments because of lower cost, better availability, similar thermophysical properties, and better documentation of such properties when compared to FC-78. For actual implementation in electronic systems, however, FC-78 has a chemical structure which is more stable and inert than that of Freon-113, and its extra cost could possibly be warranted where ultimate reliability is required.

In Chapter 2, a brief outline of equipment and methods used in the present experimental program is provided. Chapter 3 presents general heat transfer data taken and discusses parametric effects on single-phase, partial boiling, and fully-developed boiling heat transfer modes, including comments on boiling incipience and critical heat flux. Chapter 4 concentrates on an examination of the hysteresis phenomenon and dissolved gas effects, the most unique aspects of heat transfer behavior encountered in the study.

Chapter 5 presents general pressure drop data taken and discusses parametric effects on single-phase and two-phase total pressure drop. Chapter 6 examines void fraction behavior and uses data concerning it to estimate components of total pressure drop.

Chapter 2

OUTLINE OF EXPERIMENTAL EQUIPMENT AND METHODS

In order to fulfill the objectives of the experimental program, two separate loops were used. The high flux loop was the primary facility, providing for high heat flux, vertical flow experiments with control of the dissolved gas content of the circulating coolant. The low flux loop was the support facility, allowing low heat flux, horizontal flow experiments with visual observation of the heating surface. These loops, associated test sections and instrumentation, detailed operating procedures and data reduction programs are described in the remainder of this chapter and in Appendices A, B, C, D, and E.

2.1 Low Flux Loop and Test Section

Located in the main bay of the Engineering Projects Laboratory, the low flux loop was originally constructed by Coumou [21] and was subsequently modified several times. A schematic and a photograph of the facility in the configuration used for the present runs are shown in Figures 2 and 3.

On the primary circuit, coolant was pumped from the reservoir through a flow meter to a heat exchanger which acted as a preheater to give the test fluid any required inlet temperature. After passing

through the test section, the coolant was directed to another heat exchanger which served as a subcooler to prepare the fluid for return to the pump and recirculation. In addition to the circuit just outlined, a bypass leg between the pump outlet and the reservoir allowed for pressure level adjustments within a limited range.

The heated portion of the low flux test section consisted of a horizontal assembly of Corning Pyrex tubes which had a thin, electrically-conducting coating. This novel construction had the advantage of providing for electrical heating while allowing direct visual observation of the internal boiling surface. Immediately downstream from the heated section was an adiabatic length which accommodated an electronic void sensor and two glass adapter sections as shown in Figure 4.

Provision was made for flow rate, pressure level, heated section power, bulk temperature, wall temperature, and void fraction measurements. Detailed apparatus and instrumentation descriptions and specifications are contained in Appendices A and B. Since experiments on the low flux facility were oriented primarily toward examining the performance of the capacitance void measuring system, such results are contained in Appendix B.

2.2 High Flux Loop

The basic high flux loop was constructed in the Heat Transfer Laboratory [20]. A schematic and a photograph of the facility in the configuration used for the present experiments are shown in Figures 5 and 6.

On the primary circuit, coolant flowed from the reservoir through a filter and a filter-drier and then was pumped through one of two flow meters to the test section. From the test section exit, the fluid traveled to a heat exchanger which served as a subcooler to prepare the fluid for refiltration and recirculation by the pump. In addition to the circuit just outlined, there were several other piping legs which served auxiliary functions. Four legs allowed pressure level regulation by acting as adjustable bypasses and flow reversal elements. A gas vent was located at a high point following the flow meters, and two drains, one at the pump inlet and one on the low side of the heat exchanger, permitted easy flushing of the system.

One of the unique advantages of the loop was the ability to control and monitor the dissolved gas content of the fluid. The reservoir was provided with immersion heaters to promote pool boiling and saturation conditions whenever relative degassing was required. A bleed flow line from the inlet side of the heat exchanger to the reservoir assured continuous and reliable degassing of the main loop flow. Monitoring was accomplished by analysis of samples taken from a port in the test section inlet. Electrical power for heating the test sections was provided by DC generators located adjacent to the loop. Detailed apparatus and instrumentation descriptions and specifications are contained in Appendix A.

2.3 High Flux Test Section

The high flux test section arrangement consisted of three main elements — inlet, heated length, and outlet. The inlet side provided for main flow throttling, electrical and mechanical isolation from the rest of the loop, monitoring of inlet bulk temperature, and sampling for the determination of dissolved gas content.

A detailed drawing of the heated length is shown in Figure 7. It provided for uniform, direct, measured, DC electric heating of the stainless steel tubing; pressure level and total pressure drop measurement over the heated length; tube wall temperature profile measurement; and separate guard heating to minimize heat losses and temperature errors. Temperature monitors were located near the end of the heated length to allow the experimenter to detect a critical heat flux situation early enough to act to avoid the onset of destructive burnout.

The outlet side of the test section provided for electrical and mechanical isolation from the rest of the loop, monitoring of exit bulk temperature, visual observation of flow phenomena, and void fraction measurement. Two separate systems, the trap-visual system and the Ikor V/L System, Model 545-2, were used for void fraction data. The former method has been commonly used in adiabatic situations (usually air-water) by other experimenters, but it appears that only one previous study, that by Colombo, Hassid, and Premoli [22], has reported the use of an analogous method under diabatic conditions. Capacitance sensing of void fraction has attracted considerable discussion and some interest, but experimental

experience with the particular device and two-phase situation of interest here was not previously available. A comprehensive discussion of the lengthy series of predictions, comparisons, and calibrations required to assure the validity of the present void fraction data is given in Appendix B.

There has been a similar lack of published boiling investigations in which the dissolved gas content was controlled and measured by demonstrably reliable means. Because of the relatively large tendency of fluorocarbons to dissolve gases, such control and measurement were prime goals of the present study. A summary of the extensive operation, prediction, and comparison procedures undertaken to assure the accuracy of the present measurements of dissolved gas content is given in Appendix C.

Further information on the construction and instrumentation of the high flux test section is contained in Appendix A. Appendix D contains a detailed outline of the experimental procedure followed in runs with the high flux test section. A summary of the data reduction programs used in preparing the high flux raw data for analysis and interpretation comprises Appendix E.

2.4 Problems Encountered in a Fluorocarbon System

It is appropriate at this point to try to enumerate some of the problems encountered in the design and construction of the loops — or of cooling systems for electronic components — which may not be obvious

from the outline given in the preceding sections. Such difficulties may not necessarily accompany the use of all fluorocarbons, but these may be looked on as being probably representative and definitely worthy of consideration in any related study.

The saturation state properties of Freon-113, namely high vapor pressure for low temperature (or, alternatively, low boiling point for low pressure), produce at least two practical problems. One involves the loss of fluid by evaporation from a reservoir exposed directly to room temperature, room pressure (or comparable) conditions. The problem is especially acute when the reservoir is maintained near saturation temperature for degassing purposes. Such loss was minimized by restricted venting of the reservoir through a water-cooled condenser in the present case. The second problem involves cavitation within the pump and can be avoided by monitoring and assuring an adequate pressure at the pump inlet.

The low surface tension and excellent wetting characteristics (for all tested surfaces) of Freon-113 are noticed first by the experimenter when he finds that "no-leak" valves and joints do leak. A further difficulty can be experienced in locating leaks. Because of the strong tendency for the fluid to evaporate (see above), there may be no telltale wetness. The diligent search may require the use of commercial additives and/or electronic leak detectors for refrigerants. Leakage was minimized in the present apparatus by use of (a) sweat connections when possible or threaded connections sealed with Teflon tape dope when necessary;

(b) ball valves with double Teflon seals when possible or precision-seating diaphragm valves when required; (c) Teflon or Buna N gaskets for all unions and assembly connections; and (d) a mechanically-sealed, drip-proof motor and pump system.

Although it is relatively stable and unreactive as chemicals go, Freon-113 is not "compatible" with many common materials. This incompatibility can take the form of chemical reaction or dissolution or both. The abilities of Freon-113 as an organic solvent are well known to the dry cleaning industry and serve to classify it as an excellent degreaser. Adverse consequences have been observed with oils and greases (both organic and silicone), plastics (especially Plexiglas), rubbers (notably natural and Buna S), and various other substances. In particular, the previous study [20] experienced crazing of Plexiglas sheets by Freon-113 and progressive discoloration of loop fluid due to its contact and reaction with rubber hose.

Efforts to eliminate incompatibilities in the present investigation included judicious use of Teflon, Nylon, Buna N, glass, copper, and glycerine and phosphate-based greases as substitutes for the more common troublesome substances. A further effort, aimed toward keeping the working fluid free from contaminants, involved the two-component filtration-dehydration setup described in Appendix A.

Finally, one must consider the safety-related item of toxicity. Freon-113 vapor is regarded as being only slightly toxic (between Groups IV and V of the MSA ratings) in normal concentrations, but its high

vapor pressure suggests that caution be associated with its use. However, under conditions of extreme temperature excursions, the fluid may decompose into poisonous products such as phosgene gas [20]. More moderate temperature excursions may cause fouling of the heated surface by a carbon-like deposition layer. Thus, the experimental researcher must take adequate precautions in the laboratory, and the designer is charged with the responsibility of providing acceptable safety tolerances for commercial equipment.

In summary, this list is not meant to be an exhaustive survey of relevant problems, but it is included to add a "feel" for the types of problems which may nag in the beginning but glare at the end.

Chapter 3

HEAT TRANSFER

In order to estimate heat transfer results such as the wall temperature profile shown in Figure 1, one must have accurate methods for determining where each mode will be dominant in a given situation. For example, it is important to predict the incipient point, marking the division between the forced convection and flow boiling modes. Similarly, an attempt should be made to identify significant transitions within modes, such as that from "partial boiling" to "fully-developed nucleate boiling." Extreme operating limits of interest to the designer may actually be legislated by such mode boundaries, the prime example being the upper limit known as critical heat flux, where there is a departure from nucleate boiling to film boiling. After determining such mode limits, one faces the task of characterizing each mode by its peculiar heat transfer abilities and dependences on relevant variables.

3.1 The Form of the Flow Boiling Curve

The details of the heat transfer aspects of the present situation are best observed in terms of standard flow boiling curve plots such as that shown in Figure 8. For present purposes, one may regard each curve

as a set of data derived from the measurement of wall temperature at a given point z in the heated length for each value of imposed heat flux, while maintaining local pressure, inlet subcooling, and mass velocity constant. Use of heat flux as the ordinate and wall minus saturation temperature as the abscissa emphasizes the previously-mentioned important dependence of boiling phenomena on saturation conditions. Log-log plots facilitate the observance of common power-law relations often encountered for the "fully-developed" situation.

The curves plotted in Figure 8 have a form which is common to many engineering fluid-surface combinations. The example graph, taken from Reference [23] for degassed water-stainless steel, is typical of many moderately good wetting situations. As the heat flux is increased, there is a relatively smooth transition from the forced convection to the partial boiling portion at the incipient point. Then the slope of the curve gradually increases until the partial boiling mode merges with the fully-developed mode, where the slope stabilizes. If, before the critical heat flux condition is reached, the heat flux is decreased gradually, the data retrace very nearly the same curve.

The contrast to be found in the curves typical of the data which follow on the Freon-113-stainless steel situation is illustrated in Figure 9. It is clear that, on the increasing heat flux portion of the curve, the forced convection mode is extended. Also, there is a large, discontinuous jump in wall temperature at the end of the forced convection mode. After the jump, the trend toward a fully-developed type of

curve is not smooth and may be divided into two regions, called "readjustment" and "transition" here for reasons to be presented later in the discussion. The data for decreasing heat flux follow those generated by increasing heat flux until the region near the incipient jump. Here, the decreasing curve continues smoothly down to merge with the forced convection mode curve at some lower heat flux. The performance just outlined has been traditionally called "hysteresis" in boiling literature. A detailed examination of this phenomenon as related to the situation at hand is postponed to Chapter 4.

As is noted in Appendix A, the high flux test sections were instrumented to obtain wall temperature measurement at four different heated length positions (eight wall thermocouples). When such measurements are taken simultaneously, they can be used to directly construct wall temperature profiles like that shown in Figure 1. By plotting all the various position boiling curves on one graph, as in Figure 10, one can clearly identify the relative performances of the various portions.

At low fluxes, when the entire heated length is in the forced convection mode, the wall temperature can be quite non-uniform (primarily due to entrance effects), as shown by the data. Then as the heat flux increases, the exit end of the heated length nucleates, and a virtual discontinuity in wall temperature occurs. Subcooled boiling is limited to the exit while forced convection persists over the rest of the test section. As the heat flux increases further, the subcooled boiling region expands, the "discontinuity" moves toward the inlet, and each of the monitoring thermocouples is "tripped."

After a certain level of heat flux is attained, essentially the entire heated length is in the subcooled flow boiling mode. The advantages of this mode are obvious when viewed in terms of Figure 10. The axial variation of wall temperature is seen to be less than 2°F for the range of 10,000 - 40,000 Btu/hr ft^2. Furthermore, the rise of wall temperature with heat flux is much slower for the boiling case than for forced convection and, in this particular case, follows a regular power-law trend soon after incipience.

Most of the rest of the boiling curves presented here will not be of the composite-profile type. They will instead present the results from a single point on the heated length (usually that located closest to the exit — still far enough upstream to avoid end effect errors) under various imposed conditions. Such an approach is convenient for present purposes, but reference to composite-profile data will be made where necessary to clarify or explain certain concepts.

3.2 Single-Phase Results

All single-phase data were taken for the case of turbulent, forced-convection flow. Representative results for two locations are given in Figure 11.

For comparison, the standard McAdams [24] correlation with correction for entrance effects from Deissler [25] is also presented in the figure, according to the relation

$$Nu(z) = 0.023\ C\ Re^{0.80}\ Pr^{0.40} \qquad (3\text{-}1)$$

where $C = C(Re, Pr, z/D)$

It can be seen that the data and the prediction very nearly coincide over the Reynolds Number range 4,400 - 36,000.

Implicit in the above relationships is the fact that single-phase heat transfer improves with increasing velocity and/or increasing subcooling. These traditional trends will reappear in the single-phase portions of the boiling curves which follow. It was found in all the boiling runs that the data followed the McAdams correlation right up to the point where incipience occurred.

After the correspondence of the single-phase Freon-113 data with the McAdams correlation was established, the relationship was used for an instrumentation double-check preliminary to the boiling runs, as noted in Appendix D.

3.3 Parametric Effects

A convenient and useful way to investigate the heat transfer problem is through an examination of parametric effects. For the given geometry, mass velocity, pressure, subcooling, dissolved gas content, and heat flux can be varied independently. Unfortunately, results from systematic variations of these quantities can lead to confusing conclusions. This problem is primarily due to the common use of two different approaches to the study of parametric effects on boiling situations.

One is called the "local" approach and may be illustrated by a series of experiments which maintains the mass velocity, dissolved gas content,

and local pressure and subcooling constant at some point z, while varying the heat flux. Thus, while the heat flux increases, the inlet bulk temperature must decrease (inlet subcooling increases) so that local subcooling at z will remain constant. Inlet pressure may also be required to change to maintain the pressure level at z constant, depending on alterations in the pressure drop caused by the change in heat flux. This approach is dedicated to the proposition that certain of the boiling phenomena at a given point are entirely determined by conditions at the point.

The second is called the "system" approach and may be illustrated by a series of experiments which maintains the mass velocity, dissolved gas content, and inlet pressure and subcooling constant, while varying the heat flux. Thus, at any given point z, the local subcooling will decrease as the heat flux is increased. This approach is motivated by the practical desire to analyze a system by its response to a known set of externally-imposed inputs.

As is obvious from the above examples, neither approach allows for total comparability at every point. The situation is due to a very fundamental consideration — namely, that all the relevant variables are not independent. The energy equation, given in one form by Equation (1-2), is the additional constraint and serves to reduce the number of independent variables by one. The confusion occurs when constant local variable results are compared with those involving constant system variables.

Neither of the above approaches was used exclusively in the present investigation, but, in examining the results, one should be careful to note the exact specifications and positions of measured variables.

Representative data from a series of high flux runs whose purpose was to investigate mass velocity effects are given in Figure 12. As noted earlier, the single-phase data follow the McAdams correlation until nucleation is initiated. Better cooling is achieved for higher velocity in this mode, as expected. Accordingly, incipience requires higher heat fluxes for the higher velocities. The readjustment and transition regions have relatively consistent shapes for the examples given.

Next, it should be noted that all the curves tend toward the same asymptote as they approach the fully-developed mode. It is clear, at least for the variable range of present interest, that the fully-developed mode is insensitive to variations in mass velocity. Operation in this mode has special advantages for electronic cooling applications because it ensures that, under constant heating load, each portion of the surface will be maintained at a constant temperature, regardless of any reasonable local variations in mass velocity.

From data on 23 organic liquids (including Freon-113) and 12 surface materials (including stainless steel), Armstrong [6] has constructed a correlation for fully-developed pool boiling at 14.70 psia. His relation may be expressed as

$$q/A = 0.244\ (T_w - T_{sat})^{3.41} \qquad (3\text{-}2)$$

If, as was found in [20], pressure dependence of such a curve may be adequately modeled by Rohsenow's correlation [26], we have for a given heat flux

$$\frac{(T_w-T_{sat})_1}{(T_w-T_{sat})_2} = \left[\frac{h_{fg_1}}{h_{fg_2}}\right]^{0.67} \left[\frac{c_{\ell_1}}{c_{\ell_2}}\right]^{0.70} \left[\frac{\mu_{\ell_1}}{\mu_{\ell_2}}\right]^{1.37} \left[\frac{\sigma_1}{\sigma_2}\right]^{0.17} \left[\frac{(\rho_\ell-\rho_g)_2}{(\rho_\ell-\rho_g)_1}\right]^{0.17} \left[\frac{k_{\ell_2}}{k_{\ell_1}}\right]^{1.7} \tag{3-3}$$

For the particular case of converting the Armstrong equation at 14.70 psia to one applicable at 22.3 psia, the resulting curve is shown in Figure 12. It can be seen that this plot provides a remarkably good fit to the fully-developed portion of the present flow boiling curves.

It is appropriate here to add a note of caution concerning generalization of the results above. First, the scatter of data of other investigators around Armstrong's curve is relatively large. Reference [20] indicates that the fully-developed curve may be quite sensitive to the particular fluid-surface combination. Second, the complete Rohsenow correlation accounts for the pressure shift given assuming a temperature-difference exponent of 3.00. Thus, the agreement noted earlier may, in fact, be fortuitous. It is suggested that, for maximum accuracy, the fully-developed boiling curve be determined by direct experiment.

One should note that, for the data in Figure 12, the inlet subcooling — a system variable in this example — was maintained constant, but the exit subcooling — the local variable — varied with velocity for a given heat flux.

Figure 13 shows representative data from experiments meant to examine the effects of inlet subcooling on heat transfer behavior. As before, subcooling effects on the single-phase forced convection data are adequately modeled by the McAdams correlation. Thus, higher inlet subcooling induced better heat transfer and resulting lower wall temperature, as expected. Incipience occurs at nearly the same heat flux, but it appears that the readjustment mode is extended in range by increasing subcooling.

Overall, the curves have very similar forms, and the consistent trend of the transition portion of the curves toward a common fully-developed mode complements the observation in the previous paragraphs. Once again, the pressure-modified Armstrong curve seems to fit the fully-developed mode data very well.

Although no analogous series of runs was conducted with local subcooling as the manipulated variable, such information can be obtained from composite plots like Figure 10. For a given heat flux, each z location corresponds to a different local subcooling. The most important fact to be drawn from this approach is that, as with the variation in inlet subcooling, variation in local subcooling has very little effect on the fully-developed flow boiling curve. For example, at the highest

flux shown in Figure 10, the wall-saturation temperature difference is essentially the same whether the local subcooling is 7°F or 44°F.

Results from a series of runs with variation of the dissolved gas content of the Freon-113 are given in Figure 14. As expected, such variation has no measurable effect on data in the single-phase forced convection mode. Incipience, on the other hand, occurs at somewhat lower heat flux and considerably lower wall temperature as the gas content increases. The incipience jump is to a much lower wall temperature with significant gas present.

There is little difference in the level of the readjustment zones, but the transition behavior extends to much higher heat fluxes for the "gassy" run — delaying the onset of the fully-developed condition. As with the other parametric runs, once the fully-developed mode is achieved there is a regular trend to the boiling curves, and, in fact, they coincide for widely-varying values of dissolved gas content. A good approximation to the data in this mode is again provided by the pressure-modified Armstrong curve.

3.4 Critical Heat Flux

For the present case, as in many other boiling situations, determination of the critical heat flux is both one of the most important and one of the most complex problems facing the designer. Other names of this upper limit for operation in the nucleate boiling mode include boiling crisis, burnout, and departure from nucleate boiling (DNB).

The confusion between system and local approaches is most common in formulation and use of critical heat flux correlations. An informative survey of the flow boiling crisis problem was compiled by Tong [27] and serves to prepare the reader for such difficulties as "parametric distortion."

Due to inherent limitations, the present investigation was not primarily oriented toward an exhaustive study of critical heat flux. In fact, special care was taken with each test section to avoid critical heat flux as long as possible. Still, a reasonable number of such data points resulted from the experimental investigation. In general, the critical heat flux condition was indicated by a large temperature excursion as monitored by the exit thermocouple and recorder system. In most cases, it was possible to avoid destructive burnout of the heated length. Although these runs do not cover any large range of the relevant variables, they do provide for an assessment of the validity of one particular correlation and give the designer a feeling for the scatter he may expect from typical data.

Following the superposition idea suggested by Rohsenow [28] for flow boiling, Gambill [29] formulated a related approach to flow boiling crisis and attempted a correlation of data as follows:

$$q/A_{crit} = (q/A_{crit})_{\text{pool boiling}} + (q/A_{crit})_{\text{forced convection}} \qquad (3\text{-}4)$$

where

$$(q/A_{crit})_{\text{pool boiling}} = Kh_{fg}\,\rho_g \left[\frac{\sigma g_c g(\rho_\ell-\rho_g)}{\rho_g^2}\right]^{0.25} \left[1 + \left(\frac{\rho_\ell}{\rho_g}\right)^{0.923} \frac{c_\ell\,\Delta T_{sub}}{25\,h_{fg}}\right] \qquad (3\text{-}5)$$

in which $K = 0.12 - 0.17$

c_ℓ is evaluated at

$$T = T_{sat} - \frac{\Delta T_{sub}}{2}$$

and where

$$(q/A_{crit})_{\text{forced convection}} = h_{fc}\,[(T_w)_{crit} - T_b] \qquad (3\text{-}6)$$

in which

$$(T_w)_{crit} = f(T_{sat},\ V,\ \frac{T_{sat}}{T_{crit}})$$

is taken from Bernath's data [30].

The correlation is one of the few which attempts to account for the effects of general properties for various fluids. It was developed for seven fluids, none of which was a fluorocarbon. The most questionable part of the correlation is the determination of the appropriate critical wall temperature. Bernath's plot [30] was originally constructed for water, and the reasoning behind extending its use to other fluids seems

quite weak. Fortunately, for the data presented here, the contribution of the forced convection term to the total is quite small.

Other criticisms of the form of the Gambill equations might include the omission of possible surface effects, the large range specified for the lead constant, and the deceptively implicit nature of the pool boiling term. Actually, these latter two points are related. The implicit form hides the fact that, for most cases, the range is not directly dependent on the lead constant. In particular, the ΔT_{sub} term is directly related to the heat flux (for a given inlet temperature) through the energy equation, and solution of the Gambill correlation equations requires use of an iterative technique.

In Figure 15 an "operating curve" approach is used to present the results predicted by the Gambill method for a particular pressure, inlet subcooling, and heated length for flow boiling with Freon-113. The trend for these fixed variables is that critical heat flux increases with flow velocity.

The set of data taken for these conditions is plotted on the appropriate operating lines of Figure 15. The scatter encountered is typical of other critical heat flux investigations for flow boiling. It appears from the data that the Gambill correlation puts a sort of upper bound on critical heat flux for the given situation. In results given in Table B and calculated for other conditions not conveniently compared on a single graph, this tendency was consistently duplicated.

On the whole, the correlation seems to do a reasonable job of

predicting effects of mass velocity and inlet subcooling. No consistent effect on critical heat flux was found for variations in dissolved gas content. However, the designer must be careful to note both the scatter and the upper bound quality of the correlation since, in all probability, it would be necessary for the design limit to lie on the conservative side of the upper limit. If, by chance, critical heat flux conditions are attained in operation, serious consequences — including surface carbonization, toxic gas production, and physical destruction of the surface ("burnout") — may result when using the fluorocarbons. Still, as an example of practical use of the analysis, the present experimenter was able, after some minimal experience and use of Gambill's correlation, to obtain required heat transfer data up to quite near critical heat flux and to repeat the data — avoiding burnout until all scheduled runs with the given test section were completed.

Chapter 4

HYSTERESIS AND DISSOLVED GAS EFFECTS ON HEAT TRANSFER

In the previous chapter, methods were presented for predicting heat transfer performance with respect to the single-phase forced-convection mode, the fully-developed flow-boiling mode, and critical heat flux for situations in the range of current interest. It still remains to accurately characterize the partial flow boiling mode — that is, the mode from incipience to attainment of the fully-developed mode. Fundamental to any description of this intermediate regime are the prediction of the incipient point, the explanation of delayed nucleation and resulting hysteresis, and the modeling of apparently large effects of dissolved gas on partial boiling results.

4.1 Dissolved Gas — Analysis of Equilibrium and Determination of the Adjusted Saturation Temperature

As background for the discussion which follows, this section is devoted to a unified treatment of equilibrium concepts of the dissolved gas situation, with illustrations from the gas-liquid combination of present interest — "air" (see Appendix C) in Freon-113.

An important step toward assimilating information on dissolution

phenomena is to understand the many different, but related, units used to express solute-solvent quantities. A sampling of the various units encountered in this investigation is listed in Table C. Depending on the particular choice from the list, the number used may vary by at least eight orders of magnitude. The first three entries are weight or mass based and are very simply related. The fourth is molecule-based and is directly related to the previous three by means of the solute and solvent molecular weights.

All of the above units seem to have a rather fundamental basis, but they may fail to give the experimenter or designer any real feel for the quantities involved. One may visualize the variable as a given "bunch" of gas which is (or whose composite molecules are) somehow "put" into a "bunch" of liquid. Here a volume-based quantity may provide a preferable choice, and the last two entries in the table are examples. Some extra caution is required in relating these units to the more basic ones mentioned before. For example, though the amount of liquid Freon-113 (that is, the number of molecules) in a given volume may vary very little with temperature and pressure, the amount of air in a given volume is indeterminate without such specifications. Still, since no standard quantity seems to have been established for general use in the field, one must be able to perform conversions from diverse units. It may be noted that, as a convention in the present work, the mole fraction, the fourth entry in Table C, has been adopted as the standard unit for expressing dissolved gas content.

For many gas-liquid combinations, including air in most fluorocarbons, the equilibrium dissolution situation can be accurately modeled by Henry's Law. In simple terms, for the present case, it postulates that the amount of gas (expressed as mole fraction) dissolved in a liquid is proportional to the partial pressure of that gas above the liquid, where the proportionality constant is a function of temperature only — that is,

$$X_{air} = K_{air \text{ in Freon-113}}(T) \; p_{air} \qquad (4\text{-}1)$$

Unfortunately, little previous data was available on the Henry's Law constant for air in Freon-113. Of necessity, the present experiments included accurate determination of this constant (also known as the "solubility constant") and its temperature variation over the range of interest. The results are summarized in Appendix C and Figure 47.

Consider now a closed, isolated, one-component, two-phase (gas-liquid), system of Freon-113 in thermodynamic equilibrium. Let us assume that the one independent state variable allowed to this system is pressure, which is arbitrarily set at

$$p = 14.70 \text{ psia}$$

The other thermodynamic properties of the system are dependent and are determined as "saturation" state values at the given pressure. Thus, for this particular case, the "saturation" temperature, necessarily uniform within the equilibrium system, is found to be

$$T = T_{sat}(p) = 118°F$$

This temperature is the relevant one used in boiling curve plots for the one-component case. System A of Figure 16 summarizes the conditions outlined here.

Next, consider a closed, isolated, two-component, two-phase, (gas-liquid) system of air and Freon-113 in thermodynamic equilibrium. By adding another component, we have allowed another degree of freedom to the system. Therefore, let us assume that the two independent state variables allowed to the system are the total pressure and the dissolved gas content (as measured by mole fraction) in the liquid phase, which are arbitrarily set at

$$p_{total} = 14.70 \text{ psia}$$

$$X_{air} = 10.80 \times 10^{-4} \text{ moles/mole}$$

The other thermodynamic properties of the system are once again dependent and are determined by the appropriate equilibrium relations. Thus, for gas-liquid combinations to which Henry's Law applies, such as air in Freon-113, one finds that

$$p_{air} = \frac{X_{air}}{K_{air \text{ in Freon-113}}(T)} \tag{4-2}$$

$$p_{Freon\text{-}113 \text{ vapor}} = p_{total} - p_{air} \tag{4-3}$$

$$T = T_{satg}(p_{total}, X_{air}) \tag{4-4}$$

When the Henry's Law constant is a function of temperature, the formulation comprises a system of implicit equations, and a trial-and-error soltuion is probably required. For our example situation, the solution takes the form (using Figure 47 and the one-component saturation line shown in Figure 17)

$$p_{air} = \frac{10.80 \times 10^{-4}}{1.34 \times 10^{-4}} = 7.82 \text{ psia}$$

$$p_{\text{Freon-113 vapor}} = 14.70 - 7.82 = 6.88 \text{ psia}$$

$$T_{satg} = 80°F$$

It may be noted that the amount of dissolved gas specified above is representative of that which is present in a well-mixed quantity of Freon-113 liquid exposed to room conditions. The particular two-component situation is summarized in System B of Figure 16.

It is clear that the two "equilibrium temperatures" are quite different. Then, if the connotation of the term "saturation" may be taken to be that of equilibrium in each of these situations, one can see that the saturation temperature varies with dissolved gas content for a given total pressure level. In order to avoid confusion with the strict single-component sense of saturation temperature, it is probably helpful to denote the two-component analogs as "adjusted" or "gassy" saturation temperatures.

Now, by way of extension, for the same mole fraction, one can impose a different total pressure and solve for the new adjusted saturation temperature, constructing step-by-step a pressure-temperature characteristic of the given system — Freon-113 with 10.80×10^{-4} moles/mole dissolved air. Each mole fraction constitutes a different system and has its own curve. The ensemble of curves for all possible mole fractions comprises a pressure-temperature map such as that shown in Figure 17.

One can see from Figure 17 that, for any given total pressure level, the highest saturation temperature occurs for the one-component or "degassed" case. Thus, the introduction of gas into a constant total pressure system will inevitably result in a decrease in the appropriate saturation temperature.

For the case where the solubility constant does not vary with temperature, the family of curves has a consistent shape, the curve for each dissolved gas mole fraction being displaced upward by a constant amount from the single-component curve along its entire length. The temperature variation of $K_{air \text{ in Freon-113}}$, given in Figure 47, is relatively small so that the similarity condition very nearly applies for the situation of present interest.

In summary, this section has shown that the equilibrium saturation temperature of a fluid system varies with dissolved gas content, that the variation may be relatively large for common situations, and that the variation may be determined for cases where Henry's Law applies. A

pressure-temperature map so determined for air in Freon-113, Figure 17, will be used in subsequent sections. With this dependence uncovered, it becomes obvious that the crucial consideration is to determine which parts of the experimental nonequilibrium situation approach equilibrium closely enough to allow the application of the "adjusted saturation temperature" as an appropriate analytical variable.

4.2 A Prediction for Incipience With Dissolved Gas

For a first attempt at trying to understand the apparently curious characteristics of the onset of boiling as shown in Figures 9, 10, 12, 13, and 14, let us develop an analytical model for the idealized situation at the incipient point. The analysis draws on ideas presented previously by Hsu and Graham [31], Bergles and Rohsenow [32], and Behar et al. [33].

Consider the incipient bubble, emanating in hemispherical form from an active cavity of radius r on a heated surface bordering a turbulent, forced flow of liquid. For simplicity, initial analysis will be restricted to a one-component, two-phase system — say Freon-113 liquid and Freon-113 vapor. Assume now that quasi-equilibrium applies in the immediate vicinity of the bubble. Then, in terms of the variables given in Figure 18, the three conditions necessary to satisfy mechanical, thermal, and chemical potential equilibrium are

$$p_g - p_\ell = \frac{2\sigma}{r} \tag{4-5}$$

$$T_g = T_\ell \tag{4-6}$$

$$\mu_g = \mu_\ell \tag{4-7}$$

This rigorous form of the analysis requires use of the relevant property relations as indicated in Figure 19. The example plot given is exaggerated, but it clearly shows that the equilibrium temperature is higher than both the flat-interface saturation temperature corresponding to the liquid pressure and that corresponding to the vapor pressure — that is,

$$T_g = T_\ell = T > T_{sat}(p_g) > T_{sat}(p_\ell) \tag{4-8}$$

Thus, both phases may be said to be "superheated" in relation to their respective flat-interface saturation temperatures. In actuality, for most fluids, the line AB (see Figure 19) lies so close to the flat-interface saturation line that the following approximate relations hold to good accuracy

$$T \simeq T_{sat}(p_g) \tag{4-9}$$

$$T - T_{sat}(p_\ell) \simeq (p_g - p_\ell) \left.\frac{dT}{dp}\right|_{\substack{\text{at } p_\ell \text{ along the flat-} \\ \text{interface saturation line}}} \tag{4-10}$$

or, combining with Equation (4-5)

$$T - T_{sat}(p_\ell) = \frac{2\sigma}{r} \left.\frac{dT}{dp}\right|_{\substack{\text{at } p_\ell \text{ along the flat-interface} \\ \text{saturation line}}} \tag{4-11}$$

Differentiation with respect to r gives

$$\frac{dT}{dr} = -\frac{2\sigma}{r^2} \left.\frac{dT}{dp}\right|_{\substack{\text{at } p_\ell \text{ along the flat-interface} \\ \text{saturation line}}} \tag{4-12}$$

Now consider the two-component, two-phase analog of the above analysis — namely, an air-Freon-113 system again in quasi-equilibrium. Equations of the type (4-5), (4-6), and (4-7) still must be satisfied, but a fourth relation is required to insure chemical potential equilibrium of all species. It may be expressed as

$$\mu_{air_g} = \mu_{air_\ell} \tag{4-13}$$

or, where Henry's Law applies

$$X_{air} = K_{\text{air in Freon-113}}(T) \; p_{air} \tag{4-14}$$

The physical situation is depicted, and appropriate variables are assigned in Figure 20.

It is easily shown that the new constraint alters the previous analysis by specifying a different flat-interface saturation line — that is, one for the two-component (air-Freon-113) system. Similarly, the

mechanical equilibrium equation is modified to account for the respective partial pressures within the bubble

$$p_{bubble} - p_{\ell} = \frac{2\sigma}{r} \tag{4-15}$$

where

$$p_{bubble} = p_g + p_{air} \tag{4-16}$$

Thus, the "gassy" equivalents of Equations (4-11) and (4-12) become

$$T - T_{satg}(p_{\ell}, X_{air}) = \frac{2\sigma}{r} \left.\frac{dT}{dp}\right|_{\text{at } p_{\ell} \text{ along the flat-interface gassy saturation line}} \tag{4-17}$$

and

$$\frac{dT}{dr} = -\frac{2\sigma}{r^2} \left.\frac{dT}{dp}\right|_{\text{at } p_{\ell} \text{ along the flat-interface gassy saturation line}} \tag{4-18}$$

Having established the relevant relations for the postulated quasi-equilibrium incipient bubble, let us turn now to modeling of the local heat transfer and temperature profile conditions. Since the bubble and cavity sizes are generally smaller than the thickness of the laminar sublayer in the typical turbulent flow situation, the temperature distribution in the liquid near the heated wall can be approximated by a linear relation as follows:

$$T_w - T_{\ell} = q/A \frac{y}{k_{\ell}} \tag{4-19}$$

The slope of the profile is constant (neglecting small variations in the liquid thermal conductivity) and is given by

$$\frac{dT_\ell}{dy} = - q/A \ \frac{1}{k_\ell} \tag{4-20}$$

At this point, the difficulties associated with the quasi-equilibrium approximation become apparent in the problem of relating the local liquid temperature profile to the temperature resulting from the equilibrium incipient bubble analysis. Following the reasoning of Bergles and Rohsenow [32], we take as the appropriate relations for incipience

$$T_\ell = T \tag{4-21}$$

and

$$\frac{dT_\ell}{dy} = \frac{dT}{dr} \tag{4-22}$$

at

$$y = r \tag{4-23}$$

Evidently the first equation is an upper bound since all of the liquid surrounding the bubble would then be able to transfer heat to it. The second equation follows from the fact that, assuming cavities of all sizes are available for nucleation, increasing heat flux will bring the temperature profile curve, Equation (4-19), into contact (solution) with the mechanical equilibrium profile, Equation (4-11) or Equation (4-17), first when the tangency condition is just satisfied (see Figures 18 and 20).

Finally, there exists the heat transfer relationship, as obtained for forced convection with the particular flow variables, which may be taken from experiments or correlation and presented in boiling curve

form as

$$q/A = f(T_w - T_{sat}) \tag{4-24}$$

or

$$q/A = f(T_w - T_{satg}) \tag{4-25}$$

Equations (4-11), (4-12), (4-19), (4-20), (4-21), (4-22), (4-23), and (4-24) represent a non-linear system of eight independent equations in the eight variables T_w, T, T_ℓ, r, y, $\frac{dT}{dr}$, $\frac{dT_\ell}{dy}$, and q/A. The simplest solution method is probably the reduction of the first seven equations to the form

$$q/A = \frac{k_\ell}{8} [T_w - T_{sat}(p_\ell)]^2 \left.\frac{dp}{dT}\right|_{\text{at } p_\ell \text{ along the flat-interface saturation line}} \tag{4-26}$$

or, for the gassy case

$$q/A = \frac{k_\ell}{8} [T_w - T_{satg}(p_\ell, X_{air})]^2 \left.\frac{dp}{dT}\right|_{\text{at } p_\ell \text{ along the flat-interface gassy saturation line}} \tag{4-27}$$

These relationships can be easily plotted on the boiling curve coordinates along with the standard forced convection relation for the particular conditions of interest. The point where the two curves intersect is the solution to the system of equations and gives directly the

expected values of heat flux and wall temperature at which incipience will occur under the assumptions which went into the analysis. Example solutions are plotted in Figures 9 and 21 for the single-component Freon-113 and two-component air-Freon-113 cases, respectively.

With the preceding model in hand, one can now turn to a consideration of the predicted effects of parameter variation on incipience. It is easy to show that dissolved gas serves to promote incipience according to the model, resulting in a lower incipient wall temperature and heat flux. Although other factors are involved, this tendency can be seen most directly in the decrease of the adjusted saturation temperature with increasing dissolved gas content. Thus, the predicted incipient wall temperature for the relatively degassed case given in Figure 9 is 145°F while that for the gassy case at the same velocity given in Figure 21 is 127°F — although the predicted degassed $(T_w - T_{sat})$ is very nearly equal to the predicted gassy $(T_w - T_{satg})$. One important consequence of the earlier analysis is that dissolved gas may actually reduce the incipient wall temperature to a value below the "normal boiling temperature," T_{sat}.

In addition, the model predicts that increased inlet subcooling will result in increased incipient wall temperature and heat flux. This is easily seen from the fact that increasing subcooling shifts the forced convection curve up on the boiling coordinate plot (see Figure 13). This trend overshadows complications due to the fact that local subcooling is heat flux-dependent while inlet subcooling is not.

As long as the flow remains turbulent, increasing velocity has an effect analogous to that of increasing subcooling, according to the present model — pushing incipience to higher wall temperatures and heat fluxes (see Figure 21).

The real test of the analysis comes when its predictions are matched against the experimental results. In Figures 9, 13, and 21 the first thing to strike the observer is that, for the increasing heat flux traverse, nucleation is delayed far past the prediction. However, for the decreasing traverse, the boiling curve seems to merge with the forced convection curve near the predicted incipience point — indicating that, once initiated, nucleation dies out according to the analysis. Thus, some mechanism not accounted for in the analysis may be operating before nucleation is initiated by increasing heat flux. A model for this behavior is presented in the next section. For reasons detailed there, it is probably more meaningful to compare the point where nucleation dies with that predicted by the analysis.

From Figures 9 and 21, it appears that the analysis correctly predicts the directional effect of dissolved gas on the point where nucleation dies, but somewhat overestimates the size of the effect. Variations with subcooling are adequately predicted by the analysis over the present range of interest (see Figure 13). Judging from Figure 21, one can see that mass velocity effects are predicted quite well by the present method.

4.3 A Model for Hysteresis

Overall, the proposed analysis appears to adequately predict the point where nucleation dies. However, it clearly fails to explain the delayed nucleation behavior encountered on the increasing heat flux traverses. In an attempt to understand this discrepancy, a logical first step is to re-examine some of the explicit and implicit assumptions on which the analysis is based.

The most restrictive of the assumptions is probably the premise of quasi-equilibrium. Temperature gradients, other non-uniformities, and dynamic effects may make such a postulate tenuous at best. Attainment of equilibrium for the gassy cases is surely dependent on notoriously slow diffusion rates through the liquid. Thus, some inaccuracies in predicting dissolved gas effects might be expected. However, none of the above considerations seems to explain, in a consistent manner, the trends and size of the delays in nucleation which occurred.

One implicit, but very important, assumption in the incipient analysis is that surface cavities of all sizes are available for nucleation. For commercially-finished surfaces, such as those used here, a full size-range of cavities generally exists. However, the cavity "activity" or ability to initiate nucleation depends on many situational variables.

It is commonly believed that active sites are provided by cavities which contain some amount of surviving gas phase. Such pockets of gas can easily be maintained near the bottom of conical cavities for poorly

wetted solid-liquid combinations up to moderate values of subcooling. Pockets like these may be produced when a standing system is filled with liquid — trapping the gas phase in the cavities.

For nearly perfect wetting situations, such as Freon-113 on stainless steel, however, many of the cavities will probably be wetted and filled with liquid. For the idealized case of a conical cavity, all may be filled which have an included angle which is greater than the contact angle for the fluid-surface combination. Of course, real cavities are not, in general, conical, and it is logical that larger cavities will be more easily filled than smaller ones — especially when the size of microscopic impurities is of the order of the cavity size. From the above reasoning, a likely form for the distribution of active cavities in the present experimental situation is illustrated in Figure 22. If the preceding argument is valid, the main defect in the incipient analysis may lie in predicting the radius of the incipient cavity.

Using the experimental incipient wall temperatures and heat fluxes, one can "back out" the resulting idealized cavity radius from the incipient analysis. Combining Equations (4-19), (4-21), and (4-23) with Equation (4-11) or (4-17) gives

$$\frac{q/A}{k_\ell} r^2 - (T_w - T_{sat})\, r + 2\sigma \left.\frac{dT}{dp}\right|_{\substack{\text{at } p_\ell \text{ along the flat-} \\ \text{interface saturation line}}} = 0 \quad (4\text{-}28)$$

or

$$\frac{q/A}{k_\ell} r^2 - (T_w - T_{satg})\, r + 2\sigma \left.\frac{dT}{dp}\right|_{\substack{\text{at } p_\ell \text{ along the flat-} \\ \text{interface gassy} \\ \text{saturation line}}} = 0 \quad (4\text{-}29)$$

The latter equation was solved for the mass velocity series of runs, and the solutions grouped closely around $r = 1.40 \times 10^{-6}$ ft. According to the same equation, one may construct the locus of all possible combinations of heat flux and wall-saturation temperature difference for any given r. Results of this calculation for $r = 1.40 \times 10^{-6}$ ft, along with a similar curve for $r = 2.00 \times 10^{-5}$ ft (corresponding to the incipient analysis value for the lowest velocity), are shown in Figure 21.

It may be seen from the figure that the incipient points fall, with some scatter, around the curve for the smaller cavity radius. This behavior indicates that a relatively consistent size of equivalent cavity initiated nucleation and that this size was about an order of magnitude smaller than the sizes suggested by the incipient analysis. Essentially the same representative cavity radius was found to apply to the incipient data pertaining to other values of subcooling and dissolved gas content. For pool boiling of water, Torikai et al. [34] found a similar consistency in incipient radius with varying dissolved gas content.

Then, referring to Figure 22, one notes that, although a surface may contain a range of larger cavities ($r \geq r_{\text{incipient analysis}}$), nucleation must begin from one of the smaller <u>active</u> sites. It is clear from Equations (4-11) and (4-17) that the amount of superheat required to initiate nucleation increases with decreasing radius of a conical cavity. Thus, if cavities of the size range $r \geq r_{\text{incipient analysis}}$ are filled by a wetting fluid, nucleation may be delayed until the superheat achieved is adequate to nucleate the largest available cavity in the active size range.

When the first such cavity nucleates, it is likely that the resulting bubble may grow until it covers some neighboring larger cavities. If the liquid evaporates from these flooded cavities into the growing bubble, they may be, in turn, activated. If the number of such "oversized" (in relation to the imposed superheat) cavities present is relatively large, the spreading boiling region may improve the heat transfer mechanism so much as to drastically reduce the wall temperature. This sequence of events would explain the observed wall temperature discontinuity in the increasing heat flux portion of the hysteresis curve.

The "spreading" mechanism just described should not be confused with the "tripping" mechanism examined in Reference [20]. The former involves the drying out or seeding of inactive sites by spreading vapor bubbles while the latter refers to the triggering of meta-stable bubbles at active sites by local disturbances. Since disturbance levels are generally high in turbulent flow situations, it seems likely that the importance of the latter mechanism is limited to low velocity flow and pool situations.

For the decreasing heat flux traverse, the smaller cavities die out first, but the larger cavities remain boiling until the superheat is insufficient to support nucleation in them. Since, during the increasing traverse, the initially inactive large size range of cavities was activated, the decreasing traverse enjoys the availability of all sites specified by the surface distribution curve. Under this condition, the original assumption of the incipient analysis is essentially satisfied,

and one would expect its relatively good prediction of the merging of the partial boiling mode with the forced convection mode — which was noted in the previous section.

Bakhru [20] encountered hysteresis behavior in his experiments on pool boiling of Freon-113 from stainless steel tubes of the same stock as those used for the present runs. It is interesting to note that his incipient point data, when subjected to the present incipient equations, consistently give an incipient cavity radius within 5% of the value calculated earlier as being representative of the present flow boiling data. This result suggests that the filling of cavities is not sensitive to the particular orientation, method of immersion, or flow circumstances of the surface. The incipient radius may actually be a function of only the fluid-surface combination. At any rate, for the present situation, a consistent incipient radius is a good model for the data, and it appears that the size of this radius was predicted accurately by means of relatively simple pool boiling experiments which used the same fluid-surface combination.

Evidence of hysteresis may be found in the data of several other investigators. Marto and Rohsenow [35] got "bumping" excursions for pool boiling of sodium on nickel. Bankoff et al. [36] observed temperature overshoots for pool boiling of methanol from platinum. Hysteresis data for flow boiling of water have been taken by Bakhru [20], Hodgson [37], and Jordan and Leppert [38] on stainless steel; by Jeglic et al. [39] on Inconel X; and by Ricque and Siboul [40] on Monel. Unfortunately,

there was insufficient information provided in the above investigations to judge the success of the present model in predicting their results.

The model and analysis comprise an explanation which is consistent with the behavior encountered in the present experiments — delayed incipient nucleation and resulting hysteresis. Since the observed temperature overshoots present a formidable drawback to the otherwise excellent heat transfer characteristics of the subcooled flow boiling system, the next section will be devoted to a discussion of methods of preventing hysteresis.

4.4 Preventing Hysteresis

If the model of the preceding section is valid, it is clear that the way to prevent hysteresis is to provide active cavities of the correct size to initiate nucleation. In practice, this implies the use of a surface which prevents flooding of cavities in this size range.

One possible method is the coating of the cavity walls with some non-wetting substances. A good example is the application of Teflon to cavities for boiling in water. Bakhru [20] minimized hysteresis for flow boiling of water in an annulus by such a procedure. Unfortunately, Freon-113 on Teflon is a much better wetting situation, and Reference [20] shows that such a coating process had no effect on hysteresis in the Freon-113 boiling curve. Furthermore, no other coating substance is known to be "Freonphobic."

A second possibility is the manufacture of a surface which contains doubly reentrant cavities in the appropriate size range. It is well known that such cavities can remain active even up to relatively large values of subcooling [35]. However, the problem of actually producing such a surface is significant. It should be noted that it is not sufficient to provide merely a "rough" surface. In fact, a type of matrix or honeycomb structure is required which will provide stable bubble nuclei in the appropriate size range.

For the present investigation, one of the standard stainless steel tubes used for the heated length of the test section was specially coated by the Linde Division of Union Carbide Corporation with a porous matrix of stainless steel on the inner surface. Specifications on the coating included mean thickness = 0.012 in. and average void fraction = 0.375 and were tailored especially for the conditions of the runs shown in Figure 23.

The data for the commercially smooth tube under matching conditions are replotted in Figure 23 for comparison. In the single-phase forced-convection mode the coated tube shows somewhat better heat transfer characteristics, as would be expected since it is, in fact, "rough." Most important, the coated tube performance shows no incipient discontinuity with increasing heat flux as the partial boiling mode is entered. Through the partial boiling mode and into the fully-developed mode the coated tube curve follows the smooth tube curve very closely — consistently giving slightly lower wall temperatures. Coated tube data for the decreasing heat flux traverse coincide quite closely with the points

taken for increasing heat flux.

It seems from these results that the coating provided the active sites necessary to prevent delayed nucleation and, thus, hysteresis. Otherwise, the coating did not significantly alter the form or even the position of the boiling curve. This latter result may at first be surprising since it is clear that the smooth and coated surfaces have very dissimilar cavity distributions. However, as more fully explained in Reference [20], the consistency in the boiling curves is probably characteristic of the flow boiling situation. To activate a given number of cavities, a smooth surface generally requires a larger wall superheat than does a rough surface. Because of the relatively steep temperature gradients encountered in flow boiling, however, the difference between such required superheats is small compared to that pertaining to the analogous pool boiling case (see Reference [20]).

4.5 Flow Boiling Modes and the Relevant Saturation Temperature

Since, as noted earlier, saturation temperature is defined exclusively for equilibrium situations, one might question whether the variable deserves any place at all in analyses of the subcooled flow boiling process, which is inherently non-equilibrium in character. Furthermore, it has been shown that saturation temperature is highly dependent on the presence of a second component — for example, dissolved gas. Thus, such tenuous justifications for the present use of saturation temperature as a principal variable must finally rest on possible value in the presentation and explanation of experimental data.

For the degassed situation, it has long been clear that common boiling characteristics are observed on boiling plots employing T_{sat} in the abscissa construction. In particular, the fully-developed boiling portion of the curves generally show little sensitivity to subcooling and velocity when plotted on the standard boiling coordinates. Other conveniences are apparent in the relatively simple pressure-dependence adjustments in such plots which can be made to accurately model practical behavior. Finally, the standard plot is useful for attempts to delineate the ranges of the various modes of heat transfer in a certain situation. From the apparent usefulness of the saturation temperature for such purposes, one may conclude that the equilibrium concept does indeed have direct relation to the distinctively non-equilibrium process — that is, the saturation temperature is relevant.

The problem of assessing relevancy becomes somewhat clouded for the corresponding gassy case. From the previous discussion, analysis shows that dissolved gas should affect the incipient portion of the boiling curve, mainly through a change in quasi-equilibrium saturation temperature. Data presented in Figures 14 and 21 bear out this effect, although not quite to the predicted extent. Thus, it appears that T_{satg} is probably the relevant saturation temperature for gassy incipience.

After initial nucleation, the gassy boiling data in Figure 14 show wall temperatures considerably lower than those encountered for the same heat flux with degassed coolant, indicating significant dissolved gas effects until much higher heat fluxes are reached. At these higher

fluxes, there is no apparent difference between gassy and degassed wall temperatures, and T_{sat} appears to be the relevant saturation temperature.

All of the above observations point up a tendency which might be described as a continuous shift from dissolved gas-dominated to vapor-dominated behavior as heat flux is increased. Such behavior is illustrated by the curve in Figure 24 and can be rationalized by an orderly approach to the composite system characteristics. Recall first the physical picture of the situation in Figure 1 and the composite boiling curve in Figure 10. At incipience on the increasing heat flux traverse, the situation may closely approximate the quasi-equilibrium, two-component, two-phase model suggested in the incipient analysis, with allowance for delayed nucleation due to flooded cavities. This point, with just the exit (location of temperatures used in Figure 24) in nucleate boiling, represents the beginning of a degassing or dissolved gas-dominated heat transfer mode in which the gassy saturation temperature is the relevant one. After a small readjustment zone (see Figure 24), this mode plot takes on a steep slope much like that characteristic of single-component boiling.

As the heat flux increases, the incipient point moves toward the inlet to the heated section (see Figure 10), increasing the area in nucleate boiling. Since now the flow encounters a boiling region before reaching the exit section, some of the dissolved gas may be "stripped" from the coolant near the wall by this upstream degassing action. If diffusion processes are not sufficient to replenish the wall layer with

dissolved gas before reaching the exit area, the postulated two-component quasi-equilibrium model may not accurately represent the true situation, and a different type of gas-deficient "transition" mode may ensue. It seems reasonable that such behavior might be signaled by the slight decrease in slope of the boiling curve shown in Figure 24.

As the heat flux continues to increase, more heated section area will come into nucleate boiling until almost the entire upstream portion will be stripping dissolved gas from the wall layer. Thus, relatively degassed fluid will be exposed to the exit heated surface, and, when a sufficient level of heat flux and wall temperature is reached, one might expect the boiling curve to attain the characteristics of degassed, fully-developed boiling — that is, "vaporization" replaces "degassing" as the dominant mechanism. This view in reinforced by the apparent steepening of the boiling curve after the transition mode (see Figure 24), and by the merging with the fully-developed boiling data for the degassed case at higher fluxes (see Figure 14).

The traverse with decreasing heat flux encounters the same modes in reverse order until near the incipient point. For lower heat fluxes, nucleation persists, and the degassing mode is extended until the curve merges with that for forced convection.

Although the effect of dissolved gas on the boiling curve is appreciable, at least under certain conditions, there have been few investigations of this effect which employed measurement techniques accurate enough to allow adequate evaluation of quantitative results.

In particular, required accuracy in dissolved gas content and wall temperature are often elusive. McAdams et al. [41] noted that dissolved gas aided flow boiling heat transfer with water. Pike et al. [42] made similar observations for pool boiling of water and glycerin with dissolved air and carbon dioxide. Of more current interest is the work of Behar et al. [33] which gives a gassy boiling curve for water that shows a marked resemblance in form to that presented in Figure 24 for Freon-113. Thus, the proposed modes were duplicated for fluids with quite different properties.

Chapter 5

PRESSURE DROP

In the present context, the primary need for knowledge of pressure drop performance is related to assessing the feasibility of natural convection flow or the pumping power requirements of forced convection flow for a two-phase cooling system. Also, the local pressure level determines the governing local saturation properties which are important to any consideration of the phase-change mechanism.

For the vertical upflow case of interest here, the pressure level decreases consistently in the downstream direction according to the sum of the three components of pressure drop, gravity, friction, and acceleration:

$$p(z) = p(0) - \Delta p_{gravity} - \Delta p_{friction} - \Delta p_{acceleration} \qquad (5\text{-}1)$$

where the Δp's are pressure drops. In single-phase flow, the acceleration portion is zero (for a constant cross-section channel and incompressible liquid), and the friction and gravity components may be compared with conventional correlations. However, two-phase flow involves interdependence of the three components, and detailed knowledge of the situation is often required to assess their individual contributions.

As with heat transfer, the pressure drop behavior may be characterized by various modes — for example, single-phase and two-phase. However, it may happen that the effective boundaries between such hydrodynamic modes do not coincide with their thermal analogs. Thus, the point of net vapor generation (recall Figure 1) may mark the beginning of pressure drop divergence from single-phase behavior better than the incipient point. Flow regime changes may indicate transitions within the two-phase mode. After determining such mode limits, one faces the task of characterizing each mode by its particular pressure drop performance and dependence on relevant variables.

Breaking up the problem as suggested above may not simplify the approach as much as one might think. First, strong thermal-hydrodynamic interdependencies are present and show up in the limitation of the range of pressure drop data by the critical heat flux condition. Second, neither the suggested components of pressure drop nor the flow regime-related variables such as void fraction and slip ratio are easily separated or measured.

5.1 Composite Nature of the Data

As noted earlier, the total pressure drop sustained in a subcooled flow boiling situation is made up of three components. The data measurements necessarily consisted of <u>total</u> pressure drop measurements only. Any attempt to estimate the respective contribution of each component to the whole must include the use of peripheral data — for example, void fraction information.

Further, it should be kept in mind that the present data were taken from a single pair of pressure taps (see Figure 7 and Appendix A) immediately bounding the heated length. Thus, the pressure drop measured is an overall integration of local pressure gradients, governed by local hydrodynamic conditions, over the entire heated length. As such, the data allows no estimate of the detailed pressure profile as shown in Figure 1.

In the small body of literature on subcooled flow boiling pressure drop, there seems to be no general agreement on the best way to present data. The initial method used here is to plot pressure drop versus heat flux with other quantities as parameters. Although this approach may obscure some trends, it does permit easy comparison with corresponding points on the boiling curves. More fundamental plotting methods are attempted in the next chapter after a feel for the situation is developed.

5.2 Single-Phase Results

All single-phase data were taken for the case of turbulent, forced-convection flow. Representative results are given in Figure 25.

For comparison, the standard Nikuradse correlation for the frictional pressure drop component in smooth tubes (see, for example, Rohsenow and Choi [43]) with the correction for entrance effects from Deissler [25] is also presented in the figure, according to the relation

$$\frac{1}{f_F^{0.50}} = 4.00 \log_{10} (\mathrm{Re}\, f_F^{0.50}) - 0.40 \qquad (5\text{-}2)$$

where

$$f_F = \frac{\Delta p_{friction}}{\rho_\ell V^2/2g_c} \quad \frac{1}{4L/D} \quad \frac{1}{C_1}$$

and

$$C_1 = \frac{f_{F_{entrance}}}{f_F} = C_1 \text{ (Re, L/D)}$$

The experimental frictional pressure drop component was deduced by subtracting the gravity component,

$$\Delta p_{gravity} = \frac{\rho_\ell g L}{g_c}$$

from the measured total pressure drop. The relative size of the frictional component ranged from 3 - 25% of the gravity component for the single-phase runs. This fact rendered frictional data for the lowest velocity subject to relatively large scatter.

The solid points in Figure 25 are for adiabatic flow conditions while the open points are for heated runs in which the heat flux was just below that required for nucleation. It would be expected that the diabatic points would fall slightly below those for the adiabatic case because of reduced viscosity along the heated wall. This effect can be seen in the figure, but it is relatively small for the situations of present interest.

Overall, it seems that the data and the prediction very nearly coincide over the Reynolds Number range 9,600 - 43,000. Implicit in the above relationships is the fact that single-phase total pressure drop

increases with mass velocity because of contributions of the frictional component. This traditional trend will reappear in the single-phase portions of the curves which follow.

After the correspondence of the single-phase Freon-113 data with the Nikuradse correlation was established, the relationship was used for an instrumentation double-check preliminary to the boiling runs, as noted in Appendix D.

5.3 Parametric Effects

As with the case of heat transfer, it is convenient to investigate the pressure drop problem through an examination of parametric effects. Comments made in Chapter 3 concerning the difference between local and system approaches apply to the hydrodynamic situation as well. As an aid in interpreting the present results, the boiling incipience points (as indicated by the exit wall temperature) are marked on the pressure drop plots which follow. Void fraction information, which will be more fully explained in the next section and in Chapter 6, is also provided in the plots.

Representative data from a series of high flux runs whose purpose was to investigate mass velocity effects is given in Figure 26. As noted earlier, the single-phase data follow the Nikuradse correlation until the incipient point is attained. Higher pressure drop is sustained for higher velocity in this mode, as expected from frictional component contributions.

For the highest velocity case, boiling effects appear soon after the

incipient point and act to increase the total pressure drop as heat flux increases. A similar trend is found for the intermediate velocity, but the rise in pressure drop is smaller. The low velocity case shows no apparent variation from the single-phase prediction until the heat flux is raised far above that required to produce incipience. In contrast to the previous two cases, the two-phase situation results in an apparent decrease in pressure drop with increasing heat flux — although near the highest flux there are indications that the trend may be about to be reversed.

Figure 27 shows representative data from experiments meant to examine the effects of inlet subcooling on pressure drop. As before, subcooling effects on the single-phase forced-convection data are adequately modeled by the Nikuradse correlation. Thus, greater inlet subcooling produced slightly greater pressure drop because of the resulting increase of viscosity.

As the heat flux is increased past the incipient value, the curves show very similar behavior. In fact, the curves are nearly indistinguishable within the range shown — although the higher subcooling curve seems to decrease slightly before somewhat surpassing the lower subcooling curve in pressure drop at higher fluxes.

Results from a series of runs with variation of the dissolved gas content of the Freon-113 are given in Figure 28. As expected, such variation has no measurable effect on data in the single-phase forced-convection mode. For the low gas run, the total pressure drop remains

essentially at the single-phase level after nucleation was initiated — varying only slightly from that level at the highest heat flux point. The data for higher dissolved gas content followed the single-phase prediction to heat flux levels somewhat past incipience, but then showed a marked decrease in pressure drop — with some sign of trend-reversal at the highest fluxes used.

5.4 Void Fraction and Its Importance in Determining Total Pressure Drop

It is apparent from Figure 26 that the onset of divergence of pressure drop from the single-phase value coincides very closely with the appearance of measurable void fraction for both the high and low velocity cases. Some such correspondence can be found in Figures 27 and 28 as well, suggesting the possibility that void fraction information may help to characterize the observed two-phase behavior.

In addition to the quantitative void data presented in the figures, qualitative observations of the two-phase flow were made through the transparent sight section downstream from the exit. For gassy runs, small bubbles in the flow were visible soon after exit incipience, and the bubbly flow regime (with bubble size increasing with heat flux) seemed to dominate up to the highest fluxes. The transition between bubbly and slug flow nearly coincided with the highest flux run taken in each series. Experience and the Gambill correlation indicated that these points approached critical heat flux conditions very closely. For degassed conditions, no bubbles were visible until near the highest flux of the series.

Once established, bubbly flow (small bubbles) persisted up to the highest flux used for degassed runs.

Void fraction is known as one of the most important hydrodynamic parameters in the subcooled boiling situation and as one of the most difficult to measure. In particular, it is related to all three components of total pressure drop.

The effect of void fraction on the gravity component is quite direct and may be expressed in concise equation form in terms of the "static average density" as follows:

$$\Delta p_{gravity} = g \int_0^L \rho_{static}(z)\, dz \qquad (5\text{-}3)$$

where

$$\rho_{static} = \rho_g \alpha + \rho_\ell (1 - \alpha)$$

An exact analytical solution for the acceleration pressure drop in a practical situation requires detailed hydrodynamic knowledge which is very difficult to obtain. However, the important role played by void fraction in determining such results can be illustrated by means of a common model used for two-phase flow situations, the "homogeneous model." This approach assumes that gas and liquid phases flow with the same speed, i.e., the "slip ratio" is one. From momentum considerations (see, for example, Wallis [44]), the pressure drop due to acceleration is given approximately by

$$\Delta p_{acceleration} = \frac{G^2}{g_c} \left[\frac{1}{\rho_{static}(L)} - \frac{1}{\rho_\ell} \right] \qquad (5\text{-}4)$$

Formulation of expressions for the friction component proves to be more abstract, but most authors make use of the form familiar from single-phase work. The complexities are concealed in the problem of determining the appropriate two-phase friction factor to use for a given situation, for example,

$$\Delta p_{friction} = f_{TP} \; 4 \frac{L}{D} \; \frac{G^2}{2 g_c \rho_{static}} \qquad (5\text{-}5)$$

Ultimately, the appropriate friction factor may be specified in terms of variables which are directly dependent on void fraction.

The above observations serve to illustrate the fact that total pressure drop and each of its three components may be closely related to void fraction. One should realize that the nature of the relationship may be quite complicated and that only total-type data are available from the present investigation. Thus, Equation (5-3) requires a void fraction profile while only the exit void fraction was measured for these experiments. Equation (5-4) avoids the need for such detailed data, but it is a particular model whose assumptions are relatively restrictive. Still, it appears that void fraction may hold the key to understanding the total pressure drop behavior observed in Figures 26-28. The following chapter is devoted to an attempt to use the available void fraction information as an aid to characterizing that pressure drop performance.

Chapter 6

VOID FRACTION AND DISSOLVED GAS EFFECTS ON PRESSURE DROP

6.1 Bubble Collapse and Dissolved Gas Effects

One problem concerning the interpretation of the present void fraction data is that the measurements ascribed to the exit of the heated length were of necessity taken over a finite flow length somewhat downstream of the exit. Therefore, some consideration must be taken of possible bubble collapse occurring between the exit and measuring sections.

For idealized cases of bubble collapse under conditions related to the present ones, several investigators (see, for example, Florschuetz and Chao [45], Wittke and Chao [46], and Isenberg and Sideman [47]) have advanced theory-based predictions. General conclusions of the predictions for pure vapor collapse include separation of modes of collapse into inertia-controlled, heat transfer-controlled, and intermediate regions. When dissolved (noncondensible) gas enters the picture, predictions should be appropriately modified.

Shires [20] attempted to estimate the collapse of subcooled voids in Freon-113 by use of the analysis of Reference [45]. He found that the theory predicted a more rapid collapse than was encountered in his

experiments, by several orders of magnitude. By way of explanation, he attributed the apparent discrepancy to effects of bubble agglomeration, stratification, low thermal conductivity, and possible presence of dissolved gas effects.

Shires did undertake a prelimary degassing procedure, but, since he was not able to provide actual measurements of dissolved gas content, it is quite possible that a significant amount of noncondensibles was present for his runs. In light of present experience with the fluid and equipment, it appears that his degassing attempts were inadequate.

Although many of the assumptions concerning geometry, flow fields, and proximity effects are violated or, at least, intractable in the subcooled flow boiling situations of interest here, it was deemed appropriate to use some predictions to get rough estimates of the behavior which might be expected between the exit and measuring sections. Application of the analysis given in Reference [47] shows that, even for the case of the slowest predicted collapse, pure vapor collapse should have occurred before the bubbles were able to reach the measuring section (10 in. downstream of the end of the heated length).

Extending the theory, Reference [47] advances a model which shows dissolved gas effects can substantially decrease the collapse rate. In fact, their assumption of a constant mass of noncondensible gas within the bubble requires a solution which terminates with some remaining "persistent size" bubble.

Still, it remains to successfully establish the size of the constant

noncondensible mass in the bubble and, thus, determine the persistent size. Using the constant mass assumption and the perfect gas law, we have

$$\frac{p_{air_f}}{p_{air_o}} = \frac{T_{bubble_f}}{T_{bubble_o}} \left(\frac{r_o}{r_f}\right)^3$$

Assuming that the bubble is large enough so that

$$p_\ell >> \frac{2\sigma}{r}$$

then

$$p_{air_f} \simeq p_\ell - p_{sat}(T_\ell)$$

Also

$$T_{bubble_f} = T_\ell$$

Assuming further that the initial bubble contained an equilibrium partial pressure of air, we find

$$p_{air_o} = \frac{K(T)}{X_{air}}$$

where, for the present case, it makes no significant difference which temperature is used to evaluate K(T). By the arguments presented in Chapter 4, the only consistent temperature to use for the initial bubble temperature is the gassy saturation temperature corresponding to p_ℓ

and X_{air} — that is,

$$T_{bubble_o} = T_{satg}(p_\ell, X_{air})$$

Since the bubble volume fraction is directly related to the void fraction, we have finally

$$\frac{\alpha_f}{\alpha_o} = \left(\frac{r_f}{r_o}\right)^3 = \frac{\frac{X_{air}}{K(T)}}{p_\ell - p_{sat}(T_\ell)} \frac{T_\ell}{T_{satg}(p_\ell, X_{air})} \qquad (6\text{-}1)$$

One obvious consequence of this analysis is that, for $T_\ell \geq T_{satg}(p_\ell, X_{air})$, there is no gassy bubble collapse. This result is reasonable under the assumptions given when one recalls that the bubble is no longer subcooled (in the sense of "removed from equilibrium") for the above conditions, even though $T_\ell < T_{sat}(p_\ell)$. At this point, one might even question whether it is appropriate to regard $(T_{sat} - T_\ell)$ in the Jakob number of the conventional theories as the heat transfer driving force. It may be that additional slowing of the gassy bubble collapse can be modeled by employing the above idea, a recurrence of the problem of relevant saturation temperatures which was examined in Chapter 4.

The gassy form of the Isenberg and Sideman prediction indicates that collapse to the persistent size should have occurred for the present conditions before the vapor-gas bubbles reached the measurement section. Thus, if the models here are valid, it is possible to estimate the exit void fraction from the measured void fraction for the gassy case. The

gassy data given in Figures 26-28 are the results derived from applying Equation (6-1) to the void measurements. It should be noted that the largest value of $(\alpha_o - \alpha_f)$ was for the lowest measured void fraction of the low velocity series and that this difference was less than 0.01.

Visual observations made through the transparent sight section in the high flux loop serve to further substantiate the explanations offered above. For degassed runs, when bubbles were present, there was a clearly noticeable trend toward collapse as the voids traveled through the section. Near critical heat flux, the violent collapse of large vapor bubbles was evident. However, for gassy runs, observations provided no indication of bubble collapse. Even near critical heat flux, the flow exhibited a comparatively stable void appearance. The data of Shires show similar delayed collapse — pointing up the likelihood of dissolved gas effects dominating his results.

In summary, this section has shown by means of rough but tractable models and visual observations that the effect of gassy bubble collapse on measured exit void fraction is probably small for the present cases, but that pure vapor bubbles probably collapse before reaching the measurement section. Thus, it is likely that the lack of measurable voids for the degassed case in Figure 28 is due to inadequate measurement techniques. In view of the rapid collapse of subcooled, degassed voids, it appears that, for good accuracy in this case, one must resort to measurement methods which may be implemented very close to the end of the heated length. Of the techniques currently available, radiation absorption probably offers the best chances for success. Although fairly cumbersome

and involved, the method has been used to advantage by other investigators (see, for example, Reference [19]).

6.2 Parametric Effects

One of the first things to be noticed about the data in Figures 26-28 is that no measurable ($\geq$0.02) void fraction was present at the exit until the heat flux was raised considerably above that required to initiate nucleation. The very great increase in exit void fraction for the gassy case over the degassed case is obvious in Figure 28. In fact, no measurable voids were present for the degassed case until the highest heat flux shown was attained.

From Figure 26, it can be seen that the effect of increasing mass velocity is of two types: (a) delay of significant voids to higher fluxes and (b) stretching of the region of void fraction increase over a wider range of heat flux.

Figure 27 shows that the delay of significant voids occurs with increased inlet subcooling in much the same way as with increased velocity. However, the form of the curves is very similar — that is, no stretching of the void curve is apparent. The slightly larger dissolved gas content for the higher subcooling would be expected to somewhat counteract the delay by imposing a smaller collapse rate and a larger persistent size.

6.3 Correlation With Quality and the Point of Net Vapor Generation

As a first effort toward understanding the void fraction picture, the previous data are replotted with quality (recall Equation (1-3)) as the abscissa in Figures 29-31. It can be shown that this approach takes account of certain aspects of the mass velocity-subcooling effects by reducing the local conditions to a type of common denominator, the enthalpy-based quality. A measure of the success of the venture is the fact that the various void curves in Figures 29 and 30 are very similar in both form and location on the quality abscissa. This method of presentation also allows interpretive assessments of exit subcooling.

It was noted earlier that the presence of measurable exit voids very nearly coincided with changes in total pressure drop behavior. From the form of the void fraction curves, it seems likely that the point of first measurable voids may correspond to the behavioral definition of the point of net vapor generation (recall Chapter 1 and Figure 1) — the point where a rapid increase in void fraction begins.

Several analytical models have been proposed to predict the point of net vapor generation. Two of these, by Levy [2] and Staub [3], are quite similar in approach. Both use a force balance on an idealized departing bubble in combination with the turbulent temperature profile to mark the beginning of the characteristic rapid rise in void fraction. However, differences occur in their treatment of the frictional or drag force and the buoyancy force. Levy states that, for the cases of interest to him, the buoyancy force was negligible. For the conditions

of present interest, such an approximation is incorrect, and the more complete formulation by Staub was used (see Appendix F).

The specific output of the Staub equations is the local bulk subcooling at the net vapor point $T_{sat} - T_b(z)$. It is suggested that this result be simply modified to $T_{satg} - T_b(z)$ to account for dissolved gas effects. Unfortunately, the Staub prediction contains one constant in the expression for the surface tension force which is not at all well specified. A suggested outside range is given in Reference [3], and the largest value was chosen for use here (see note in Appendix F).

Results of applying the Staub analysis in the above form to the present experiments are shown in Figures 29-31. Considering the restrictions and idealized nature of the model, one finds rough agreement with the points of first measurable voids. In general, the analysis predicts that net voids will occur somewhat earlier than the experiments showed. One possible factor contributing to this result could be that, since the points are somewhat past the incipient point, the two-component equilibrium saturation temperature may not be the relevant one (recall Chapter 4). A more representative value is probably between T_{satg} and T_{sat}. It can be seen in Figure 31 that the present range of dissolved gas content does have a significant effect on the prediction. However, as noted before, the degassed data point in that figure is probably not a good indication of the actual exit conditions. Use of smaller values of the surface tension constant would result in shifting the predicted points to the left in Figures 29-31.

One may note that the runs given in Figure 31 very nearly reached the zero quality exit condition — the boundary between subcooled flow boiling and bulk flow boiling (recall Chapter 1 and Figure 1). For these particular conditions, it is interesting to compare the data with a prediction from the homogeneous equilibrium model for the positive quality region. The essential assumptions are (a) equal gas and liquid flow velocities and (b) thermodynamic equilibrium. Thus, the model situation is one in which the entire flow is at the saturation temperature and in which all the heat added to the flow goes into the formation of vapor. Specifically, the situation requires that the static average density equal the flow average density — that is,

$$\rho_{static} = \rho_{flow}$$

or

$$\rho_g + \rho_\ell(1 - \alpha) = \frac{1}{\frac{\chi}{\rho_g} + \frac{(1-\chi)}{\rho_\ell}}$$

and

$$\alpha = \frac{1}{1 + \frac{1-\chi}{\chi}\frac{\rho_g}{\rho_\ell}} \qquad (6\text{-}2)$$

Equation (6-2) is plotted for the present variables in Figure 31. It appears that the gassy void fraction data would nearly merge with the homogeneous prediction if the trend could have been extended into the positive quality region. In actuality, however, the data would be expected to cross the homogeneous prediction near zero quality and remain

somewhat below it up to relatively high qualities, where the two curves finally merge. This behavior is due to the development of slip velocity between the two phases (in the eventual form of a high-velocity vapor core) and/or to the storage of superheat in the liquid phase.

Because of critical heat flux limitations, it was not possible to obtain data in the positive quality region with the present setup. Extensive apparatus modifications would have been necessary to accommodate the longer heated lengths required to investigate this region.

6.4 Using Void Fraction Information to Estimate Components of Total Pressure Drop

The logical next step is to attempt to explain observed total pressure drop behavior by use of the accrued exit void fraction information. Referring to Equation (5-3) for the gravity component of total pressure drop, one finds that rigorous evaluation of the expression requires knowledge of the entire void profile, $\alpha(z)$, along the heated length. It is important to realize that the present data do not provide this specific information directly — that is, Figures 29-31 give $\alpha_{exit}(\chi_{exit})$ rather than $\alpha(z)$ or $\alpha[\chi(z)]$. To bridge this gap in knowledge, it is proposed to use a reasonable averaging procedure.

Assuming for each series of runs that void fraction is a function of quality, we have

$$\alpha = \alpha(\chi)$$

and

$$\rho_{static} = \rho_{static}(\chi)$$

so that

$$\Delta p_{gravity} = \frac{gL}{g_c(\chi_{exit} - \chi_{in})} \int_{\chi_{in}}^{\chi_{exit}} \rho_{static}(\chi) \, d\chi \quad (6\text{-}3)$$

For the interval $\chi_{measurable\ voids} \leq \chi \leq \chi_{exit}$, α can be taken from the data in Figures 29-31. There are no voids for the interval $\chi_{in} \leq \chi \leq \chi_{incipience}$. As a reasonable approximation for the intermediate region of small boundary layer voids, $\chi_{incipience} \leq \chi \leq \chi_{measurable\ voids}$, it is proposed to use a linear relation connecting the appropriate values at each extreme.

Using the homogeneous model presented earlier, one can predict the acceleration component from the exit void fraction data. Unfortunately, this leaves the friction component, for which no adequate subcooled flow boiling version seems to exist. Rather than to present the friction component as a sort of experimental leftover, it is deemed useful to subtract the gravity component estimate given by Equation (6-3) from the total pressure drop data given in Figures 26-28. The resultant composites of the acceleration and friction components are shown in Figures 32-34. This form can be used for comparison to a pressure drop correlation for subcooled flow boiling suggested by Bergles and Dormer [48].

6.5 Comparison of Reduced Pressure Drop Data With a Correlation for the Friction and Acceleration Components

Reference [48] presents a correlation which was developed with data taken from low pressure experiments with subcooled flow boiling of

degassed water in horizontal tubes. The method was used successfully to account for mass velocity, subcooling, and pressure level effects on water data over a wide range of conditions.

The abscissa used for the correlation plots is constructed as a dimensionless heated length. The numerator L_b is the length of the boiling portion of the heated section — that is, the distance from the incipient point to the exit of the heated section. The denominator or reference length $L_{b,s}$ is that heated length which would be required to bring the fluid from the given inlet conditions to the saturation condition corresponding to the pressure at the exit of the heated section.

For high heat fluxes, the incipient point is quite near the inlet to the heated length, and $L_b \simeq L$. Under the present conditions, it was assumed that this relation held for heat fluxes higher than that required for incipience at L/D = 4, the location of the wall thermocouple nearest to the inlet.

When dissolved gas is present, there is some question as to what the appropriate saturation condition for calculating $L_{b,s}$ should be. If the equilibrium analysis of Chapter 4 applies in some region, it seems that the required saturation condition is that specified by $T_{satg} = T_{satg}(p_{\ell_{exit}}, X_{air})$. In the figures that follow $L_{b,s}$ will denote the reference length calculated from $T_{sat}(p_{\ell_{exit}})$. and $L_{b,sg}$ will denote that found from $T_{satg}(p_{\ell_{exit}}, X_{air})$.

The ordinate used in the plots is a dimensionless pressure drop. The numerator Δp_b is the pressure drop (friction + acceleration) sustained

over the boiling length. The denominator $\Delta p_{a,s}$ (or $\Delta p_{a,sg}$ for the gassy case) is the friction pressure drop which would be incurred by the flow of fluid through a similar tube of length $L_{b,s}$ (or $L_{b,sg}$) under adiabatic conditions with the bulk fluid temperature constant at its value at the incipient point.

Three pairs of plots are used to present the friction-acceleration components obtained from the present data for Freon-113. One member of each pair is plotted on the traditional (degassed) coordinates, and one is plotted on the proposed (gassy) coordinates. For comparison, the curve proposed in Reference [48] for L/D = 25 (corresponding to the present L/D = 24) for water is also given in each of the figures. It should be noted that this reference curve was taken from data with ordinate values $\leq$ 2.00.

From Figure 35, one can see that data for the two highest velocities fall relatively close together and somewhat above the reference curve. After measurable voids appear at the exit, these data tend more toward the reference curve. For the low velocity series, the data for low fluxes fall quite near to the reference curve but bend somewhat below it thereafter.

On gassy coordinates in Figure 36, the same data show a close correspondence to the reference curve up to the point where measurable voids appear for the higher velocities. Thereafter, the experimental points fall below it.

The form of the data in Figure 37 largely resembles that of Figure 35 —

with points exceeding the reference until the presence of measurable voids and subsequently tending toward it. Further, Figure 38, as Figure 36 before, shows a good match on gassy coordinates between reference and data for low flux behavior and divergence with the appearance of significant voids.

Figures 39 and 40 provide a comparison of the gassy-degassed series of runs. The behavior illustrated for the degassed case seems contradictory and unlikely in light of the other data. As noted earlier, the void fraction data for the degassed case probably seriously underestimated the actual voids present in the heated length. This would result in subtracting too large a gravity component from the total pressure drop raw data. In turn, for high heat fluxes, the combination friction-acceleration pressure drop component derived and presented in Figure 39 is probably smaller than that actually present. Thus, the actual degassed curve would be expected to be much closer to the gassy curve — probably of a similar form and somewhat below it.

Overall, the correlation coordinates seem to take reasonable account of the mass velocity and subcooling effects, as indicated by the proximity of the curves to one another. The results for low velocity seem somewhat out of line, but the data which went into the reference curve (minimum velocity = 5.00 ft/sec) showed a similar directional shift with velocity. The size of the pressure drops decreased, and the experimental uncertainty increased with decreasing velocity.

In a strict sense, there is no reason why gassy Freon-113 and degassed

water should share the same correlation curve, even with use of the gassy coordinates. Still, by use of the proposed modification to the plots, it can be seen that, for gassy runs, there seem to be indications of several modes operating within the two-phase region. With partial reference to the heat transfer discussion, one might roughly classify these as gas-dominated, transition, and vapor-dominated. For small voids, gas quasi-equilibrium conditions may apply, T_{satg} may be the relevant saturation temperature, and a reference correlation such as that shown may adequately predict the data on gas-adjusted coordinates. As voids become a significant portion of the volume flow, diffusion processes may be too slow and/or dissolved gas supply inadequate to maintain the validity of the gassy analysis. Then, the normal one-component saturation temperature T_{sat} may become the relevant one, and the unadjusted reference curve may prove adequate.

6.6 Summary of Pressure Drop Behavior

This section is devoted to bringing the diverse elements of Chapters 5 and 6 together into a composite picture of pressure drop behavior.

For the range of variables encountered in the present study, the gravity term is the largest of the components of total pressure drop. As heat flux is increased, the gravity component maintains essentially its single-phase liquid value until well after nucleation is initiated. When the point of net vapor generation is reached at the exit section, rapidly increasing void fraction acts to decrease the static average

density of the mixture in the heated length. This, in turn, produces a significant decrease in the size of the contribution of the gravity component to the total pressure drop. Further increase in heat flux moves the net vapor point upstream and causes additional decay of the gravity component.

The friction-acceleration component is completely dominated by the friction term in the single-phase liquid region and is given by traditional correlations. Immediately after boiling incipience, friction probably still dominates this term and increases because of the presence of the bubble boundary layer near the tube wall. As increased heat flux produces significant void fraction, the acceleration portion probably becomes of a size comparable to that of the friction portion, and the two act together to cause a rapid rise in the friction-acceleration component.

For low velocities, increases in the friction-acceleration component are insufficient to overcome the decrease in the gravity component at low void levels. Thus total pressure drop decreases until higher heat flux and void conditions are attained, where the fast-growing friction-acceleration term is finally able to arrest the decrease of the composite.

At higher velocities, the larger friction-acceleration term is capable of preventing any decrease in total pressure drop. However, any rapid increase is significantly hindered by the conflicting trend of the gravity component until much higher heat fluxes and void fraction are achieved.

The direct effect of the presence of significant dissolved gas is apparently a drastic reduction in the collapse rate of bubbles formed. This serves to increase the void fraction for given conditions over that which would obtain for the degassed case. The ultimate effect is to shrink the region of single-phase domination of total pressure drop components and hasten the point where void fraction significantly changes the relative sizes of the components.

Comparison of data with a correlation for the friction-acceleration component showed reasonable agreement in mass velocity and subcooling effects. Dissolved gas results appeared to show trends from gas-dominated to vapor-dominated behavior which complemented observations made in the earlier discussion of heat transfer.

Chapter 7

CONCLUSIONS

The studies presented in the preceding chapters have provided information on heat transfer and hydrodynamic behavior for subcooled flow boiling of a fluorocarbon representative of a group suitable for use in the cooling of high-power-density electronic components. Specific problems arising from the excellent wetting characteristics and large solubility constants of fluorocarbons were also examined.

Heat transfer in the single-phase region was adequately represented by standard correlations for turbulent flow in tubes. In the two-phase region, however, boiling curves had a unique form dominated by large, discontinuous jumps in wall temperature at the incipient point on increasing heat flux traverses. Parametric effects of mass velocity and subcooling on two-phase heat transfer generally followed conventional trends. Techniques were devised for accurate determination of the temperature dependence of the air-coolant solubility constant and for measurement and control of dissolved gas content in the main experimental loop. Dissolved gas effects were found to increase heat transfer significantly in the partial boiling mode. Data in the fully-developed boiling mode were successfully described by modifications of existing

correlations. Critical heat flux data showed that a conventional correlation provided, at best, an upper bound for the parameter range of interest.

An analysis for determining the saturation temperature adjusted for the presence of dissolved gas was incorporated into a prediction for boiling incipience. Decreasing heat flux traverses showed approximate agreement with the resulting predictions. A model was presented for predicting the delayed nucleation experienced for increasing heat flux traverses. On the basis of this model, a method for preventing cavity flooding and resultant hysteresis was suggested and successfully implemented by means of a special surface coating. The apparent transition encountered in gassy boiling heat transfer from gas-dominated to vapor-dominated modes was described with reference to appropriate saturation temperatures.

Standard correlations adequately represented pressure drop performance in the single-phase region. Parametric effects on two-phase total pressure drop were illustrated and discussed.

Three novel techniques — photographic, trap, and capacitance — were employed to obtain accurate void fraction measurements. An examination of bubble collapse effects on void fraction showed that dissolved gas drastically retarded collapse rates for the parameter range of interest. Parametric effects on void fraction were presented and correlated with some success on quality coordinates. An existing analysis for predicting the point of net vapor generation was compared

with void fraction data and gave approximate agreement using a selected value for a relevant proportionality constant.

Void fraction information was used to estimate the gravity component of the total pressure drop. The remaining friction-acceleration component data were plotted on coordinates suggested in an existing correlation. Modification of the coordinates to account for dissolved gas content resulted in fair agreement with the correlation curve. A qualitative description of the gas-dominated to vapor-dominated transition in pressure drop performance, analogous to that for heat transfer, was presented. A comprehensive explanation of the behavior of the various pressure drop components was offered.

Appendix A

LOOP AND TEST SECTION DETAILS

A.1 Low Flux Loop and Test Section

The following descriptions refer directly to equipment illustrated in Figures 2, 3, and 4.

A 2-gal stainless steel tank, fitted with a sight glass to indicate coolant level and a water-cooled glass condenser (Graham type, Model 2560 by Corning Glass) to minimize evaporation of the coolant through the vent, served as the reservoir.

From the reservoir, the test fluid entered the suction side of a centrifugal canned-rotor type pump, Model 810E by Dynapump. Pump speed was regulated by a Variac transformer within a limited range.

A Brooks Rotameter, Model 1110, with a range of 0-1.00 gpm of Freon-113 was located downstream from the pump to monitor flow rate to the test section. Float type RV was used to give maximum immunity to viscosity variations.

Next the test fluid passed through the tube side of a Ross BCF 502 single-pass, shell-and-tube heat exchanger. A mixture of hot and cold water flowed through the shell side of this "preheater" section

and was adjusted to give the test fluid any required inlet temperature.

Flowing from the flow meter through the test section, the coolant was directed to the tube side of a Ross BCF 603 shell-and-tube heat exchanger. The shell side was supplied by cold water and provided for complete condensation and/or dissolution of any gas-phase component of the flow emanating from the test section during boiling experiments. At this point the fluid was ready for recirculation in the loop.

A bypass leg between the pump outlet and the reservoir allowed for pressure level adjustments within a limited range. Piping was of 5/8-in. nominal copper with both soft and silver-soldered sweat joints. Threaded connections were sealed with 1/2 in. Teflon tape dope. A Henry diaphragm valve was used for throttling upstream of the inlet to the test section. All other valves were Jamesbury ball valves with Teflon seats. A framework of Dexion slotted angles provided support for the entire loop.

The heated portion of the low flux test section consisted of a horizontal assembly of 14 Pyrex 7740 glass tubes, each 15 in. long and coated on the outside with a very thin, electrically conducting film of tin oxide for 13 in. of its length. These tubes were approximately 70 percent optically transparent so that visual observation of the boiling internal surface was possible. The manufacturer, Corning Glass Works, listed the nominal thickness of the film as 16 microinches. All tubes were precision ground to an inside diameter of 0.433 in. and an outside diameter of 0.510 in.

Seven Variac transformers controlled the AC power used for heating,

with each transformer feeding two tubes. Variable trimming resistors were connected in series with the tube with lower overall resistance to compensate for the resistance difference between pair members. Connections from transformer to tube were made by spring-clipping a lead wire to a section, at each tube end, which was covered with silver-base paint.

Immediately downstream from the heated section were two 15-in. adiabatic sections. The first consisted of an electronic void sensor and two short Pyrex adapter sections as shown in Figure 4. The second was a plain Pyrex glass tube of the same dimensions as those mentioned before.

A framework of Dexion slotted angles held a series of Plexiglas plates in which were mounted the O-ring couplings used to smoothly connect the tubes. Rigidity and alignment was assured by three 1/2-in. drill rods which extended through the plates over the entire test section length.

For monitoring purposes, flow rate was indicated by the loop flow meter; pressure level by a 3-1/2 in. Helicoid compound gauge, 30 in. Hg vacuum to 15 psig; and test section power by two Westinghouse portable single-phase wattmeters, Type PY-5. Bulk temperatures of the coolant were obtained from four centerline thermocouples mounted in Conax packing glands, two upstream and two downstream of the void sensor in adjacent coupling sections. These thermocouples were 30-gauge iron-constantan with beads formed by a Dynatech thermocouple welder and with output reported through a Leeds and Northrup Speedomax Multipoint Recorder with Cleertrend printing. For control purposes, sampling temperatures of the external walls of the heated tubes and of the void sensor were recorded by means

of other such thermocouples connected to the same instrument.

Two separate measuring systems provided data on void fraction in the low flux loop. The first was an Ikor V/L Measuring System, Model 545-2, including a capacitance sensor section mounted on-line and a remote electronic readout package. Further details on this instrument are included in Appendix B. The second system was photographic and consisted of a Polaroid Model 110B camera using an auxiliary closeup lens set, high-speed film and indirect floodlighting. Pictures were taken through the 15-in. clear glass section immediately following that of the sensor. In order to avoid distortion due to the curvature of the tube, a trough-like Plexiglas jacket was installed around it, the jacket was filled with a refraction index-matching fluid (Nujol) until the tube was covered, and pictures were taken through the bath so formed.

A.2 High Flux Loop

The following descriptions refer directly to equipment illustrated in Figures 5 and 6.

A stainless steel tank 10 in. in diameter and 10 in. high served as a combination reservoir and degassing tank. Its capacity was adequate to provide make-up liquid for small leakages incurred during long periods of operation. Heat for degassing purposes in the tank was supplied by two 2000-watt Chromalox immersion heaters installed near the bottom of the tank. A single Powerstat transformer mounted on the control panel bench served to regulate the power to the heating elements. The top of the tank was vented to the atmosphere through a glass coil-type, water-cooled condenser in order to prevent excess loss of coolant by evaporation.

A valve-controlled inlet at the top of the tank provided for a recirculating bleed flow during degassing sequences. The coolant level was indicated by a sight glass fitted to the side of the tank.

From the reservoir, the fluid passed through a stainless steel FulFlo filter rated at 10 gpm and charged with a cartridge of viscose filter media having a nominal rating of 20 microns. Shell gasket 31300 by FulFlo was used in order to insure compatibility with the fluorocarbons.

Next the coolant passed through a Sporlan two-stage Catch-All filter-drier, Model C-969. This device with use of Sporlan RC-4864 dessicant cores provided further filtration and virtually complete dehydration of the refrigerant.

After the decontamination stages mentioned above, the test fluid entered the suction side of an Ingersol-Rand centrifugal pump, Model 1-1/2 RVH 7-1/2, rated at 40 gpm Freon-113 at a head of 90 psi. This model incorporated a bronze casing and impeller as well as mechanical seals. A Marathon Electric drip-proof AC electric motor drove the pump at 3450 rpm. At this speed, the motor was rated at 7-1/2 hp for 220-volt, 3-phase, 60-cycle alternating current. A 3-1/2 in. Helicoid compound gauge, 30 in. Hg vacuum to 15 psig, was installed on the suction side of the pump to aid in maintaining an inlet pressure sufficient to avoid cavitation within the pump.

Two vertical float-type flow meters by Fisher and Porter installed in parallel served to monitor the flow rate to the test section over alternate scales of 0-4.25 gpm water or 0-1.00 gpm water. These scales

were easily convertible to Freon-113 flow rates by use of the manufacturer's specifications.

Flowing from the flow meters through the test section, the coolant was directed to an American Standard BCF 4-pass shell-and-tube heat exchanger rated at 30 gpm water on either side with a heat load of 100,000 Btu/hr. The shell side carried the test fluid while the tube side was connected to the city water supply. This equipment was sized so as to provide for complete condensation and/or dissolution of any gas-phase component of the flow emanating from the test section during boiling experiments. At this point the fluid was ready for refiltration and recirculation in the loop.

The circuit just traced was that of the primary flow. There were several other piping legs outside this circuit which served auxiliary functions. A line for the previously-mentioned bleed flow ran from the inlet side of the heat exchanger back to the reservoir-degassing tank. Four additional legs allowed pressure level regulation by acting as adjustable bypasses and flow reversal elements. A gas vent was located at a high point following the flow meters, and two drains, one at the pump inlet and one on the low side of the heat exchanger, permitted easy flushing of the system.

The main piping was 1-in. nominal copper tubing with high-strength 95-5 solder used to sweat all joints. Jamesbury ball valves with double Teflon seals were used in primarily on-off situations, while Henry diaphragm valves were used where control and/or throttling were most important. All unions were provided with Teflon gaskets to insure tight joints

with a minimum of galling. The support framework for the entire loop was constructed of Dexion slotted angles.

Electrical power for heating the test section was provided by two 36-kw DC generators connected in series and located adjacent to the loop. Each generator was rated at 12 volts and 3000 amperes. A power control console permitted coarse or fine adjustments through the range 0-24 volts by means of air-cooled Ohmite resistors. Power was transmitted from the generators through large copper-bar busses which connected to the loop by water-cooled, braided-copper power leads. Details on the measurement of input power are included in the section on the high flux test section.

A.3 High Flux Test Section

The inlet side of the test section was insulated electrically and mechanically from the rest of the loop piping by a short length of Buna N tubing. From this flexible leg, the coolant flowed through a Henry diaphragm valve to an insulated length of brass pipe and fittings and then to the lower end of the heated length. Main flow throttling was accomplished at this inlet valve, very close to the heated length in order to minimize the possibility of the development of flow instabilities during two-phase operation. Samples for determination of dissolved air content were drawn from a valved port in the brass inlet leg and introduced directly into an Aire-Ometer AD-4002 measuring device (see Appendix C). Inlet bulk temperature was indicated by a 30-gauge iron-constantan

centerline thermocouple mounted through a Conax packing gland in the brass inlet leg.

A detailed drawing of the heated length of the test section is shown in Figure 7. The primary element consisted of a 15-in. length of 304 stainless steel tubing with an inside diameter of 0.500 in. and a wall thickness of 0.010 in. Brass bushings soldered to the ends of the tube acted as electrical connectors for the 12-in. conducting portion. Aluminum buss bars securely clamped to the bushings served as links and supports for the water-cooled copper leads from the DC generators. The tubing material and dimensions were chosen so as to provide for impedance matching with the power source, resistance to fouling, accurate wall temperature measurement, and characteristics of a common-type engineering surface.

A pressure tap hole was drilled 1/8 in. from the inner edge of each bushing through the bushing with a No. 60 drill and through the tube wall with a No. 80 drill. The hole was then deburred, and a small gauge stainless steel tube was soldered over the hole on the outside of the bushing. Each small tube was connecting by a Conax packing gland to a length of Buna N tubing which in turn connected to the central pressure tap manifold.

Six 30-gauge iron-constantan thermocouples were attached to the outside tube wall as shown in Figure 7. A small chip of mica under each thermocouple electrically insulated it from the heated tube surface. Attachment and primary thermal insulation of each thermocouple was provided by wrapping with 3M No. 27 glass cloth tape.

Two 0.005-in. diameter copper-constantan thermocouples were attached to the tube wall in a similar manner 0.50 in. from the exit end of the 12-in. conducting portion. These were indicators meant especially to detect a critical heat flux situation early enough for the experimenter to act to avoid the onset of destructive burnout.

To minimize heat loss and maximize wall temperature measurement accuracy, a guard heater and insulation assembly was mounted around the heated length. A 12-in. length of 1-1/2 in. copper tubing slit and wrapped with glass-insulated Kanthel heater wire in three sections surrounded the stainless steel tube. Asbestos fiber filled the space between the two tubes. Six 30-gauge iron-constantan thermocouples were attached to the inside surface of the copper tube as shown in Figure 7. The leads from these thermocouples, along with those from the eight tube wall thermocouples, extended from the two small slits in the copper tube. Each of the three sections of Kanthel wire was connected to a Variac transformer which regulated AC power input for a range of 0-120 volts.

Flow from the heated length passed through a short brass and nylon length where an 0.005-in. diameter copper-constantan thermocouple was mounted in a hypodermic needle on the flow centerline to indicate exit bulk temperature. This length was electrically insulated from the heated length by the nylon buffer and thermally insulated by a thick wrapping of glass fiber material.

Next the flow passed through the trap and sensor sections detailed in Appendix B and continued to a flexible Buna N outlet hose which directed the coolant to the main loop piping.

All thermocouple beads were formed by a Dynatech welder. Outputs from the iron-constantan thermocouples were recorded by a Leeds and Northrup Speedomax Multipoint Recorder. Copper-constantan thermocuples were all connected to ice junctions with one exit thermocouple's output being recorded continuously on a Honeywell chart recorder and the output from the others being measured on a Leeds and Northrup K-2 precision potentiometer.

Pressure level measurements were made by opening the appropriate valves in the central pressure tap manifold to connect the tap leads to two Helecoid 8-1/2 in. pressure gauges with range 0-30 psig mounted on the main control panel. Pressure drop measurements were made by connecting the tap leads to opposite sides of a two-fluid manometer containing Freon-113 liquid and Meriam red liquid (S.G. = 2.95) as the working fluids.

Power measurements for the heated length were accomplished by separate methods for determination of DC voltage and current from the generators. Voltage was taken from a Digitec digital voltmeter connected by clip leads directly to the aluminum buss bars of the heated length. Current was determined from the voltage measured across a shunt calibrated by the National Bureau of Standards.

Void fraction was determined from the direct trap readings and/or the remote capacitance readings. Appendix B details the various readout options possible with these devices.

Appendix B

VOID FRACTION MEASUREMENT

In the history of boiling investigations, many different approaches have been taken toward solving the problem of void fraction measurement. Indirect measurement methods include deduction of void fraction from measures of acoustic velocity, dielectric constant, electrical resistivity, permeability, viscosity, thermal conductivity, particle absorption (alpha, beta, and neutron), radiation absorption (microwaves, infrared, visible, ultraviolet, gamma, and X-rays), and concentration of dissolved radioisotopes in the two-phase mixture. More direct methods include photography, sampling probes, change of system volume during vapor generation, and separation of phases with measurement of the volume occupied by each phase. A report by Gouse [49] is probably the most comprehensive survey on void fraction measurement.

All of the above methods have certain disadvantages, but three of them were chosen for use in the present investigation in hopes that the combination of them would spotlight reasons for discrepancies and shore up confidence in void fraction measurements.

B.1 Trap Measurement

The simplest in concept of the methods is probably the last in the above list. This separation and measurement in the present case were accomplished by means of a "trap" — consisting of a vertical calibrated glass sight section through which the two-phase mixture passed and two quick-closing valves, one at either end of the glass section. A bypass with another quick-acting valve opened when the trap valves closed, allowing the main flow to travel around the trap. Figure 41 shows the device mounted on-line in the high flux loop.

The glass tube was an 18-in. length of precision-bore 1/2-in. inside diameter Pyrex. It was joined at each end to the machined flange of a Jenkins ball valve bored for a matching inside diameter and secured by Eccobond 276 cement. The closing mechanism consisted of a four-bar linkage connecting the valve actions to a steel 50-lb pull coil spring which was held in the cocked position by means of a trip latch. When tripped, the system closed the two sight section valves and opened the bypass valve in less than 0.1 sec. This isolated a section of the two-phase flow, allowing the liquid to drain to the bottom of the sight section, leaving the gas (or "void") at the top. Void fraction was read directly from the gas-liquid meniscus on a calibrated scale marked on the glass tube.

It should be recognized that the void fraction indicated in this method was not a point or local measurement. It was, in fact, a space-averaged quantity over the entire sight glass length, and was thus

sensitive to non-equilibrium effects (bubble collapse) leading to a variation of void fraction along the length. The relative importance of this effect varied with specific test conditions.

Another characteristic of measurement using the trap was the necessity of disrupting the main flow situation by directing the fluid through the bypass leg. Although such a procedure was somewhat inconvenient, the excellent reproducibility encountered in shakedown runs indicated that original conditions were easily established once the trap valves were reopened.

B.2 Photographic Measurement

Although photographic measurement is potentially the most accurate of the methods, it is, for many cases, too complicated and tedious to be practical. The setup described in the section on the low flux equipment was meant to provide data only for the special case of stable, low velocity, stratified-slug flow in the horizontal orientation.

For the relatively small void fractions (0.00 - 0.30) encountered under these conditions, it was possible to get good estimates of the volume of bubbles (or "voids") relative to that of liquid by means of a combination of photographs. Bubbles were so regular and similar as to allow volume estimates to be made on the basis of top and side views in most such instances. To insure adequate sampling, many randomly-timed pictures were taken of each flow situation once steady state was established. The picture results were averaged over all pictures taken

for given conditions and analyzed for deviations. The reproducibility and accuracy obtained from this procedure was judged adequate for checking the capacitance meter system in this very limited range of conditions.

B.3 Capacitance Measurement

One may note that the capacitance system is the only "indirect" method of the three outlined in this appendix. In principle, the instrument measured the capacitance (or dielectric constant) of the cylinder of fluid contained within the sensor element and converted this to a void fraction, based on the position of the measured capacitance on the scale ranging between the capacitance of the test liquid and that of its vapor.

Like the previous two methods, this one involved the length-averaged void fraction (over the 6-in. sensor length), but it did offer the conveniences of direct, on-line readout and monitoring of large-scale dynamic behavior. Unfortunately, other potential problems with capacitance measurement indicated the necessity of extreme care in applications.

Of prime concern was the fact that a combination of two capacitors, in general, have widely differing characteristics depending on whether they are connected (or sensed) in series or in parallel. The problem becomes obvious when the situation of two different flow regimes having the same void fraction is considered. Next, it is well known that the capacitance of a liquid may be affected by temperature and is, in

general, extremely sensitive to impurities. Finally, the electronic components within the sensor may be temperature-sensitive, may produce an undesired non-uniform field, or may be susceptible to end effects.

With such uncertainties, it was deemed necessary to undertake an extensive shakedown and verification study on the reliability of the capacitance system in measuring void fraction. The first step involved temperature calibration of the sensor for variations associated with both the liquid and gas phases.

Since the dielectric properties of air and Freon-113 vapor were equal within the accuracy of the instrument, it was deemed adequate to conduct the gas-phase portion of calibration with air in the precision furnace. It was found that sensor output increased in a linear fashion with working temperature within the range 70 - 160°F for air as the dielectric medium. The calibration procedure consisted of a preliminary heating of the furnace containing the sensor, a 12-hour wait for thermal equilibrium to ensue (as indicated by eight thermocouples located on the sensor body, within the sensor, and in the ambient gas), and data-taking during the very slow cooling of the system. A subsidiary finding during these tests was that temperature gradients within the sensor body produced slight variations in output from that encountered for uniform temperature — implying that the sensor should be well insulated when installed on-line. Specific results for the gas-phase temperature calibration are shown in Figure 42.

Temperature calibration for the liquid phase was carried out on both the low flux and high flux loops. It was found that sensor output decreased in a linear fashion with working temperature within the range 70 - 120°F for liquid Freon-113 as the dielectric medium. The calibration procedure consisted of circulating the liquid through the insulated sensor until steady state was attained (as indicated by loop instrumentation plus four thermocouples which monitored sensor and bulk temperatures) and taking data for each set of conditions in the desired range. An additional finding of these runs was that the level of output from the sensor would vary slightly from day to day (less than 4%), but that temperature dependence remained consistent. This behavior was attributed to the effects of trace impurities on the dielectric constant. Specific results for the liquid-phase temperature calibration are shown in Figure 43.

According to the manufacturer of the instrument, the above calibrations are sufficient to correct for temperature effects and are to be applied in the following manner:

$$\alpha = \frac{\varepsilon_{\ell}(T) - \varepsilon_{TP}}{\varepsilon_{\ell}(T) - \varepsilon_{g}(T)}$$

where α is the void fraction of the two-phase flow, ε_{TP} is the dielectric constant of the two-phase flow measured by the instrument, and $\varepsilon_{\ell}(T)$ and $\varepsilon_{g}(T)$ are the calibration dielectric constants for the pure liquid and pure gas phases, respectively, at the representative "bulk" temperature T.

Now, if the manufacturer's assertions are correct, what do they imply about the expected performance of the instrument for the case of equal void fractions with differing flow regimes? It is helpful to consider the simple situation of 0.50 void fraction with pure slug flow and with pure stratified flow between flat plates (see Figure 44). It is clear from this example that the two cases have the same void fraction but not the same capacitance (or effective dielectric constant). The slug flow situation is the one which results in an expression identical to that given above; thus, the value given by the manufacturer-recommended equation would appear to yield correct values for pure slug flow while failing for other flow regimes.

In fact, the boundaries within which data from all flow regimes must fall can be easily determined by extending the comparison of series and parallel arrangements (the extremes) begun above. The results are shown in Figure 45.

Having established the rationale for expecting the capacitance meter to be flow-regime sensitive, one finds the need for tests to verify such behavior and for additional calibration runs in the flow regimes of interest. The stratified-slug flow regime was investigated on the low flux loop with voids produced by heating of gassy Freon-113 liquid. An idealized prediction for void meter performance, easily derived from an extension of the series-parallel analyses, is shown in Figure 45. Measurements taken over the void fraction range 0.00 - 0.30 by the capacitance measuring system are compared in Figure 45 against those taken

by the photographic system associated with the low flux loop. The comparison shows that "actual" void fraction was fairly close to that indicated by the sensor (and manufacturer's equation) but that most readings were slightly on the high side, as expected.

The bubbly and bubbly-slug flow regimes of interest to experiments on the high flux loop were checked out next. For these runs the sensor was placed downstream of the trap section on the high flux loop, with the trap being used to determine the "actual" void fraction for comparison purposes. Methods used for producing voids were injecting air into the stagnant liquid column, injecting air into the flowing liquid, and flow boiling of gassy liquid. The results presented in Figure 45 indicate a significant departure of "measured" from "actual" void fraction over the range 0.00 - 0.40 for these two flow regimes. The data scattered consistently about the line shown, and this was the calibration line used for the reduction of data from the high flux loop.

It is appropriate to note here that three separate readout methods were employed in the use of the capacitance void meter. The electronics package allows for 0 - 5 volts output to a precision Digitec digital voltmeter, 0 - 5 millivolts output to a Sanborn recorder, and direct visual output from a meter with a calibrated face on the front of the component case. The digital readout was used for high accuracy in the single-phase calibration stages. The recorder readout was used for fast response and time-averaging in two-phase situations. The readout from the meter face was compared with the digital and recorder readouts and was

found to be adequate for both accuracy and time-averaging requirements. This latter purpose was fulfilled by an internal, adjustable damping system.

Appendix C

DISSOLVED GAS MEASUREMENT

The effects of dissolved gases are accentuated for the case of fluorocarbons due to their relatively large dissolved gas content under normal conditions (see Table C). It is important for the purpose of documenting these effects that an accurate measurement technique be employed to measure such content. Methods considered in preliminary studies included gas chromatography, mass spectroscopy, freeze distillation analysis, and electrolytic cell exposure. It was determined that none of the above methods provided the desired characteristics of on-line convenience and good measurement accuracy of all dissolved gases.

C.1 Aire-Ometer Checkout

In order to fulfill these requirements, it was decided to try the Seaton-Wilson AD-4002 Aire-Ometer (see Figure 46). In operation, the device takes in a measured amount of test liquid, depressurizes and films the sample on the walls of a glass manometer tube, then repressurizes the sample — collecting a measured volume of vapor and foreign gas (formerly dissolved) above the test liquid sample. Assuming

equilibrium between the vapor and liquid and total elimination of dissolved gas from the liquid at the end of this procedure, one can deduce the amount of dissolved gas originally contained in the sample from the final temperature, pressure, and gas volume. With this device, convenient samples can be analyzed quickly for all dissolved gases, without, however, determining the identity or proportions of such components.

First, it was necessary to validate the reliability of the device and the assumptions underlying its design. Early tests showed that usual vacuum greases (mainly silicones) provided inadequate sealing for the depressurization sequence. This behavior was due to incompatibilities noted earlier in the text and was successfully avoided later by use of glycerin-Bentonite, phosphate, and Apiezon vacuum greases. It was found that excellent reproducibility was achieved by allowing appropriate times for depressurization and repressurization sequences.

Only two standards were available for checking the device's measurements of dissolved gas content in Freon-113. One source was a coolant bulletin by DuPont [50], and the other was the test run by the meter's manufacturer [51] especially for this investigation. For the conditions of a total pressure of 14.70 psia and a temperature of 77°F, there was excellent agreement of the present Aire-Ometer data with both the standards. The comparison was within 5% and is illustrated by the points plotted in Figure 47. For purposes of clarity, it should be noted here that the gas content referred to above is that which exists in an equilibrium situation between air, Freon-113 vapor, and Freon-113 liquid. Thus nitrogen and oxygen are the predominant dissolved gases, but their

relative proportions in the dissolved state are not necessarily the same as that in the air. This relation is determined by their respective solubility constants, and DuPont data indicate a noticeable difference between them. However, it is convenient for present purposes to refer to the mixture of "dissolved" composition as "air."

C.2 Temperature Variation of the Solubility Constant

With the reliability of the instrument and the scarcity of relevant data well established, the next step was to get a qualitative and quantitative feel for the dissolution situation with air in Freon-113. Early tests showed that the associated diffusion and convection processes could range from very rapid — the order of several minutes to degas an open beaker of Freon-113 by vigorous boiling — to very slow — the order of many hours to redissolve air into a sample in a stagnant situation.

Finally, it was desired to accurately establish the temperature variation of the solubility constant for air in Freon-113. For this purpose, a 1-liter glass bottle with a narrow, open neck and a low sampling port was half-filled with liquid Freon-113 and immersed in a constant temperature bath. Compressed air was bubbled through the Freon-113 until near-equilibrium conditions were established. Then the compressed air feed was stopped to allow time for temperature equilibrium to be attained as indicated by four monitoring thermocouple systems. Samples were then taken through a hose running from the port to the

Aire-Ometer and analyzed as explained before. Data taken over a large temperature range are given in Figure 47.

The major conclusion to be drawn from the data is that the solubility constant for air in Freon-113 does not vary significantly with temperature. The fact that this constant increases slightly with temperature does not imply that the amount of dissolved gas increases with temperature. In fact, the amount actually decreases with temperature, as is indicated indirectly by the relatively large amount of scatter for data taken at high temperatures (uncertainty in the value of the solubility constant increases with a decrease in the amount of air measured).

Appendix D

OPERATING PROCEDURES

D.1 Preliminary Procedure

Diabatic data-taking sequences on the high flux loop were preceded by the lengthy checkout procedure outlined below.

1) Charge loop and reservoir with supply of Freon-113
2) Conduct preliminary check of the various data read-out systems
3) Turn on water cooling to the heat exchanger, power leads, reservoir condenser, and emergency generator power link
4) Adjust loop valves and turn on system pump
5) Readjust valves as necessary and wait for steady state at the desired conditions
6) Determine base dielectric constant at the given bulk temperature for use in reduction of capacitance void meter readings
7) Check for direct correspondence among readings from various wall and bulk thermocouples
8) Vent the central pressure tap manifold in order to eliminate air bubbles and fill the manometer and pressure tap lines
9) Compare measured pressure drop with that predicted by the standard Nikuradse correlation for tubes from measured flow rate and bulk temperature
10) Change the flow rate and repeat 9) above
11) Start up and balance the two DC generators
12) Power up the heated length to a low flux

13) Power up the three guard heater segments so as to match each inside guard wall temperature with each corresponding outside test wall temperature

14) Wait for steady state to be achieved

15) Use heat balance to compare measured electrical power into test section with measured rate of increase in energy of the flowing medium (This allows a comprehensive check of measurements of voltage, current, flow rate, and inlet and exit bulk temperatures, as well as the adequacy of the guard heater and insulation provisions)

16) Compare resulting heat transfer rate with that predicted by the standard McAdams correlation (This allows a second comprehensive check of the measurements mentioned immediately above, as well as a test of the accuracy of test wall temperatures)

17) Change the heat flux and repeat 13) through 16) above

18) If all previous indications are favorable, set the desired pressure level and flow rate by means of the various loop valves

19) Undertake an adequate degassing procedure (employing the reservoir heaters and return bleed flow valve) until the desired dissolved gas content is attained as indicated by Aire-Ometer measurements

20) Adjust heated length power to the desired initial level

21) Adjust cooling water flow to the heat exchanger so as to achieve the desired test section inlet temperature

22) Adjust guard heater power to match wall temperatures as before

23) Wait for steady state to be achieved — making small loop adjustments as necessary to obtain desired operating conditions

D.2 Data-Taking Procedure

After the preliminary procedure, the data-taking sequence generally

began with very small increases in heat flux (order of 3% steps each) while maintaining the single-phase regime. After incipience, heat flux increases were coarser (order of 10% steps each).

The increasing heat flux traverses were terminated when (a) observations indicated that critical heat flux was near or (b) correlation predictions indicated such a situation existed. Decreasing traverses proceeded from the maximum heat flux to single-phase values using the same intermediate levels as those of the increasing traverse.

A period of about 15 minutes was allowed between each setting of heat flux for steady-state to ensue. Appropriate readjustments to maintain required pressure level, inlet temperature, flow rate, and dissolved gas content were made before data-taking commenced.

No stainless steel tube which had previously "burned-out" was used for data-taking purposes.

Appendix E

DATA REDUCTION

The experimental data obtained in the present investigation were reduced by a master program and subroutines written in Fortran IV and run on the I.B.M. 1130 computer of the M.I.T. Mechanical Engineering Department.

Freon-113 properties were provided by curve fits to values given in the coolant manufacturer's bulletins [52, 53]. Many of these curves were taken from subroutines listed in Reference [12].

Mass velocity was derived from flow meter readings, with correction for density variations as specified in Reference [54]. Heat flux was calculated from measured test section voltage and current and was based on the inside diameter of the tubes. Pressure drop was determined from manometer readings, with correction for density variations in the liquid columns. Void fraction data from the capacitance measuring system was reduced according to the methods given in Appendix B and Chapter 6. Dissolved gas content was deduced from gas volume measurements made by the Aire-Ometer, with appropriate correction for variation in ambient conditions (see Appendix C).

Wall and bulk thermocouple outputs read through the K-2 potentiometer were converted to temperatures according to a curve fit by

Hynek [55] to the Leeds and Northrup table [56] for copper-constantan thermocouples. Measured outside wall temperatures were modified to give inside wall temperatures by accounting for gradients within the tube wall due to internal heat generation. Since the wall was quite thin, the modifications were in all cases less than 2°F.

Various subroutines were developed to aid in checking measurement accuracy and to aid in the presentation of data in correlated form. Heat flux values previously mentioned were checked by comparison with an inlet-exit bulk heat balance for single-phase flow. As mentioned in Appendix D, single-phase heat transfer and pressure drop data were compared with the McAdams and Nikuradse correlations. The Gambill correlation for critical heat flux (see Chapter 3), the gassy saturation temperature analysis (see Chapter 4), the Staub prediction for net generation (see Chapter 6 and Appendix F), and the Bergles-Dormer correlation for boiling pressure drop (see Chapter 6) were also programmed as subroutines.

Appendix F

STAUB'S MODEL FOR THE POINT OF NET VAPOR GENERATION

From a force balance on a departing bubble which marks the point of net vapor generation, Staub [3] derives the following equation relating drag, buoyancy, and surface tension terms:

$$\frac{(\rho_\ell - \rho_g)\, g}{12\sigma\, f(\beta)\, g_c}\, D_d^2 + \frac{f_D \rho_\ell\, V^2}{32 g_c \sigma\, f(\beta)}\, D_d - 1 = 0$$

where

$$f_D = f_D\left(Re, \frac{D_d}{D}\right)$$

and from Schlicting [57]

$$\frac{1}{f_D^{0.50}} = 1.74 - 2.00 \log_{10}\left[\frac{D_d}{D} + \frac{18.7}{Re\, f_D^{0.50}}\right]$$

for turbulent flow. Given the experimental conditions and an appropriate $f(\beta)$, one can solve the above equations by iteration to yield an appropriate departure diameter D_d. By specifying the temperature at a distance $\frac{D_d}{2}$ from the wall at $T = T_{sat}$ and using the universal temperature profile (see Reference [3]), one can solve for the local

bulk subcooling at this point of net vapor generation. For the present cases, D_d was relatively large and protruded into the turbulent core so that the appropriate relation is

$$T_{sat} - T_b = \frac{7.07\ q/A}{c_\ell \rho_\ell V f_D^{0.50}} \left[\frac{\ln Y_c/Y_d}{1-Y_d/Y_c} - 1 \right] \left[1 - \frac{Y_d}{Y_c} \right]$$

It is suggested that the above equation be modified by changing T_{sat} to T_{satg} to account for dissolved gas effects. Of the range specified by Staub for $f(\beta)$, it was found that the highest value,

$$f(\beta) = 0.17$$

gave best results for the present situation. These specifications were used in calculating the predictions plotted in Figures 29-31.

Table A

COMPARATIVE PROPERTIES OF FREON-113 AND WATER

Property	Freon-113	Water	Unit
p_g	6.90	0.507	psia
ρ_ℓ	97.4	62.2	lb_m/ft^3
ρ_g	2.28×10^{-1}	1.58×10^{-3}	lb_m/ft^3
k_ℓ	0.0500	0.352	Btu/hr ft°F
μ_ℓ	1.62	2.10	lb_m/hr ft
c_ℓ	0.215	1.00	Btu/lb_m°F
h_{fg}	65.9	1050	Btu/lb_m
σ	1.26×10^{-3}	4.90×10^{-3}	lb_f/ft
K_{air}	1.38×10^{-4}	1.03×10^{-6}	moles/mole psi

Above values for temperature = 80°F

Table B

COMPARATIVE CRITICAL HEAT FLUX DATA AND PREDICTIONS

pressure (psia)	velocity (ft/sec)	inlet subcooling (°F)	dissolved gas (moles/mole)	actual C.H.F. ($Btu/hr\ ft^2$)	predicted range C.H.F. ($Btu/hr\ ft^2$)
22.3	2.13	61	10.80×10^{-4}	99,200	93,700-111,300
22.3	2.13	61	1.00×10^{-4}	82,800	93,700-111,300
22.3	2.13	61	1.00×10^{-4}	77,800	93,700-111,300
19.5	2.06	63	1.00×10^{-4}	83,400	92,300-108,900
19.0	2.06	62	1.00×10^{-4}	91,600	90,700-107,100
18.8	2.06	61	1.00×10^{-4}	83,700	90,300-106,400
18.8	2.06	61	1.00×10^{-4}	74,700	90,300-106,400
18.5	2.09	60	1.00×10^{-4}	78,400	89,900-106,000
18.4	2.09	60	12.10×10^{-4}	72,800	89,700-105,800
21.9	2.11	54	9.50×10^{-4}	75,300	88,300-104,700
22.2	2.14	52	8.92×10^{-4}	89,500	87,800-104,300
19.6	1.06	63	1.00×10^{-4}	54,700	63,900-72,600

Table C

COMPARATIVE DISSOLVED GAS UNITS

User	Unit	Air in Freon-113	Air in Water
Ricque	parts/billion (wt)	167,000	23,600
Beckman	parts/billion (wt)	167	23.6
3M	grams/1000 grams	0.167	0.0236
DuPont	moles/mole	0.00108	0.0000146
McAdams	milliliters/liter	224	20.0
Seaton-Wilson	milliliters/milliliter	0.224	0.0200

Conditions for the above: saturation, equilibrium at

total pressure = 14.70 psia

temperature = 80°F

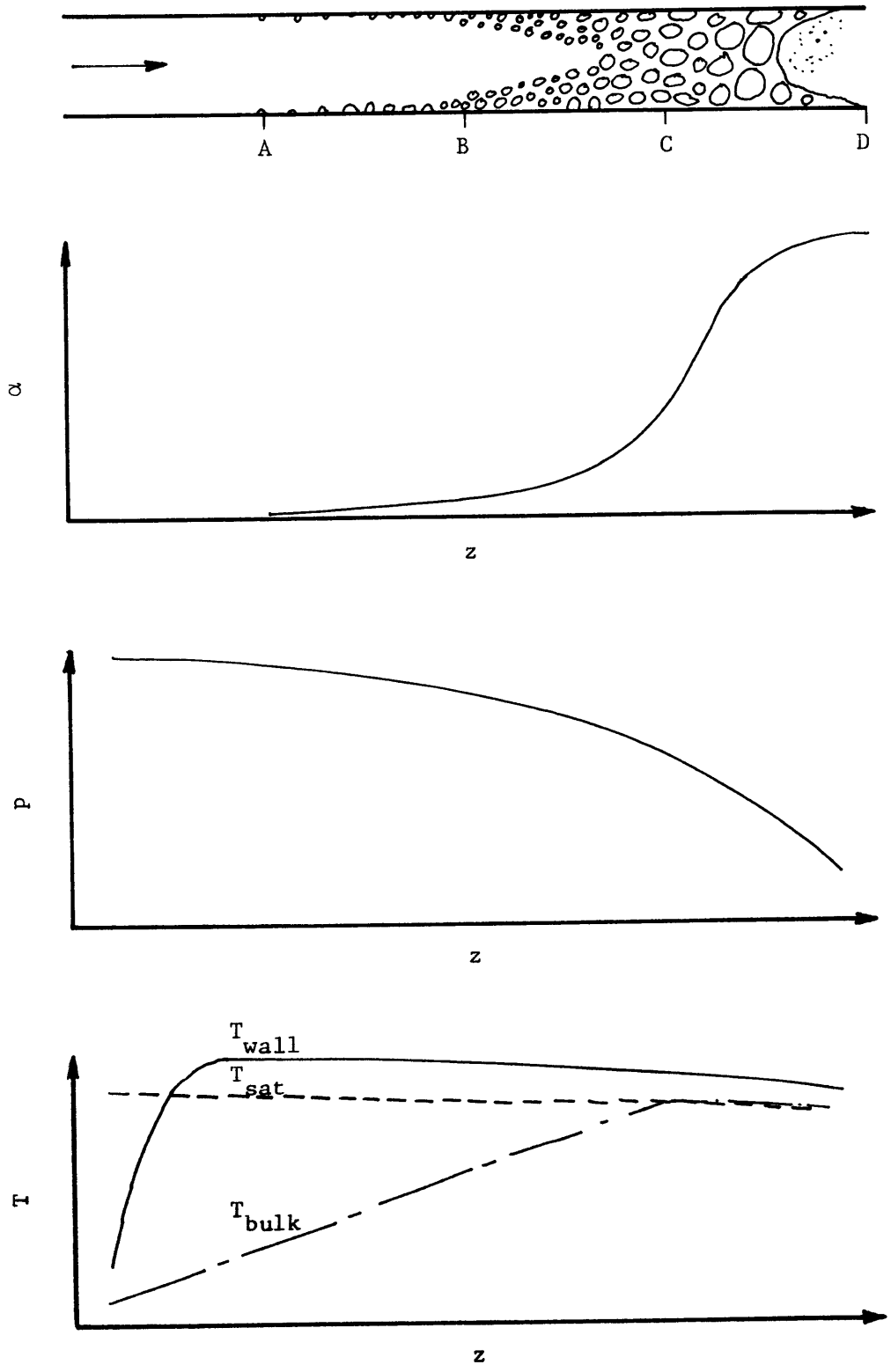

Figure 1. Composite View of Flow Boiling Situation

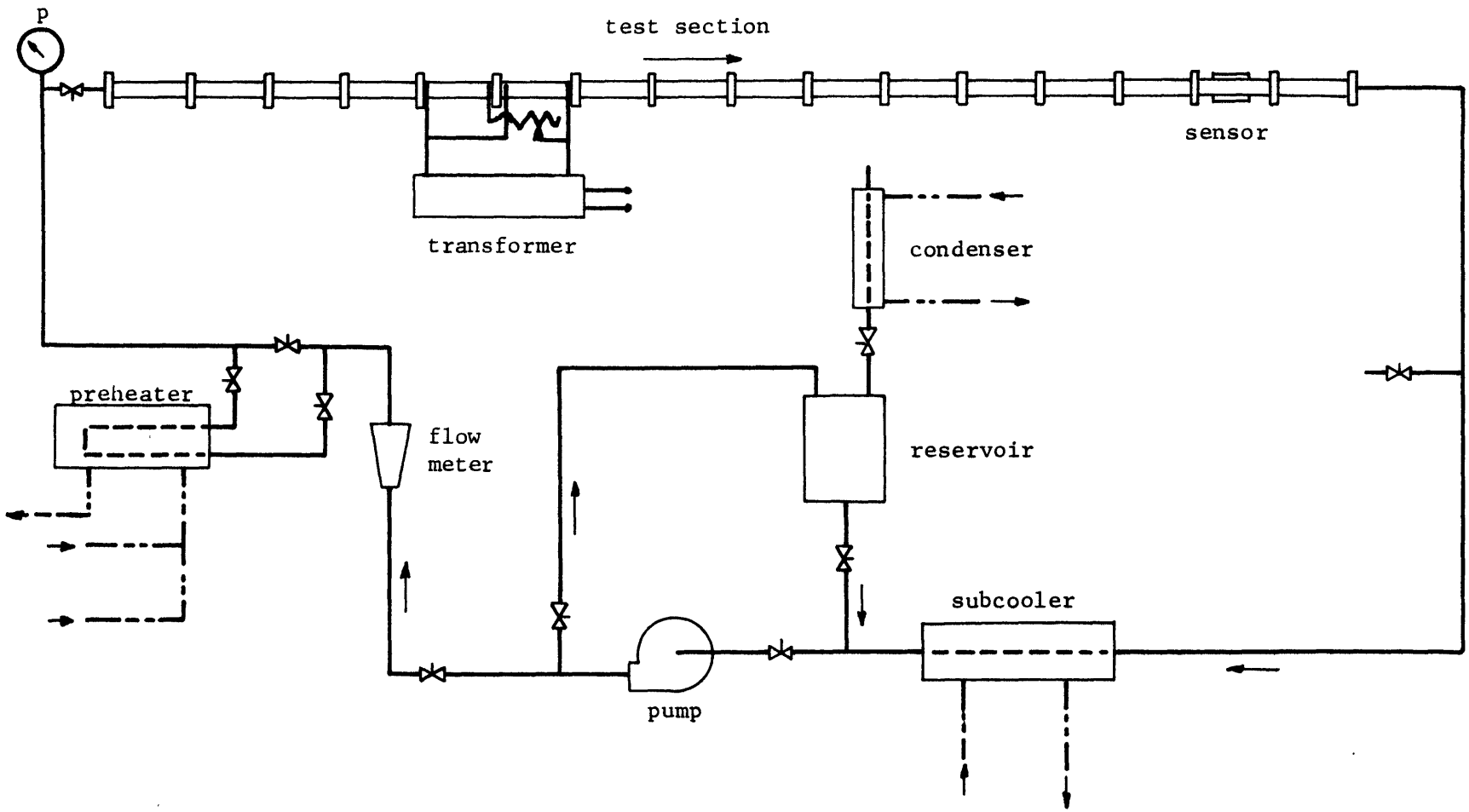

Figure 2. Schematic of Low Flux Loop

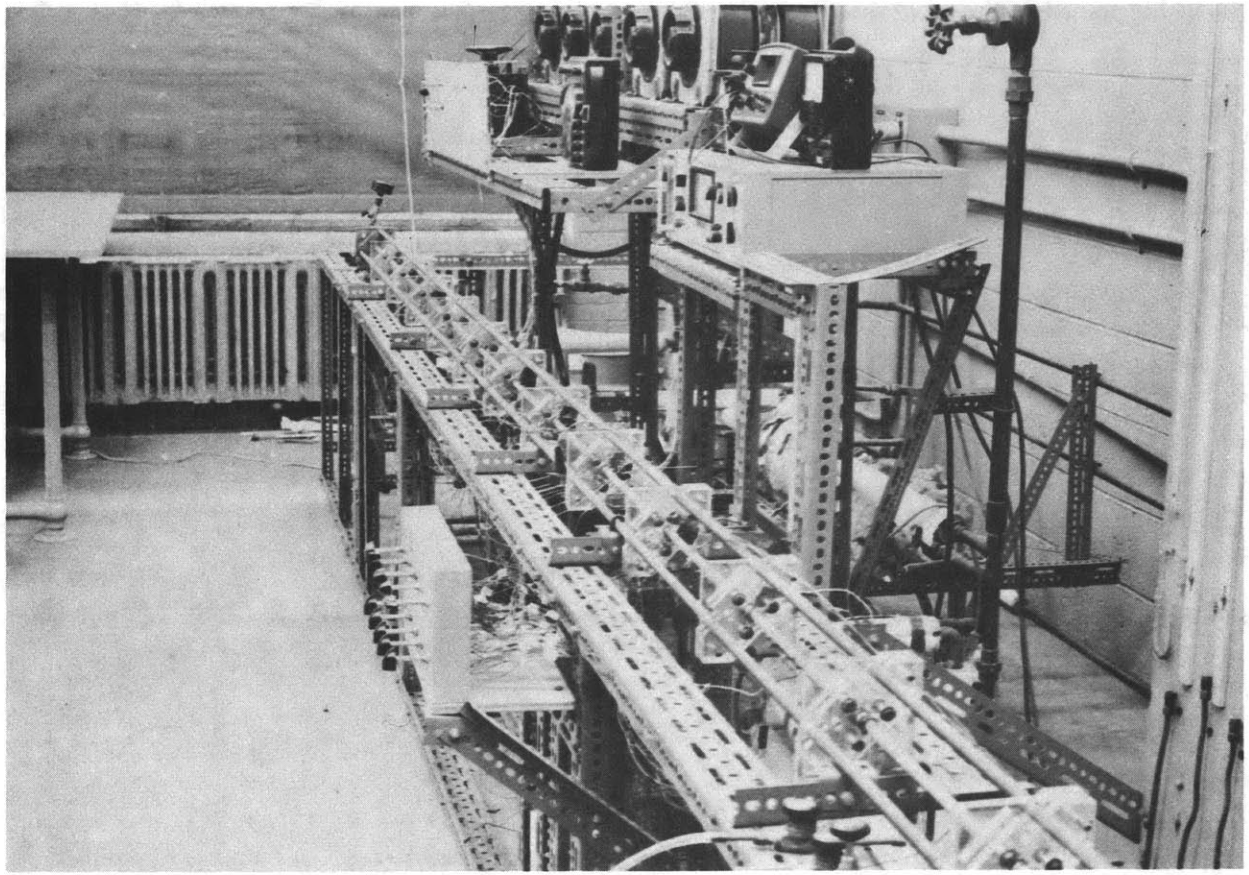

Figure 3. Photograph of Low Flux Loop

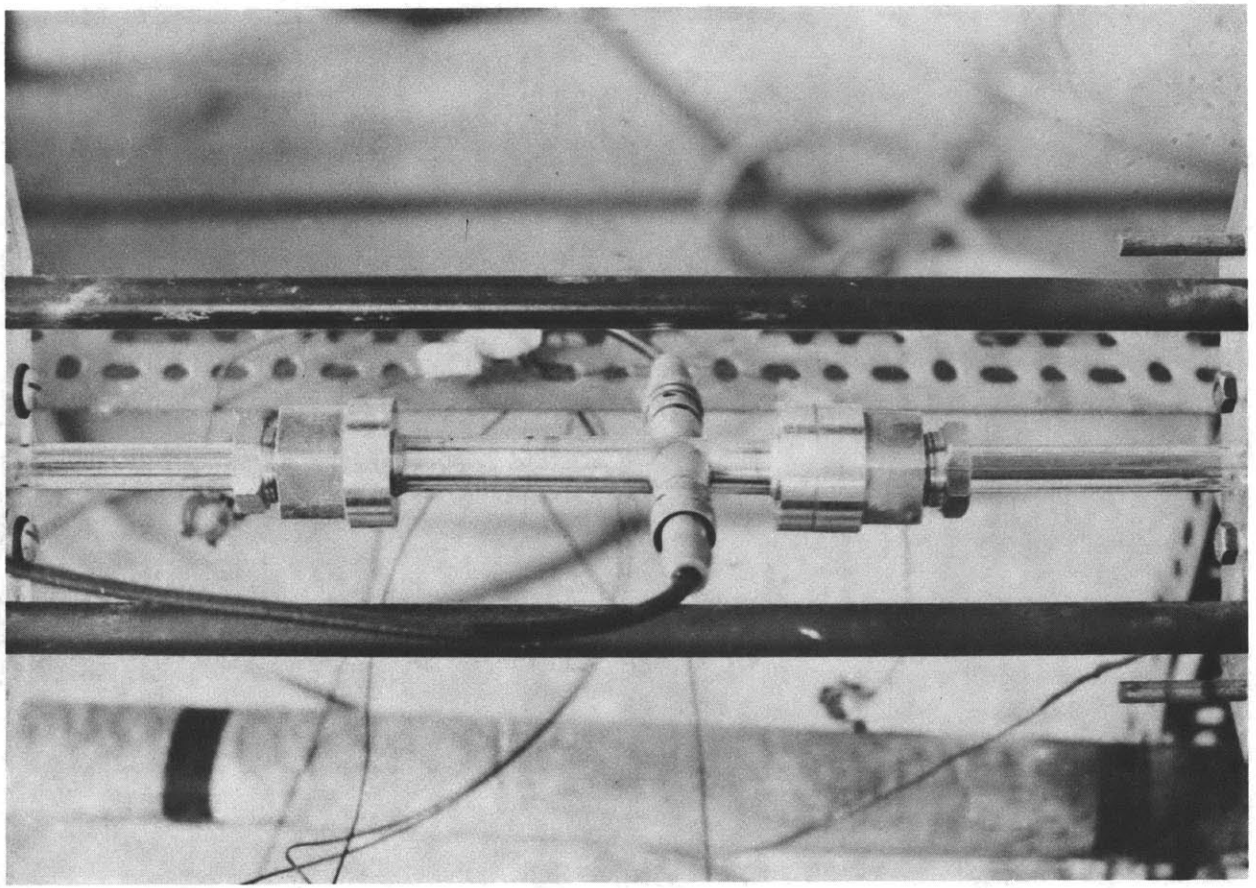

Figure 4. Capacitance Void Sensor Mounted in Low Flux Test Section

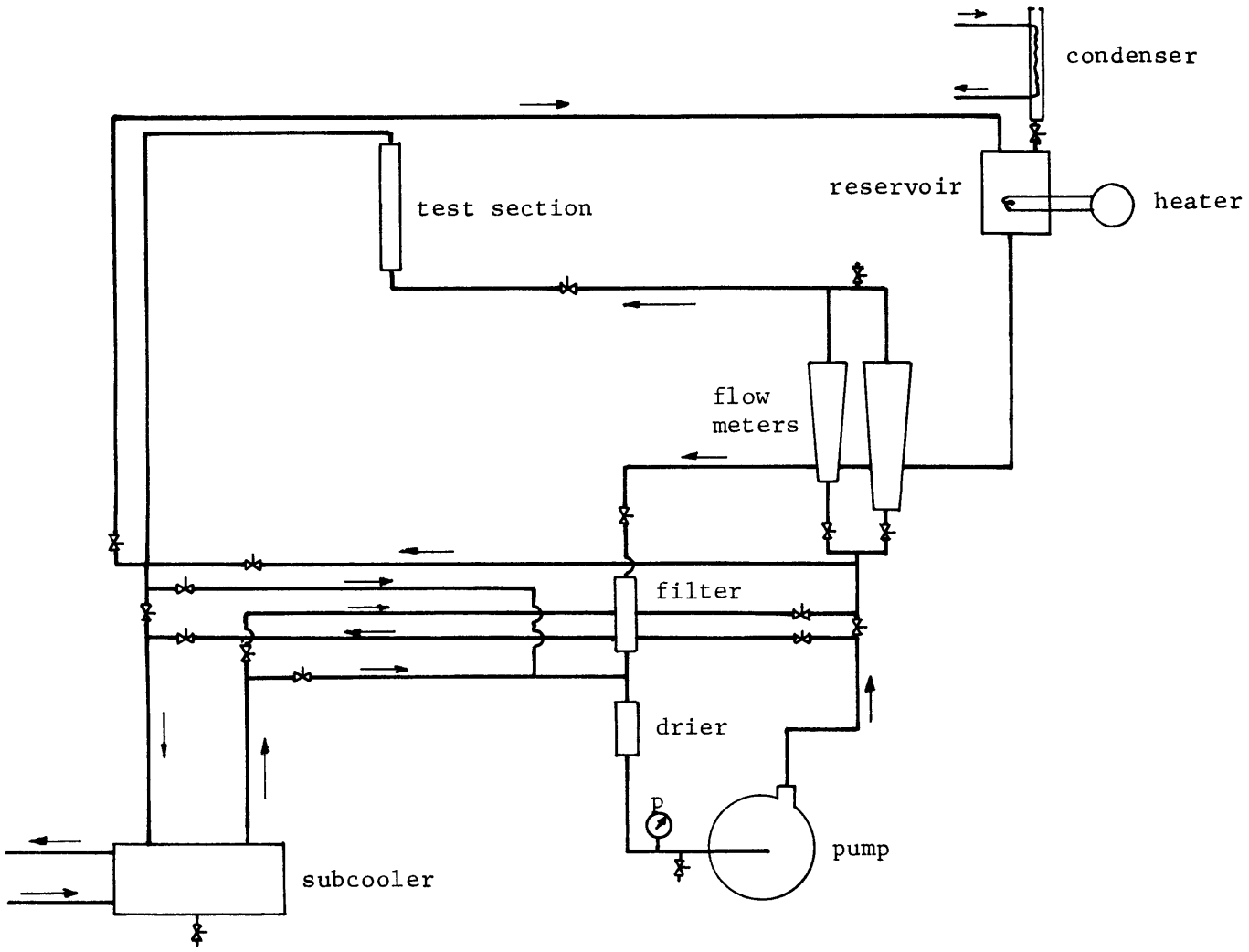

Figure 5. Schematic of High Flux Loop

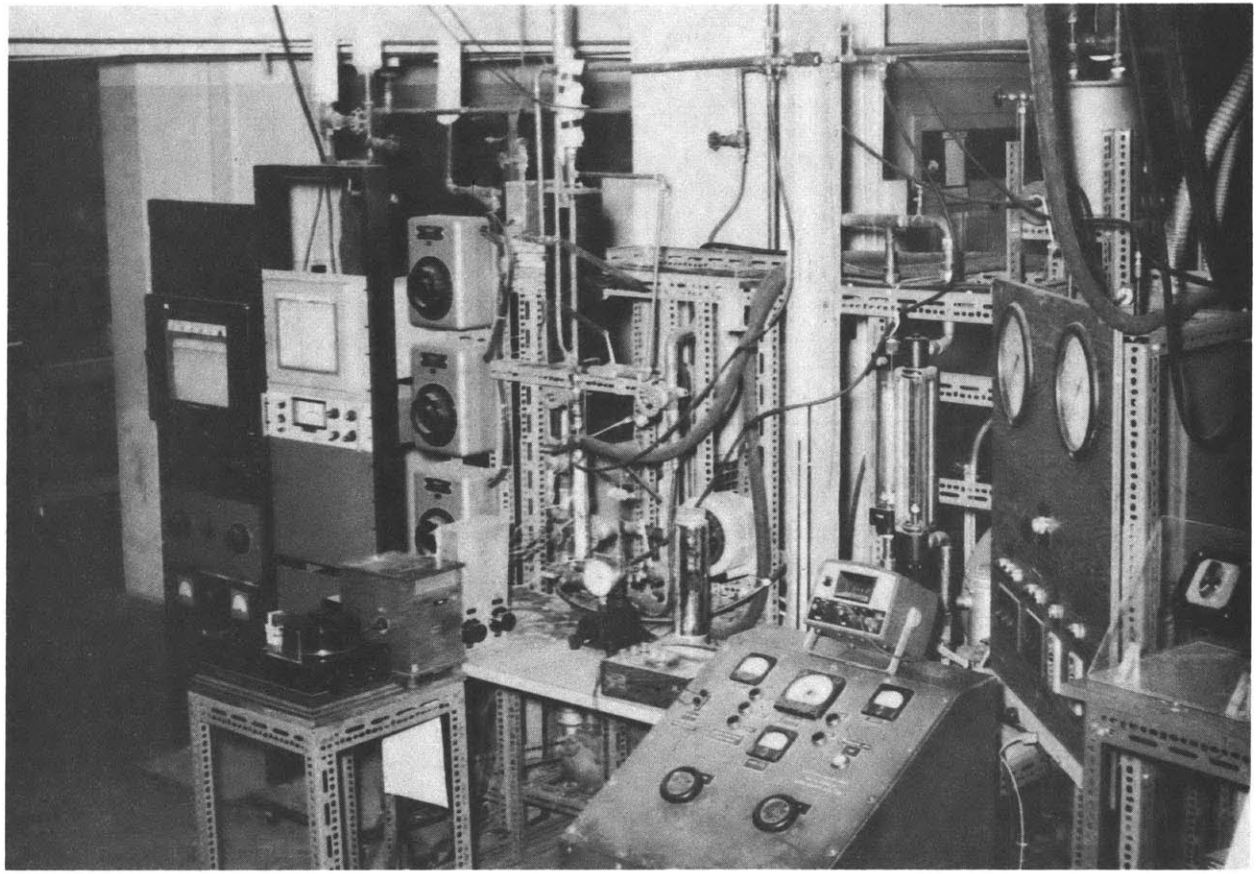

Figure 6. Photograph of High Flux Loop

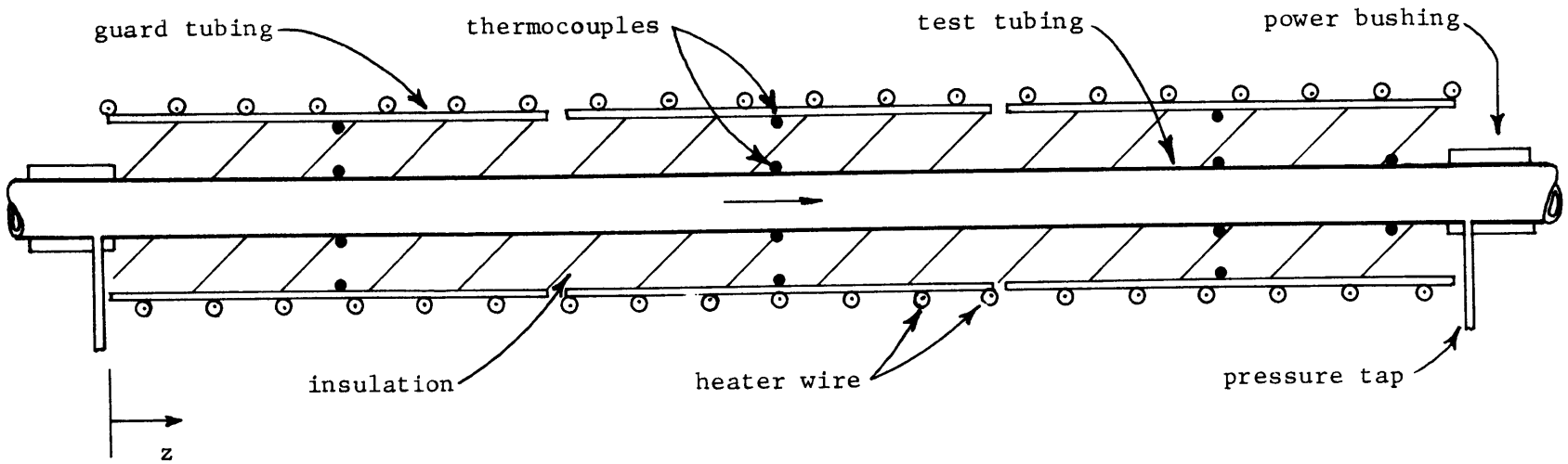

Figure 7. Detail of Heated Length in High Flux Test Section

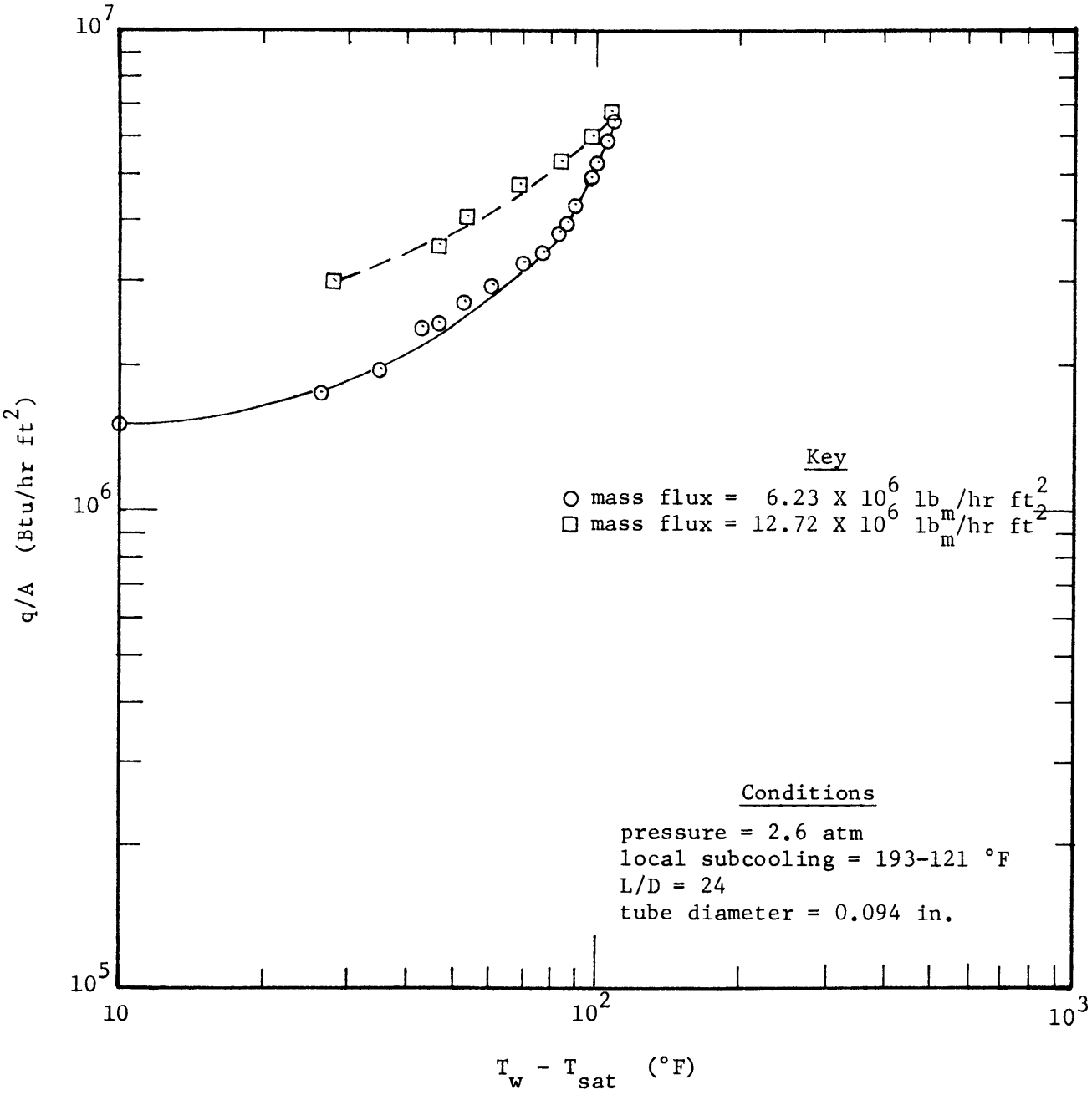

Figure 8. Water-Stainless Steel Flow Boiling Curve

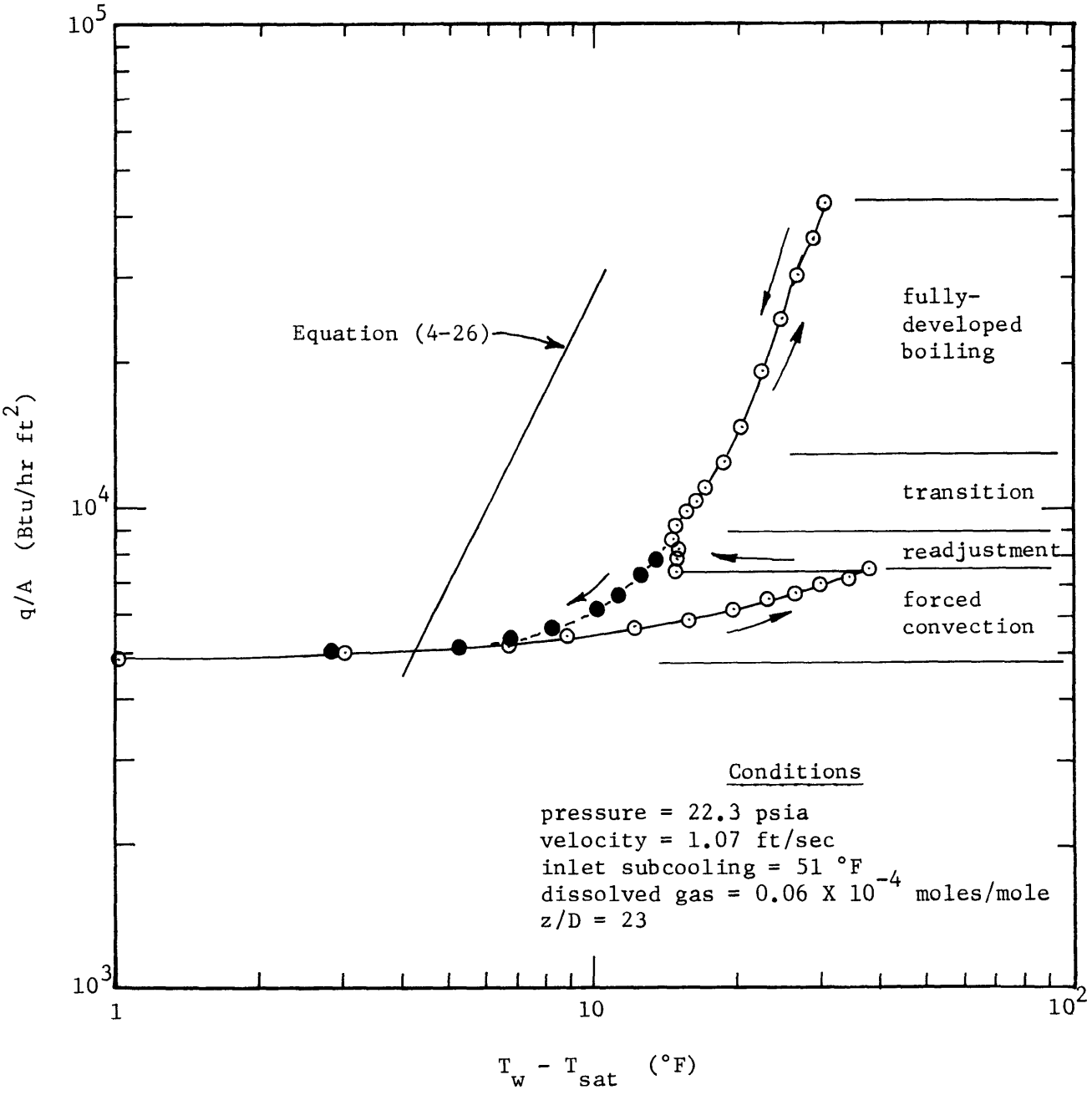

Figure 9. Freon-113-Stainless Steel Flow Boiling Curve

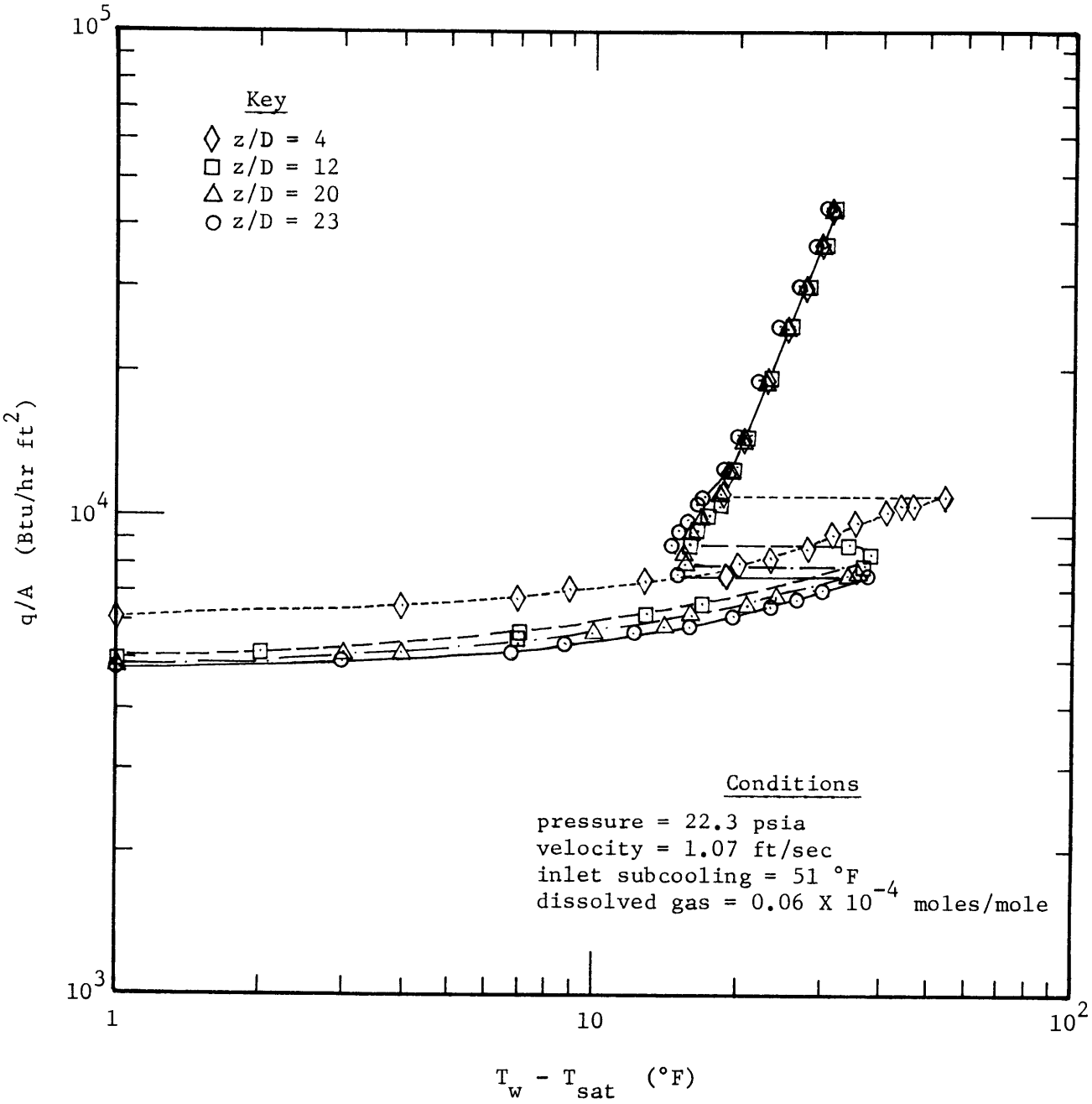

Figure 10. Composite Flow Boiling Curve

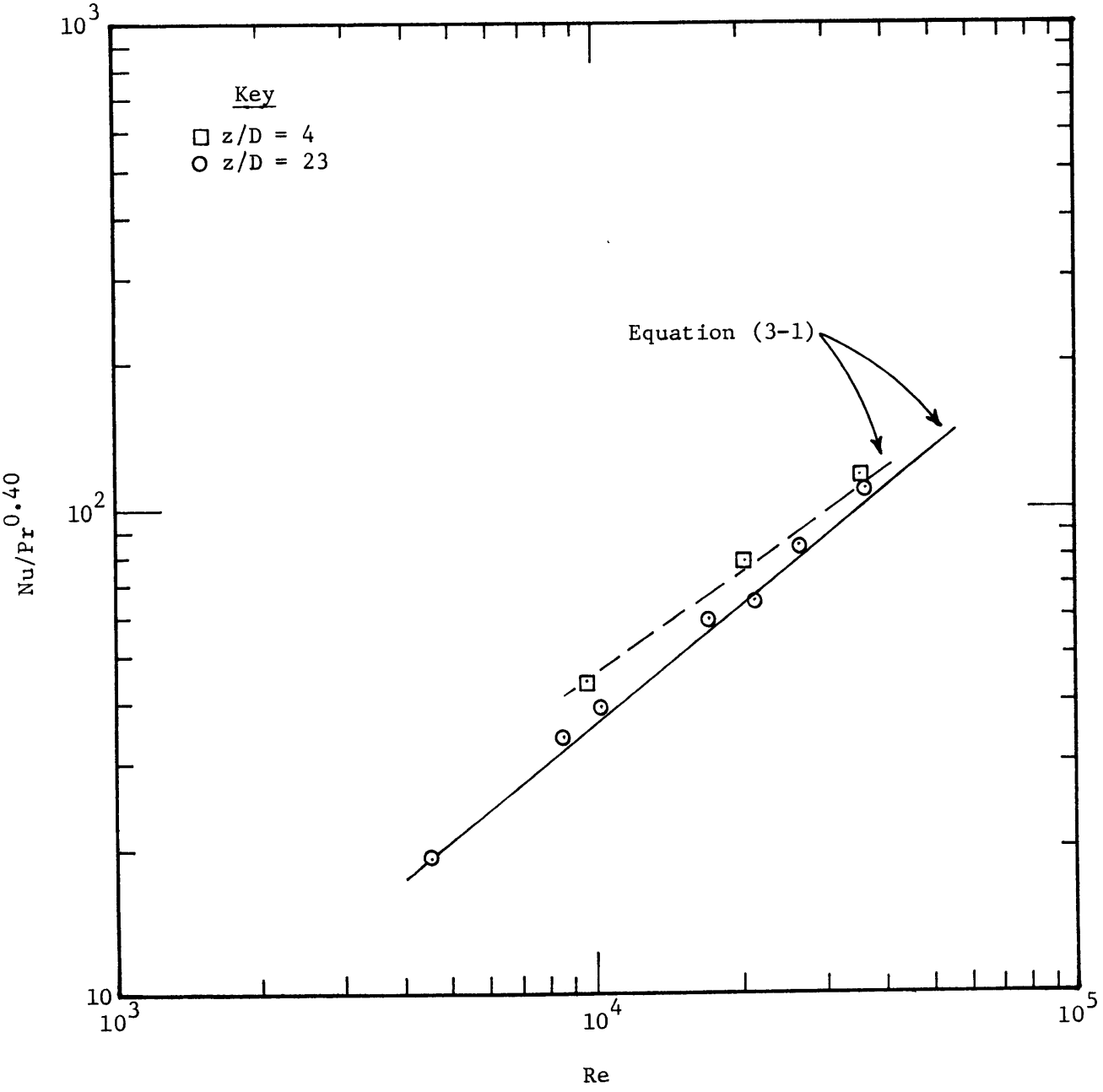

Figure 11. Single-Phase Heat Transfer Results

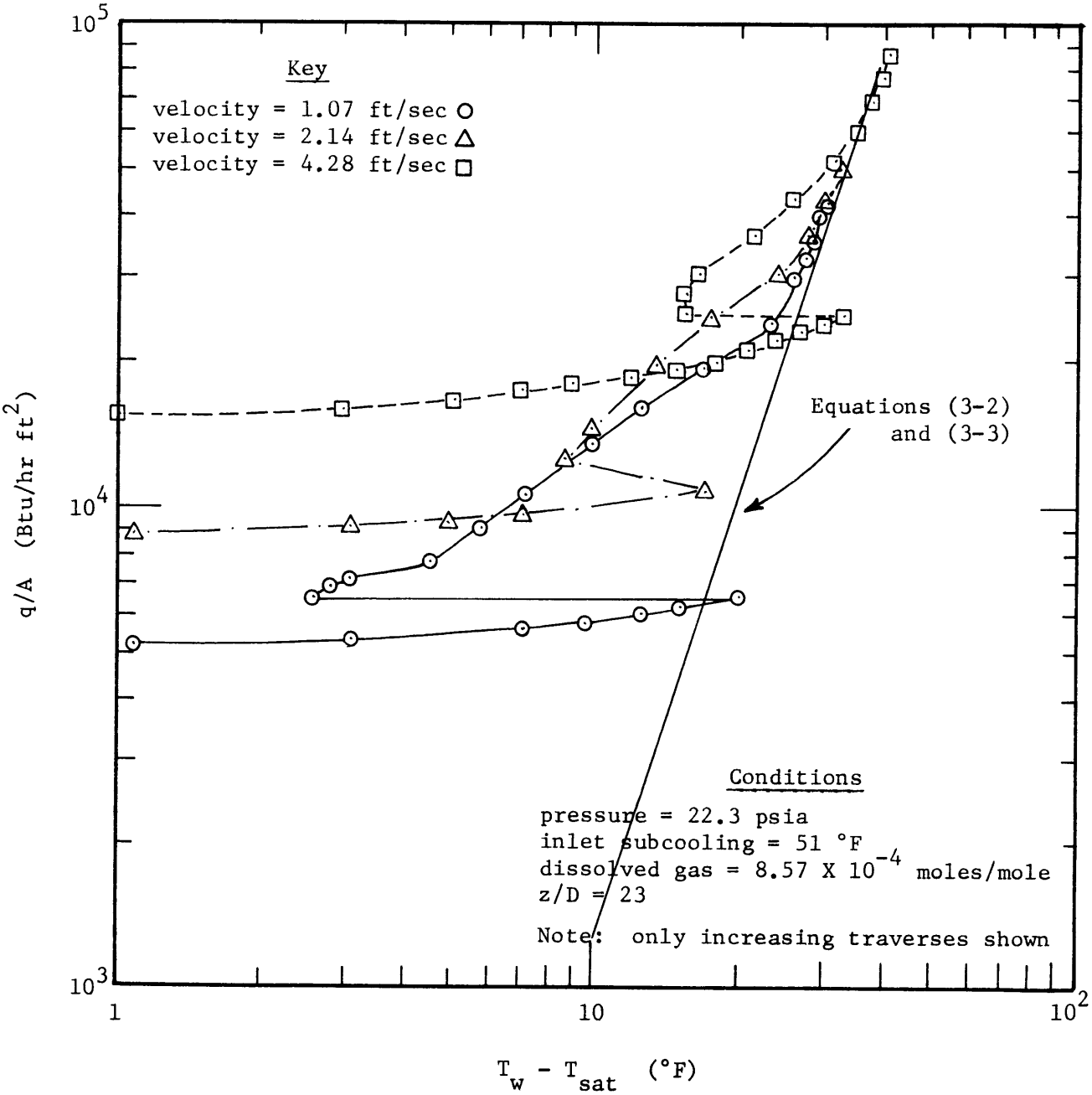

Figure 12. Mass Velocity Effects on Flow Boiling Curve

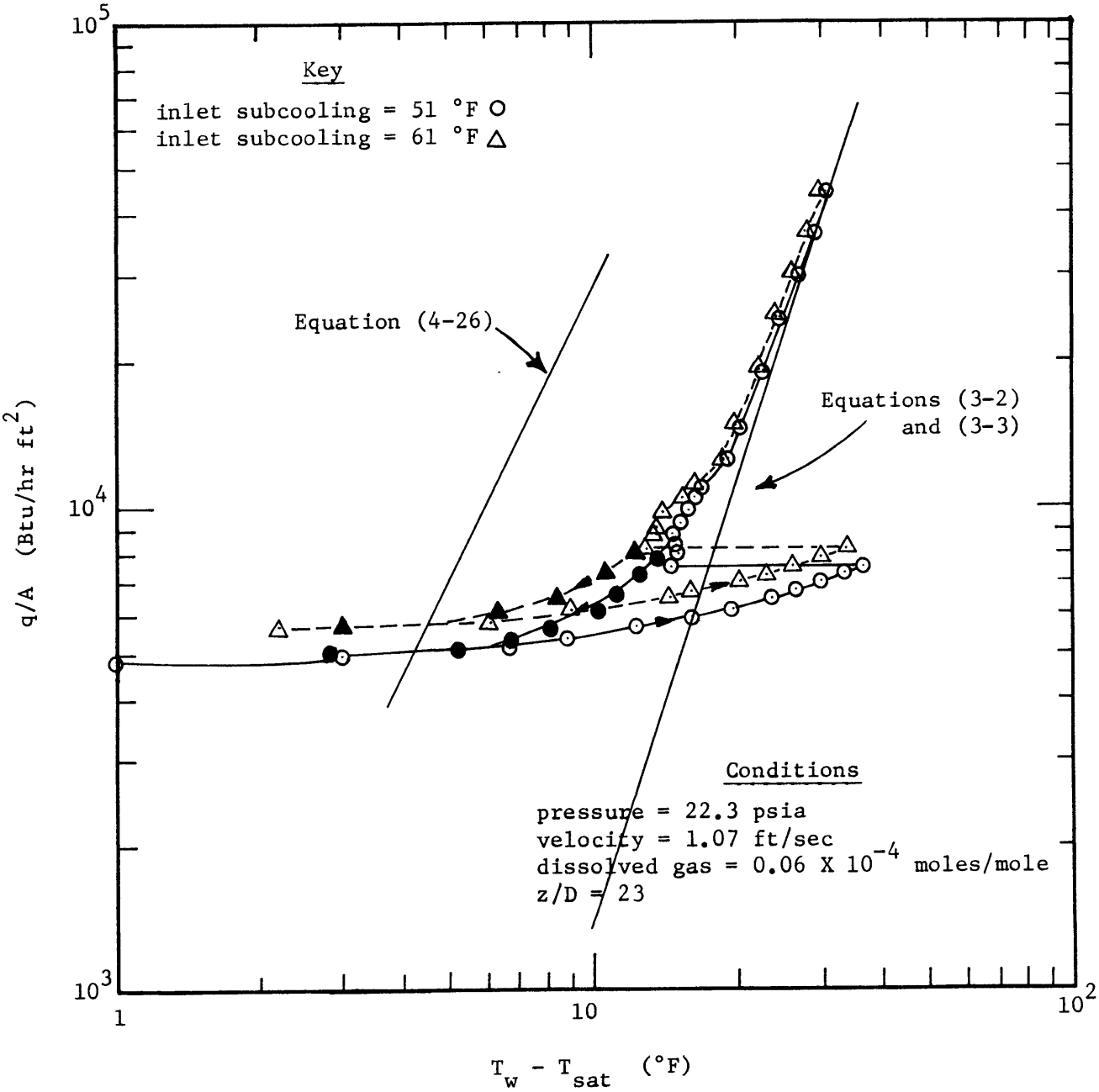

Figure 13. Inlet Subcooling Effects on Flow Boiling Curve

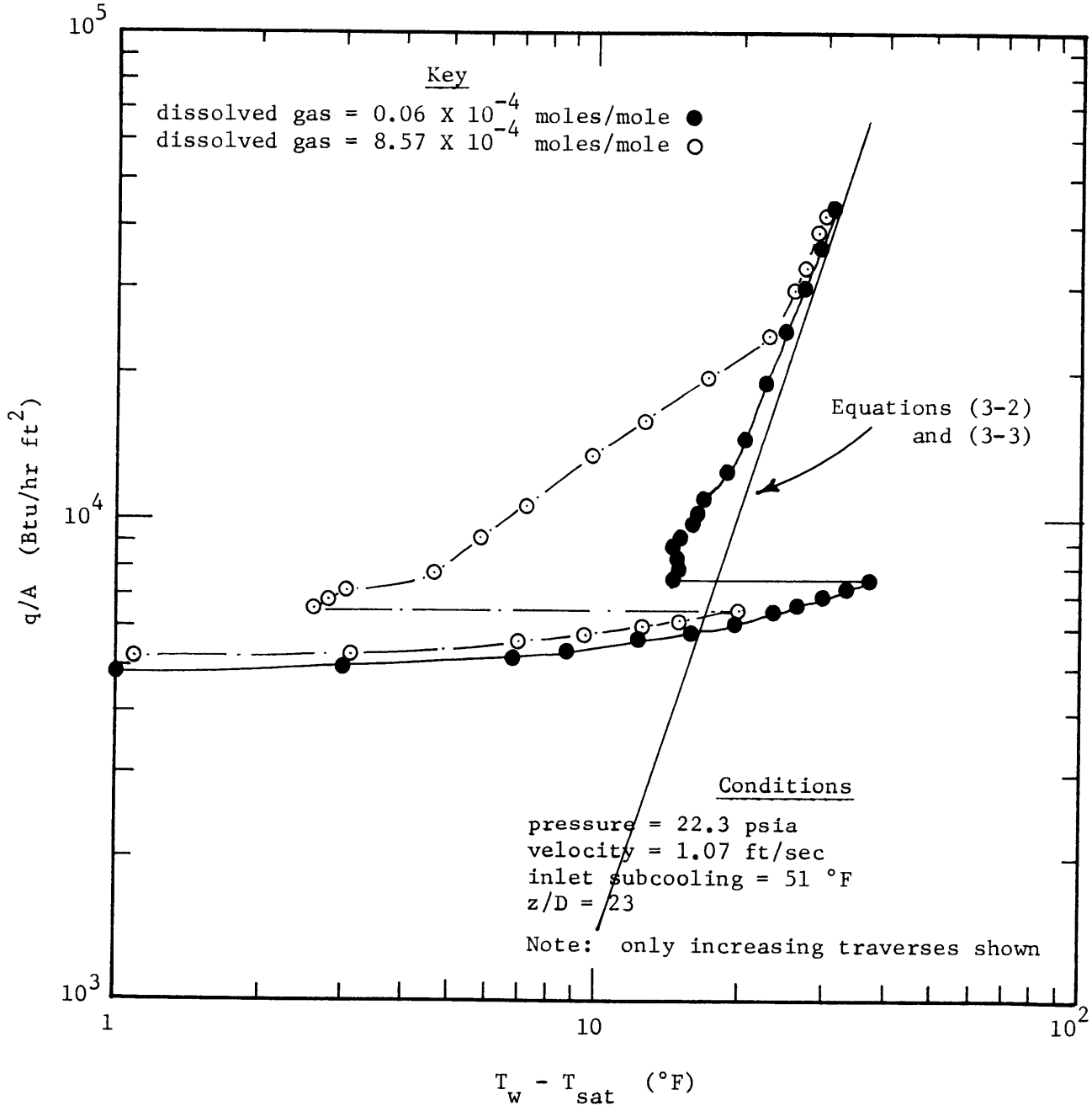

Figure 14. Dissolved Gas Effects on Flow Boiling Curve

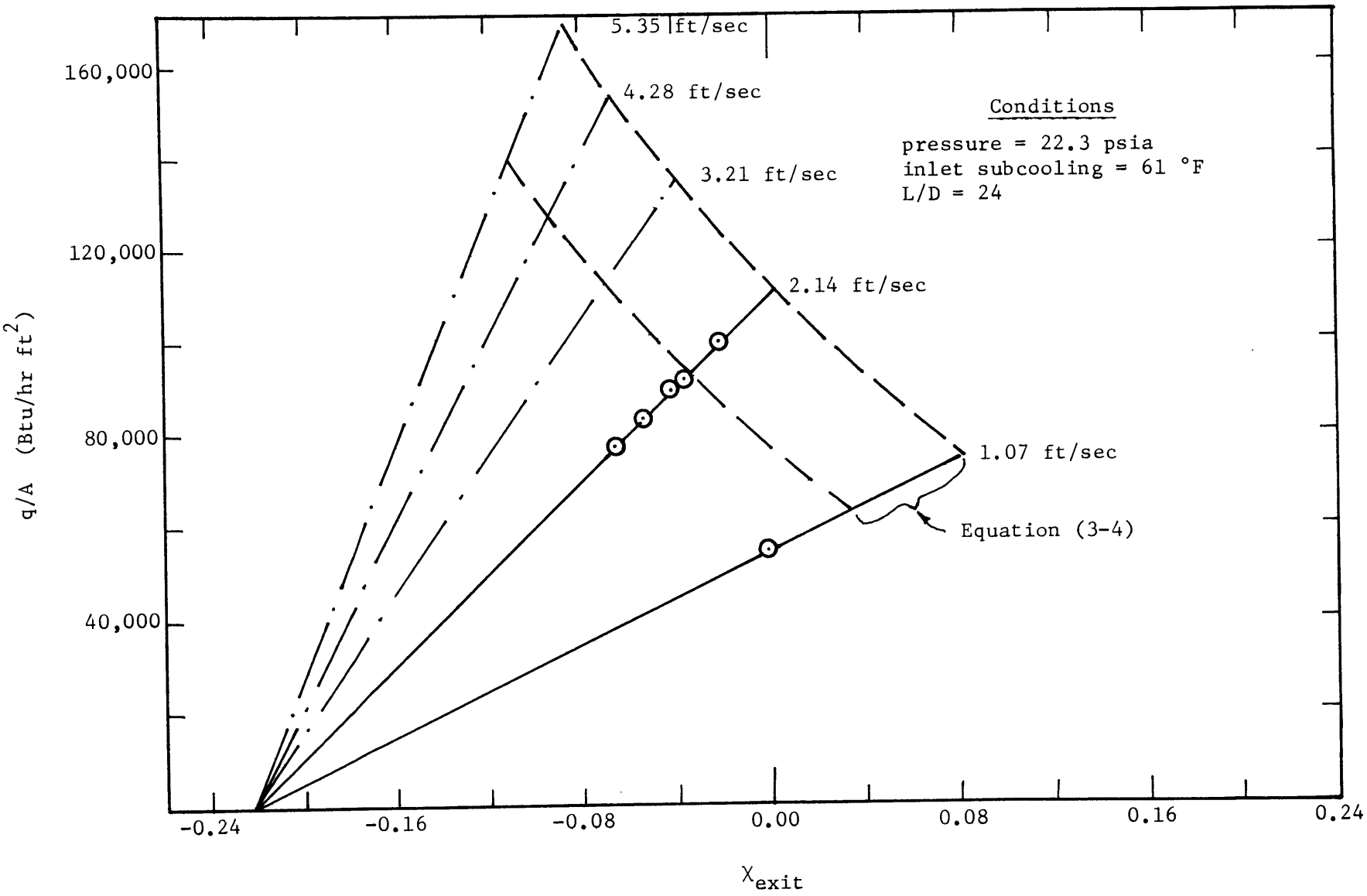

Figure 15. Critical Heat Flux Using Operating Curves

System A

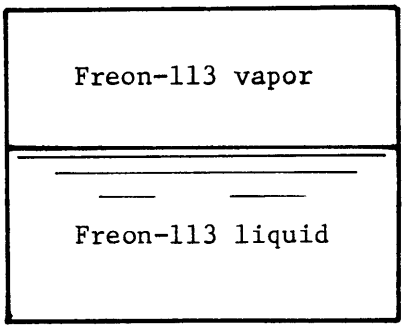

p_{total} = 14.70 psia

T_{sat} = 118 °F

System B

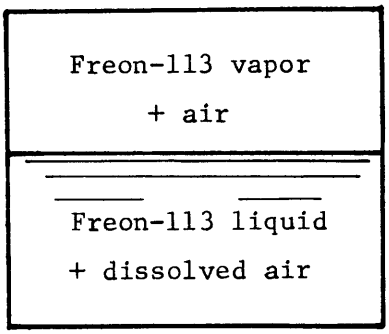

p_{total} = 14.70 psia

X_{air} = 10.80 X 10^{-4} moles/mole

T_{satg} = 80 °F

Figure 16. Comparison of Idealized Gassy and Degassed Systems Under Thermodynamic Equilibrium Conditions

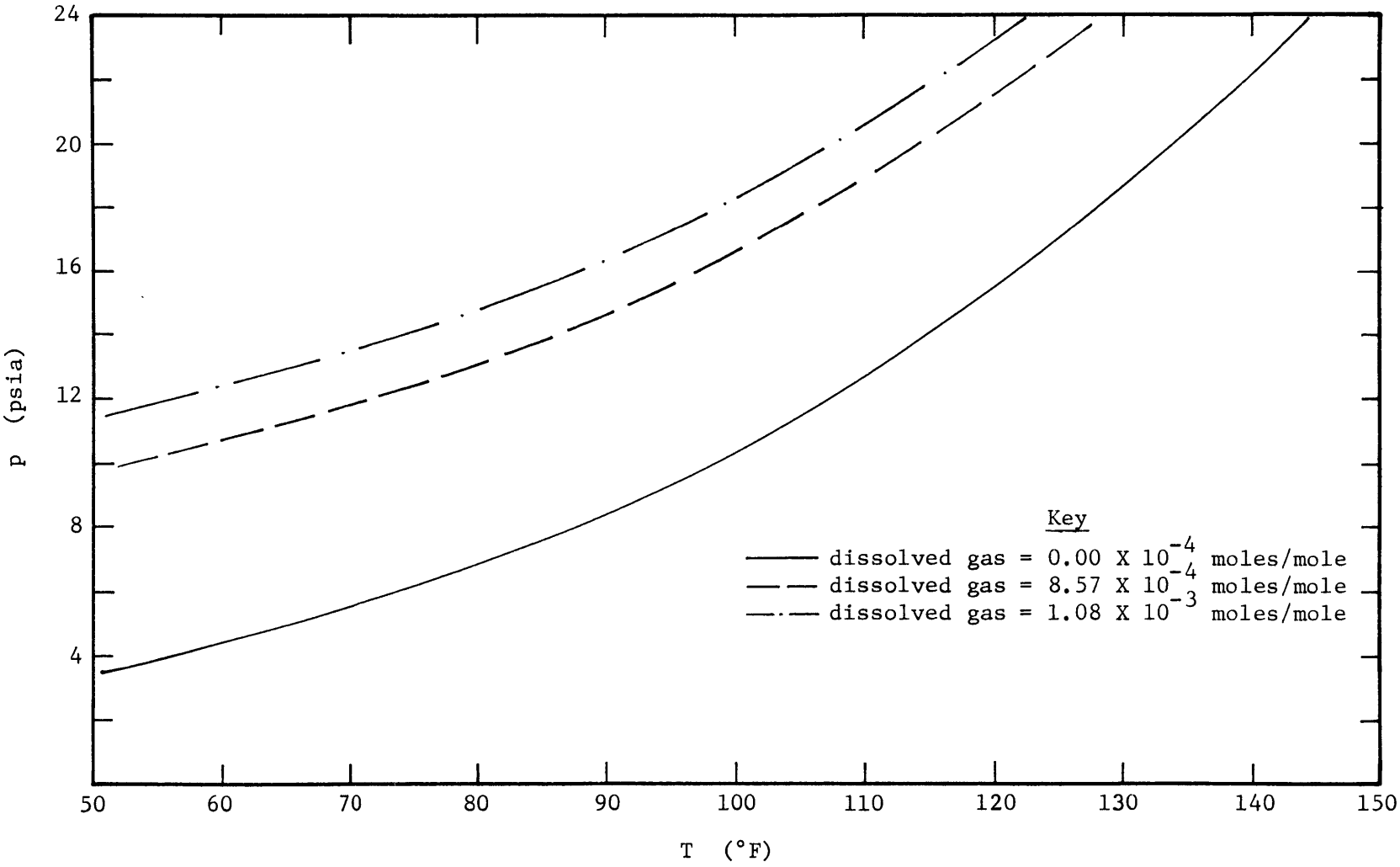

Figure 17. Two-Component Pressure-Temperature Saturation Map

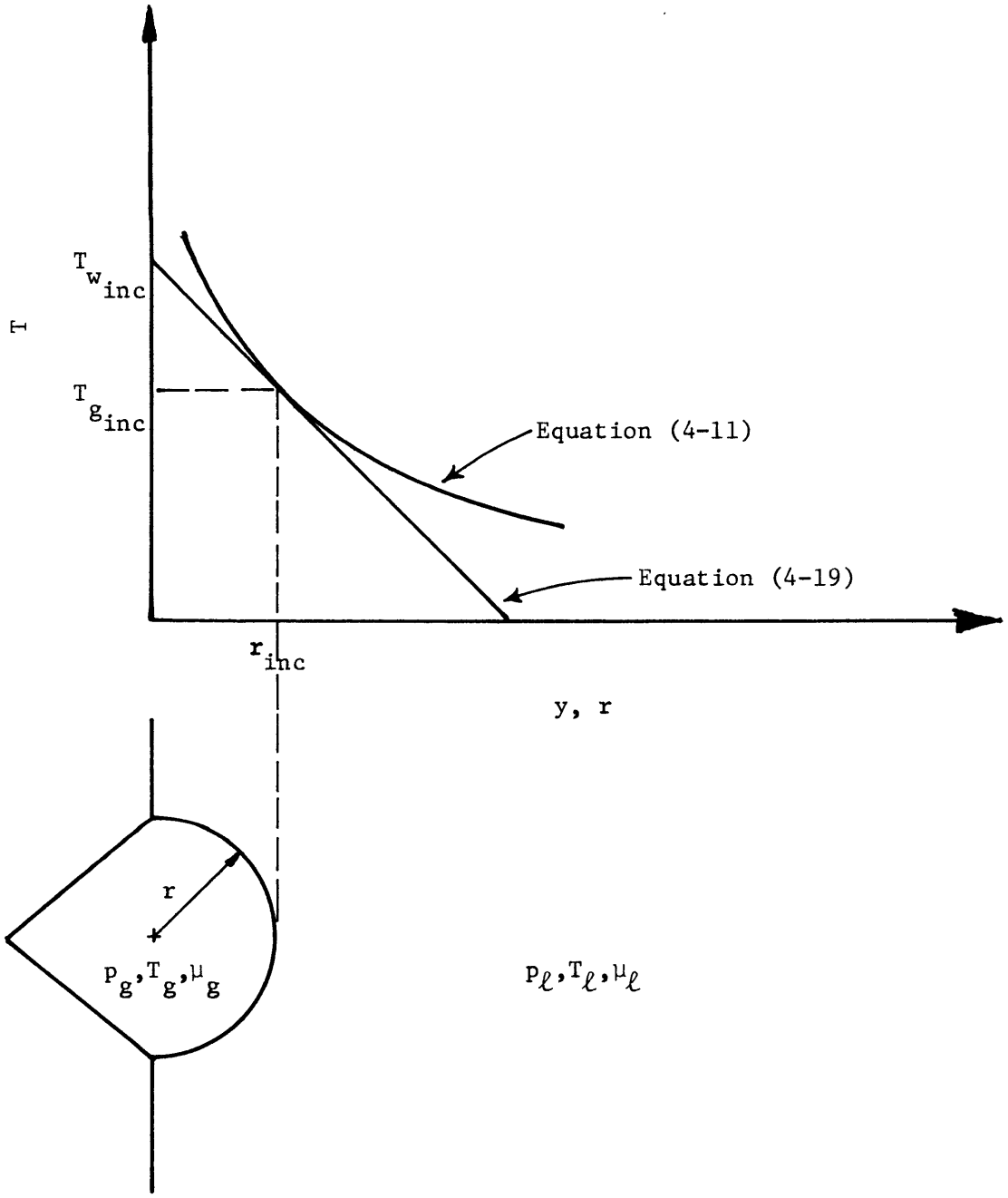

Figure 18. Incipient Bubble and Associated Variables — One-Component Case

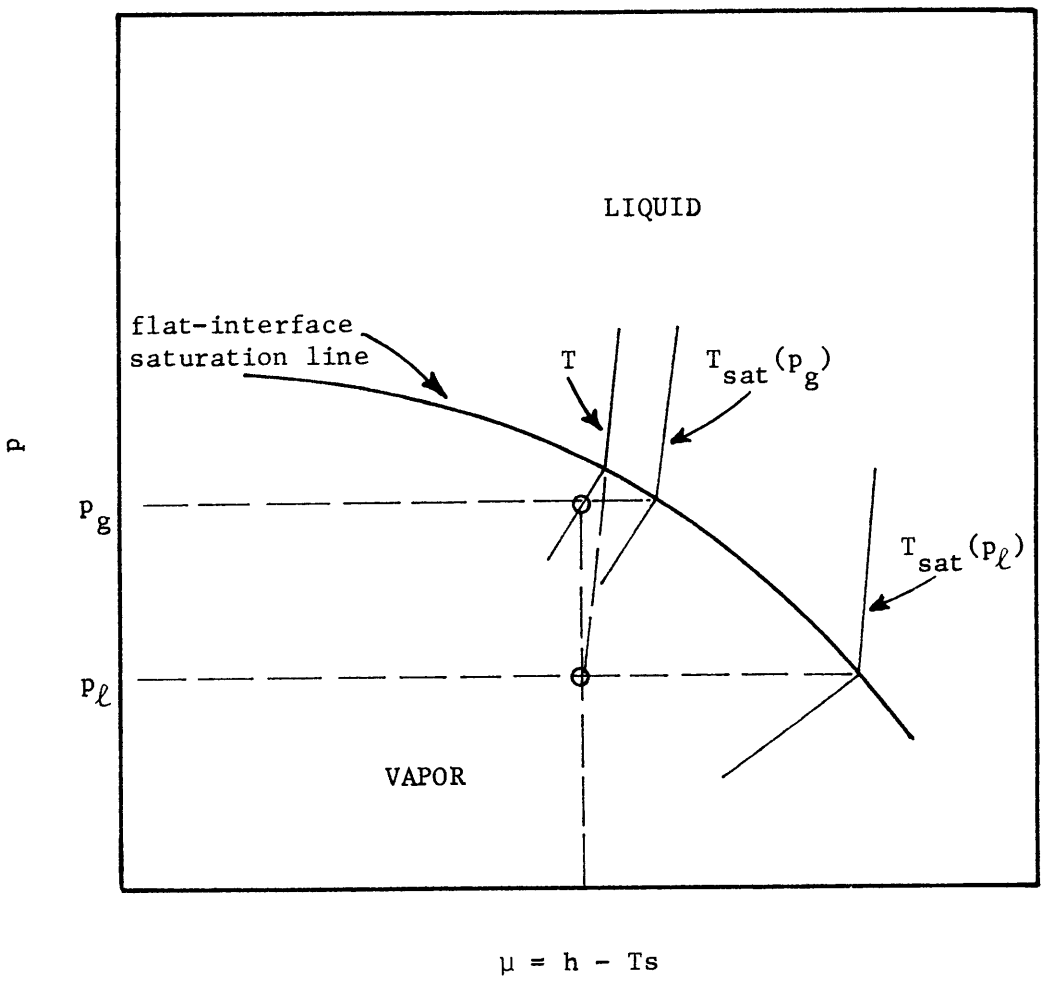

Figure 19. Chemical Potential Plot for Determination of Incipient Bubble Superheat — One-Component Case

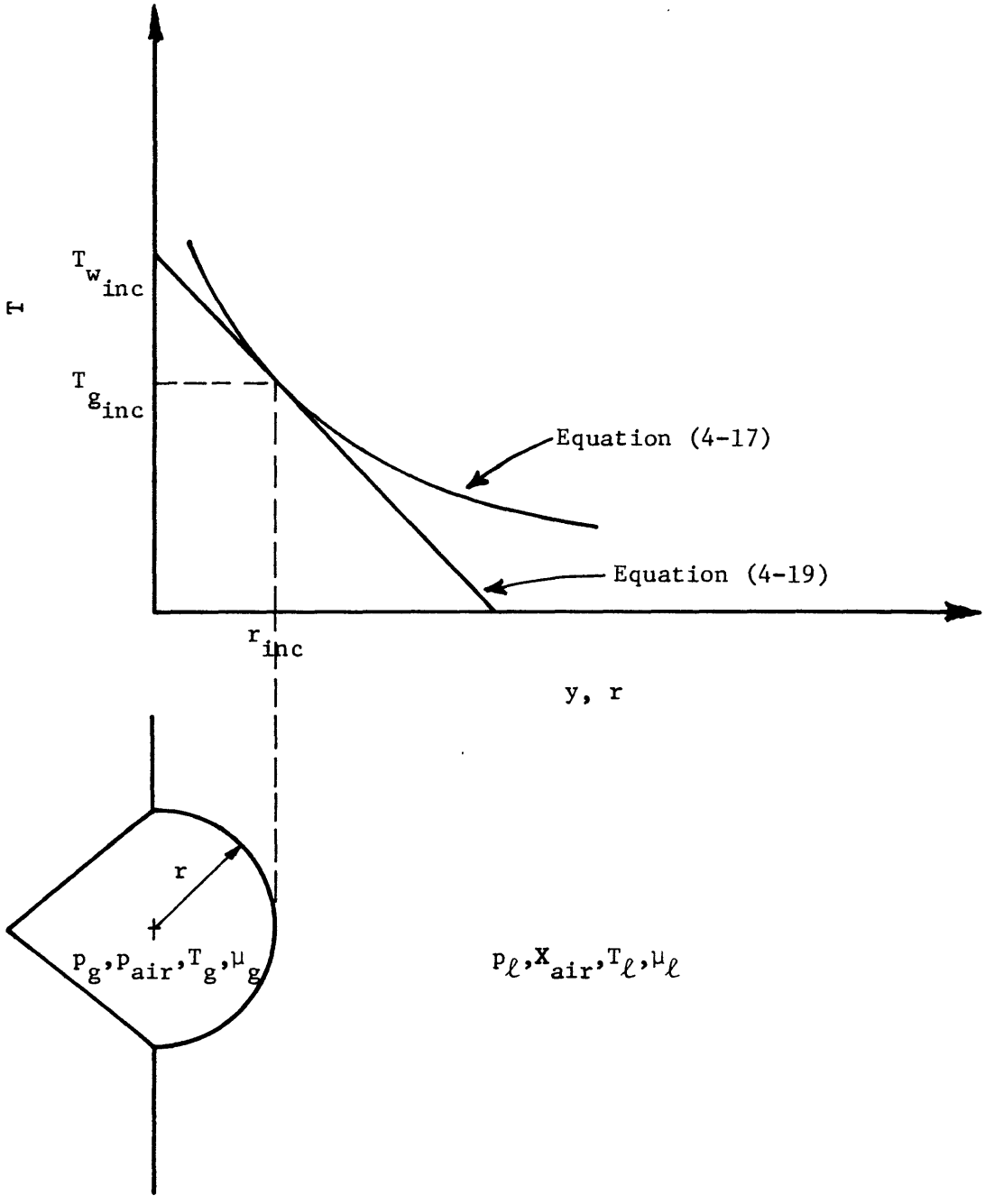

Figure 20. Incipient Bubble and Associated Variables — Two-Component Case

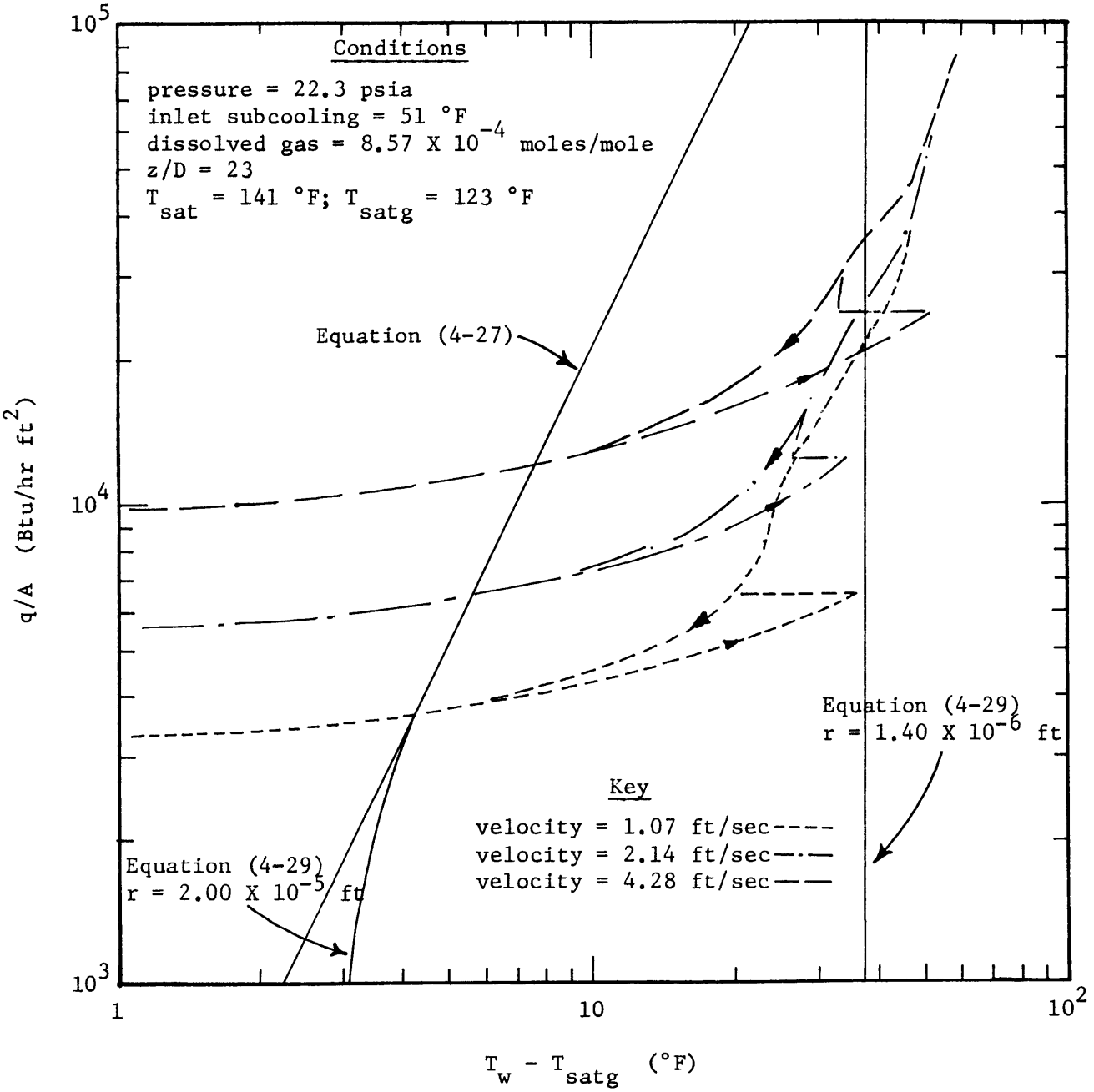

Figure 21. Gassy Flow Boiling Curves Using Adjusted Saturation Temperature

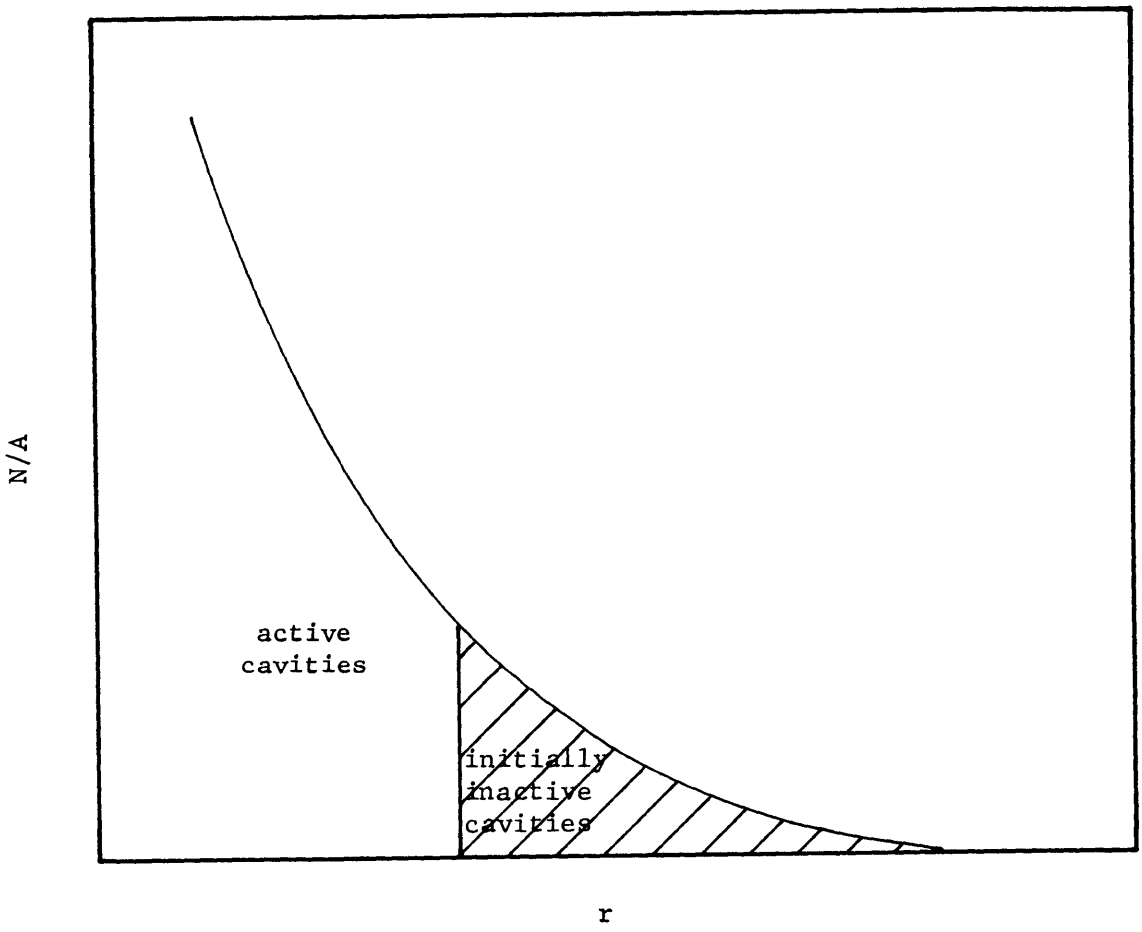

Figure 22. Proposed Active Cavity Distribution for Given Commercial Stainless Steel-Freon-113 Combination

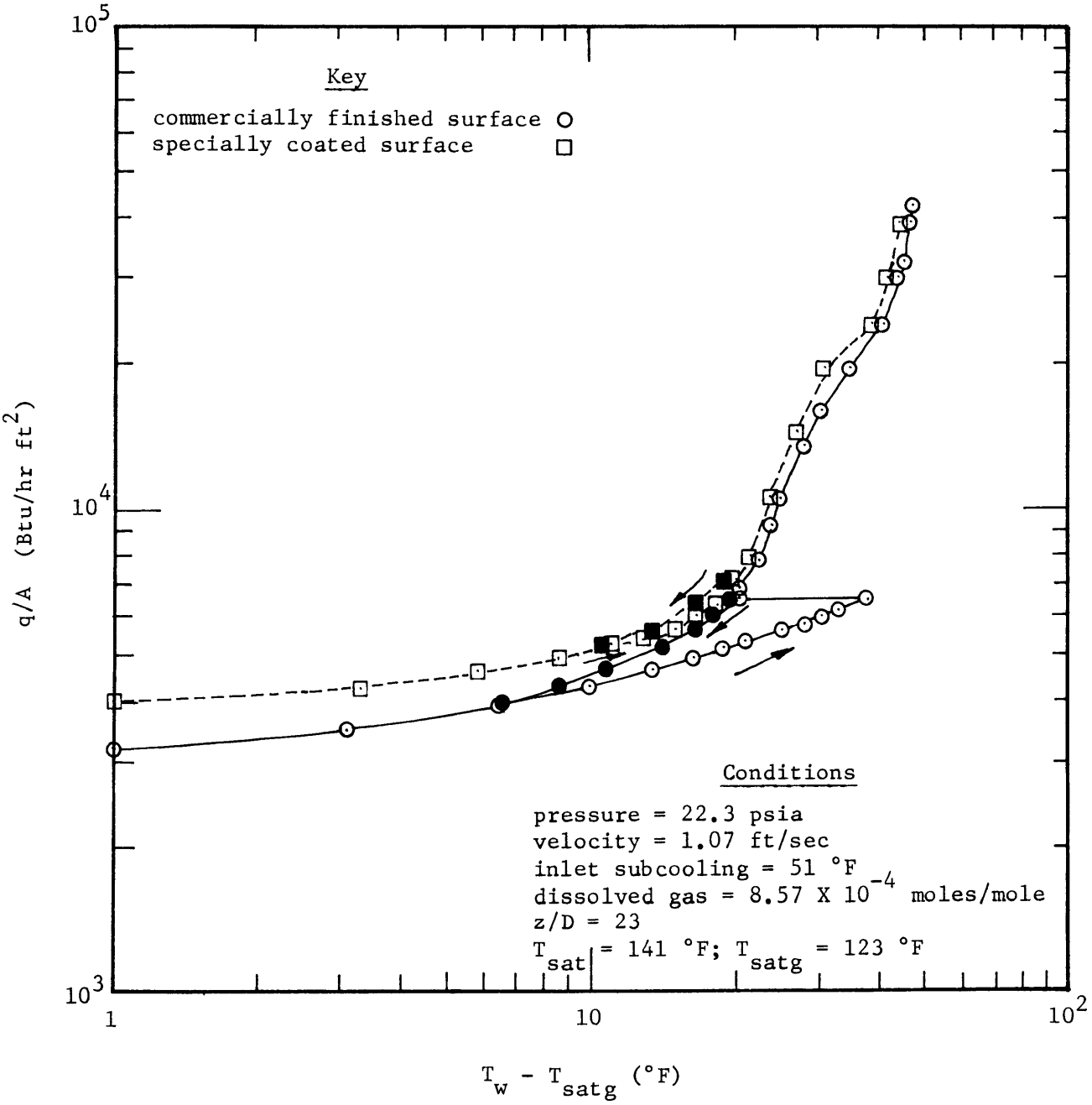

Figure 23. Comparison of Flow Boiling Curves for Smooth and Specially-Coated Surfaces

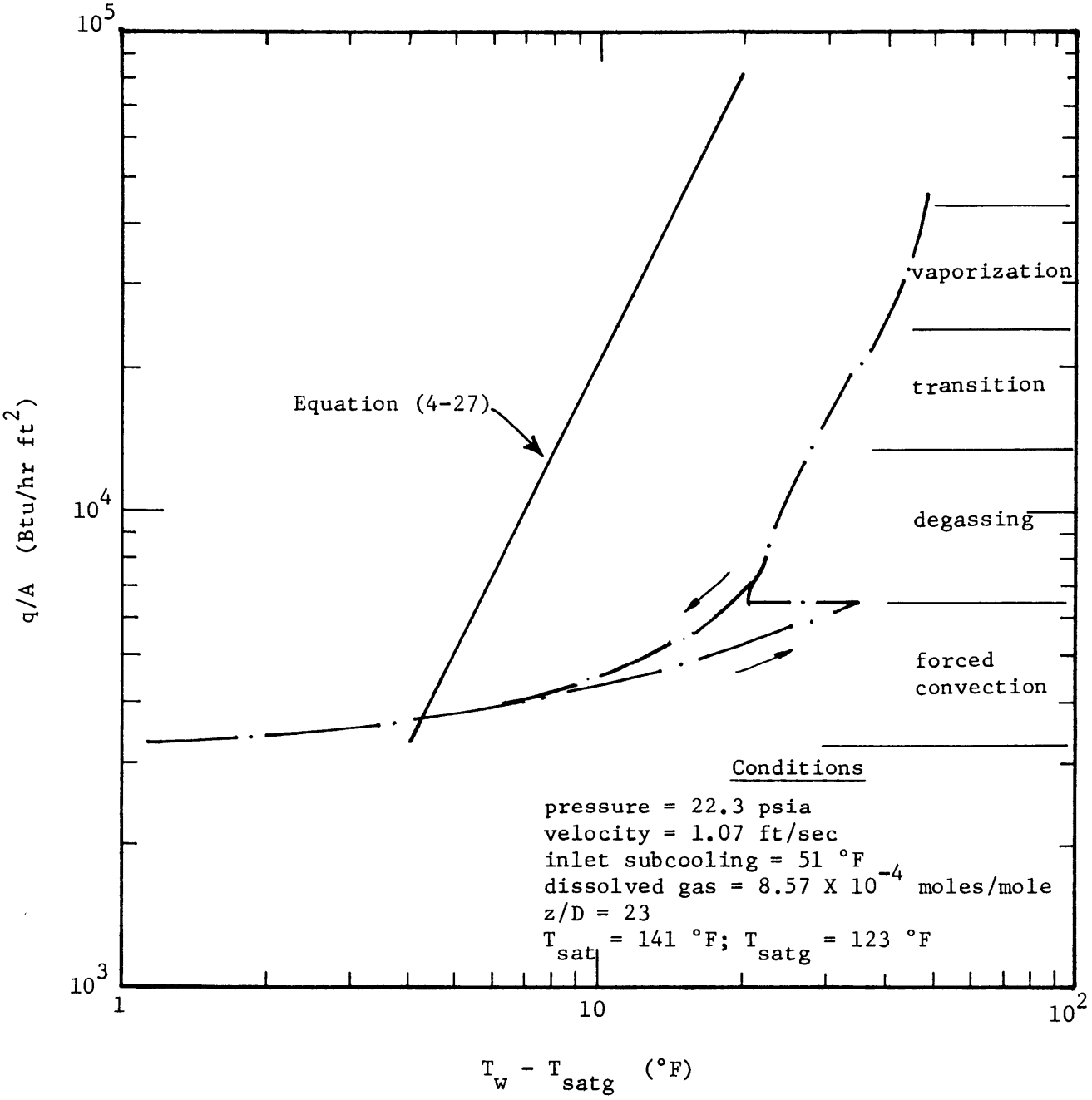

Figure 24. Gassy Flow Boiling Curve Showing Various Heat Transfer Modes

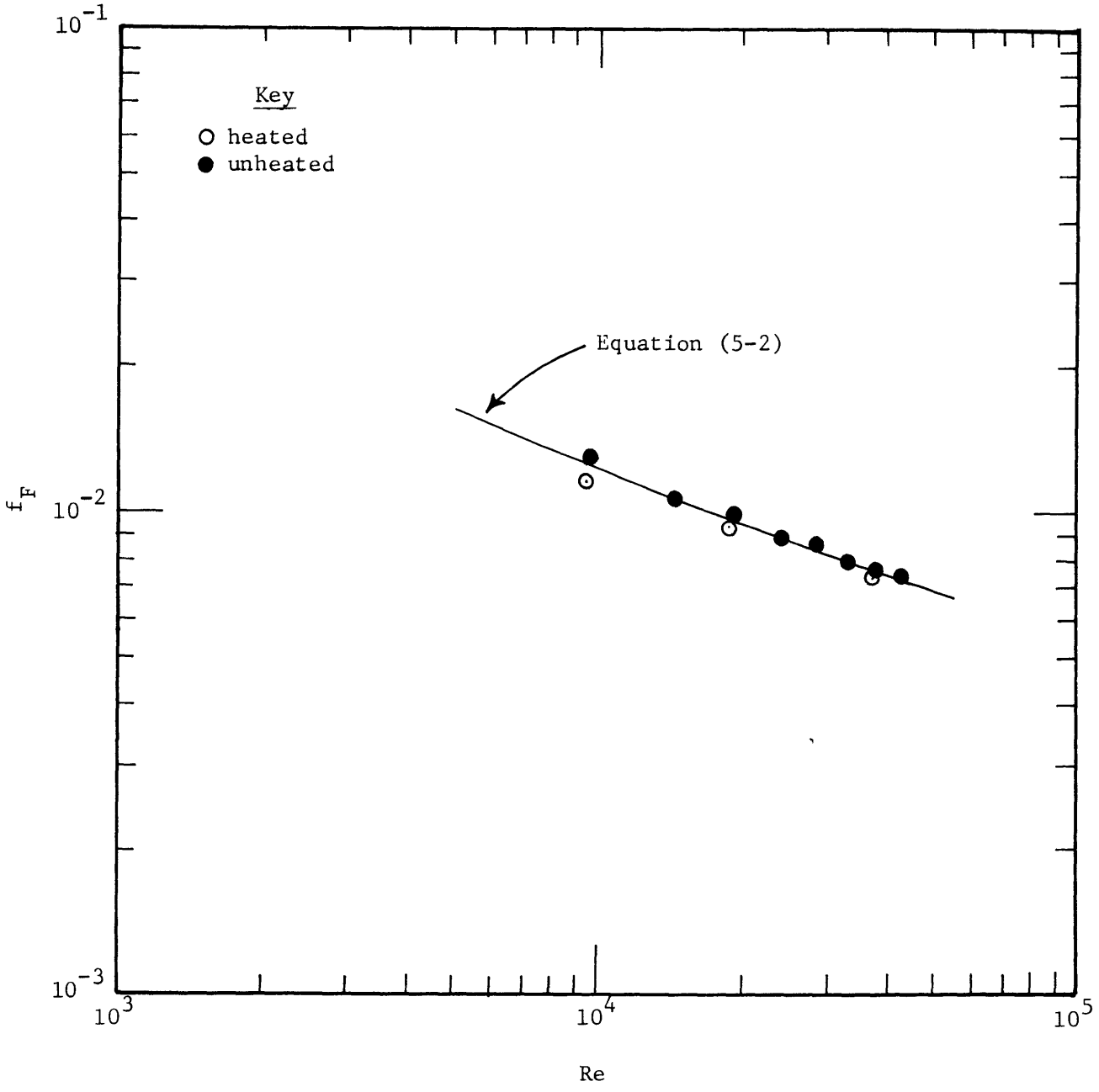

Figure 25. Single-Phase Pressure Drop Results

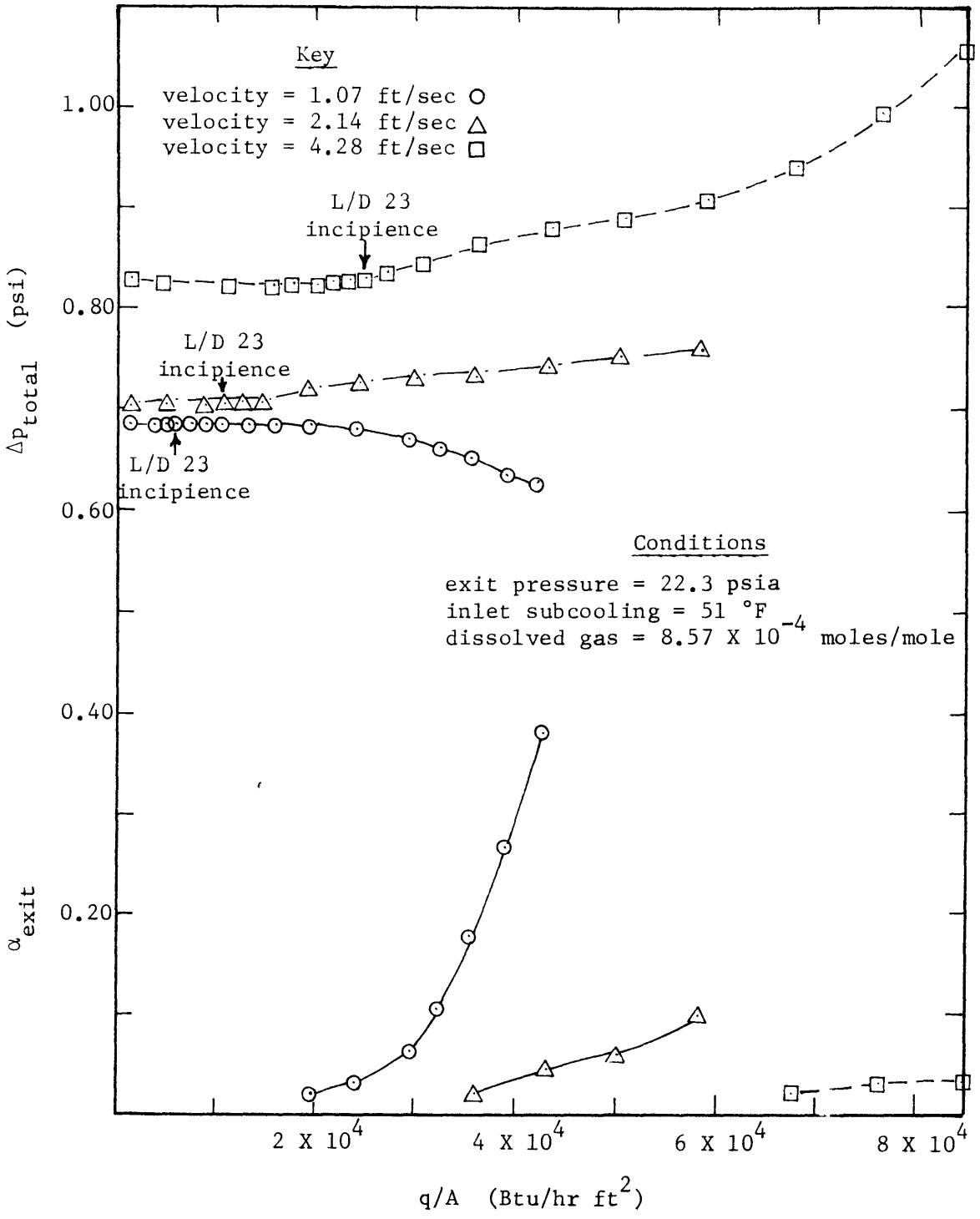

Figure 26. Mass Velocity Effects on Total Pressure Drop and Exit Void Fraction

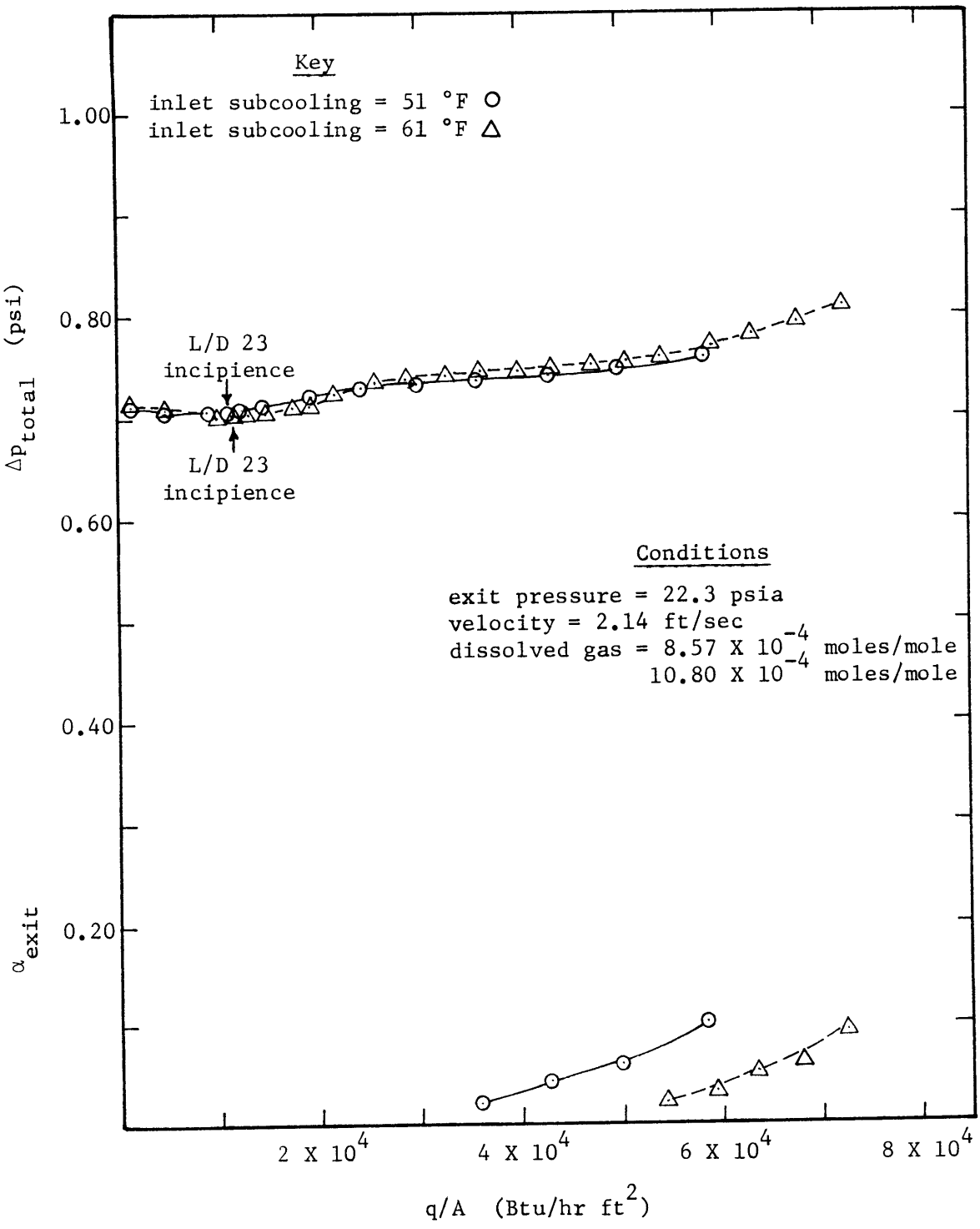

Figure 27. Inlet Subcooling Effects on Total Pressure Drop and Exit Void Fraction

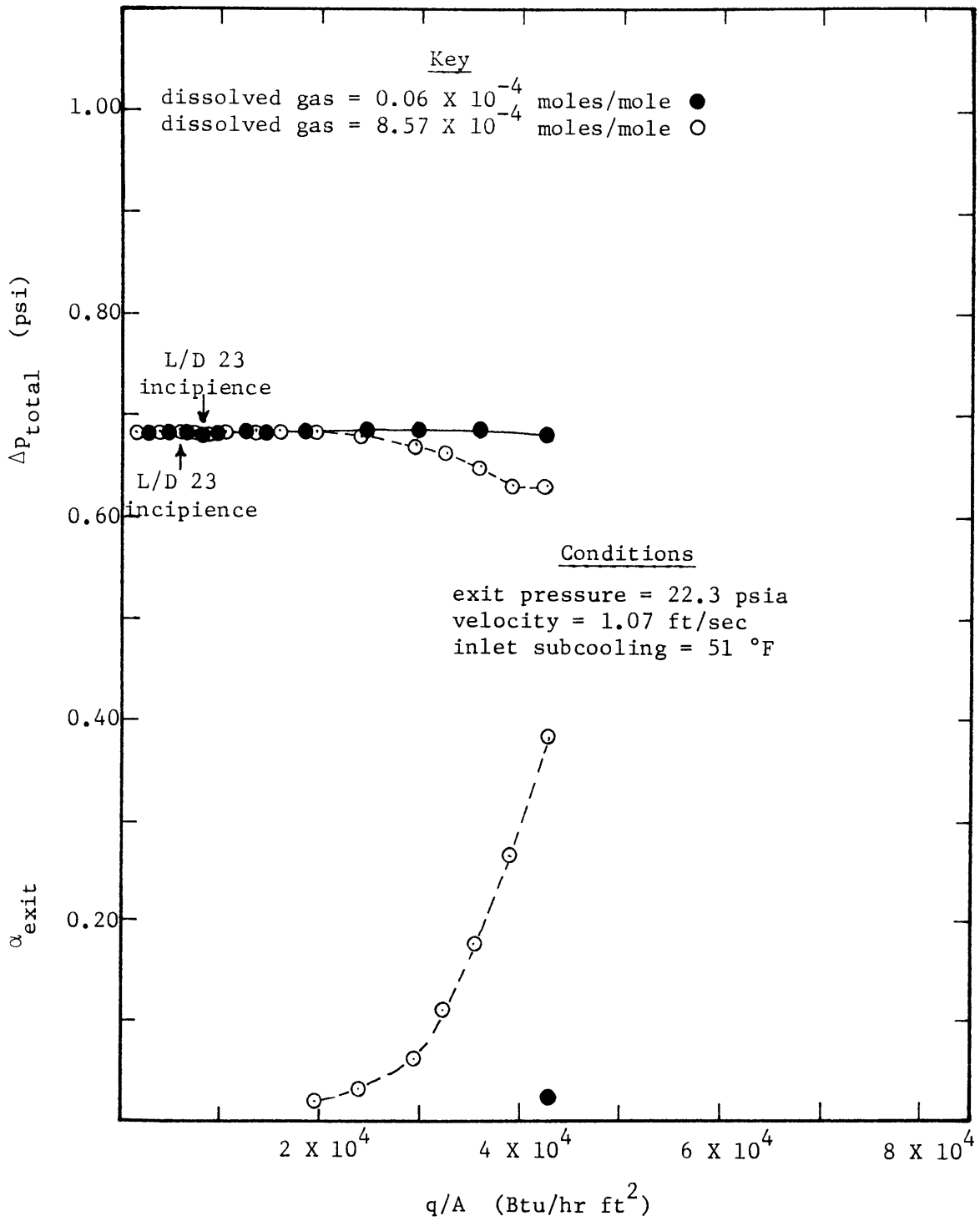

Figure 28. Dissolved Gas Effects on Total Pressure Drop and Exit Void Fraction

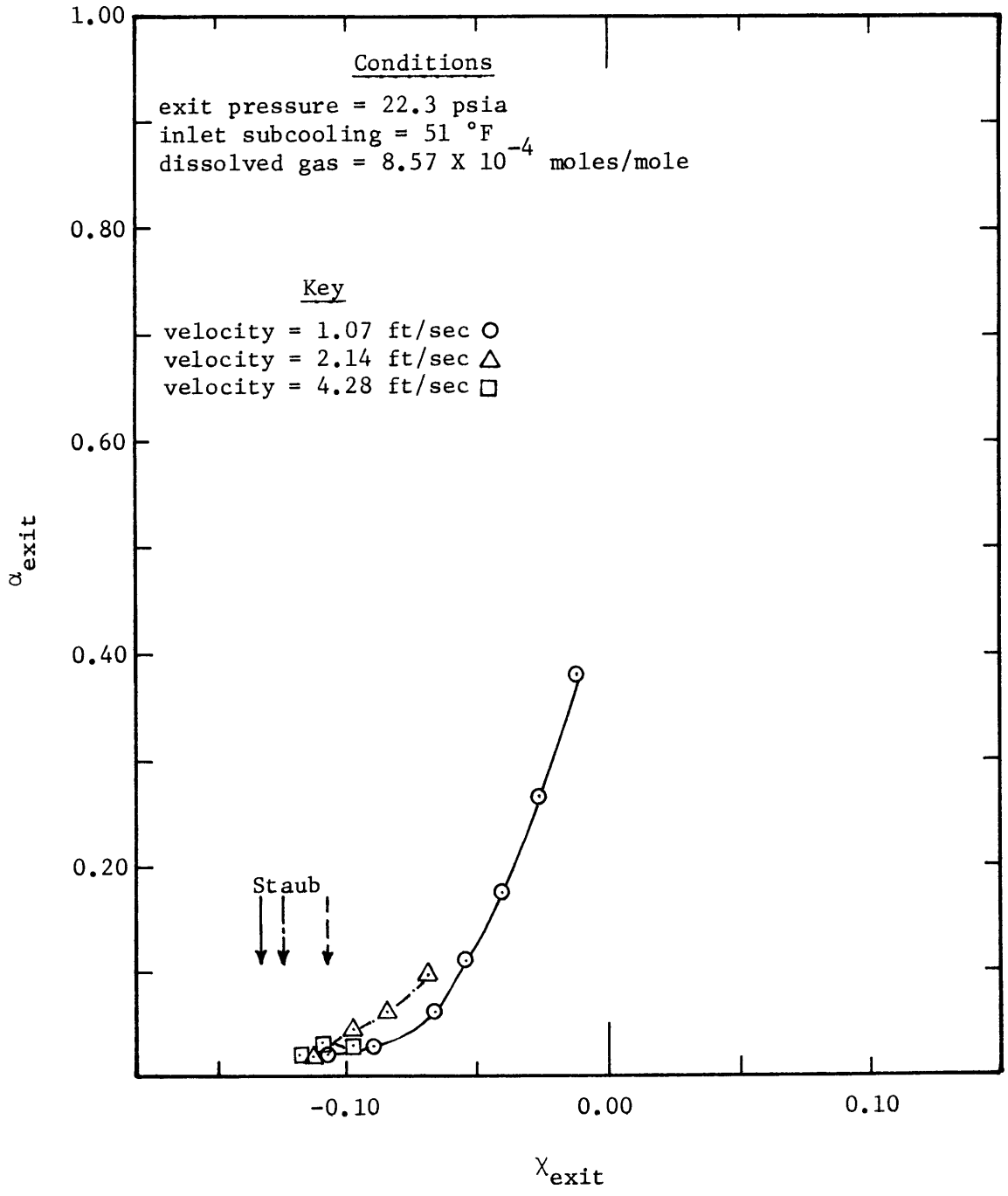

Figure 29. Mass Velocity Effects on Exit Void Fraction — Quality Coordinates

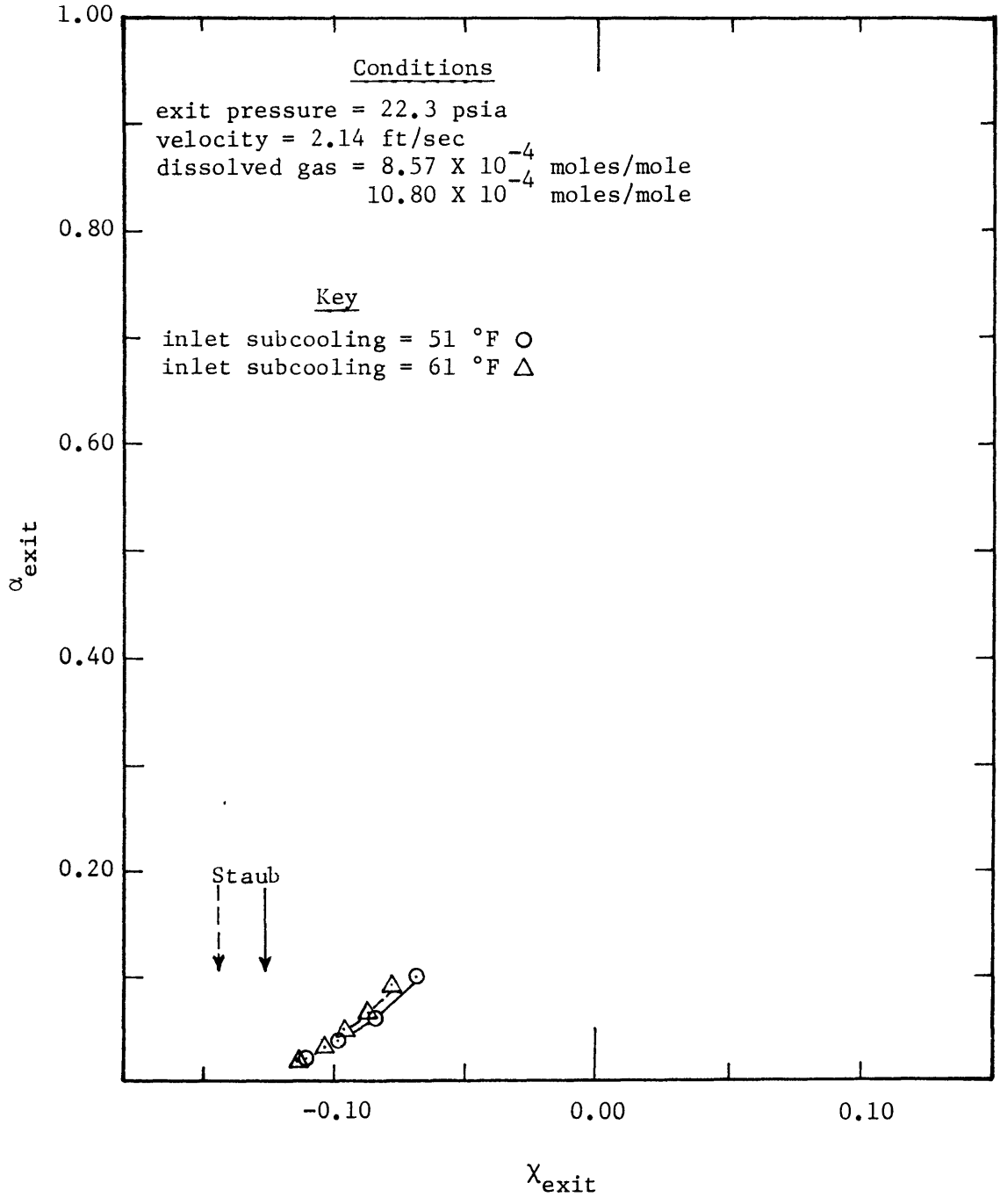

Figure 30. Inlet Subcooling Effects on Exit Void Fraction — Quality Coordinates

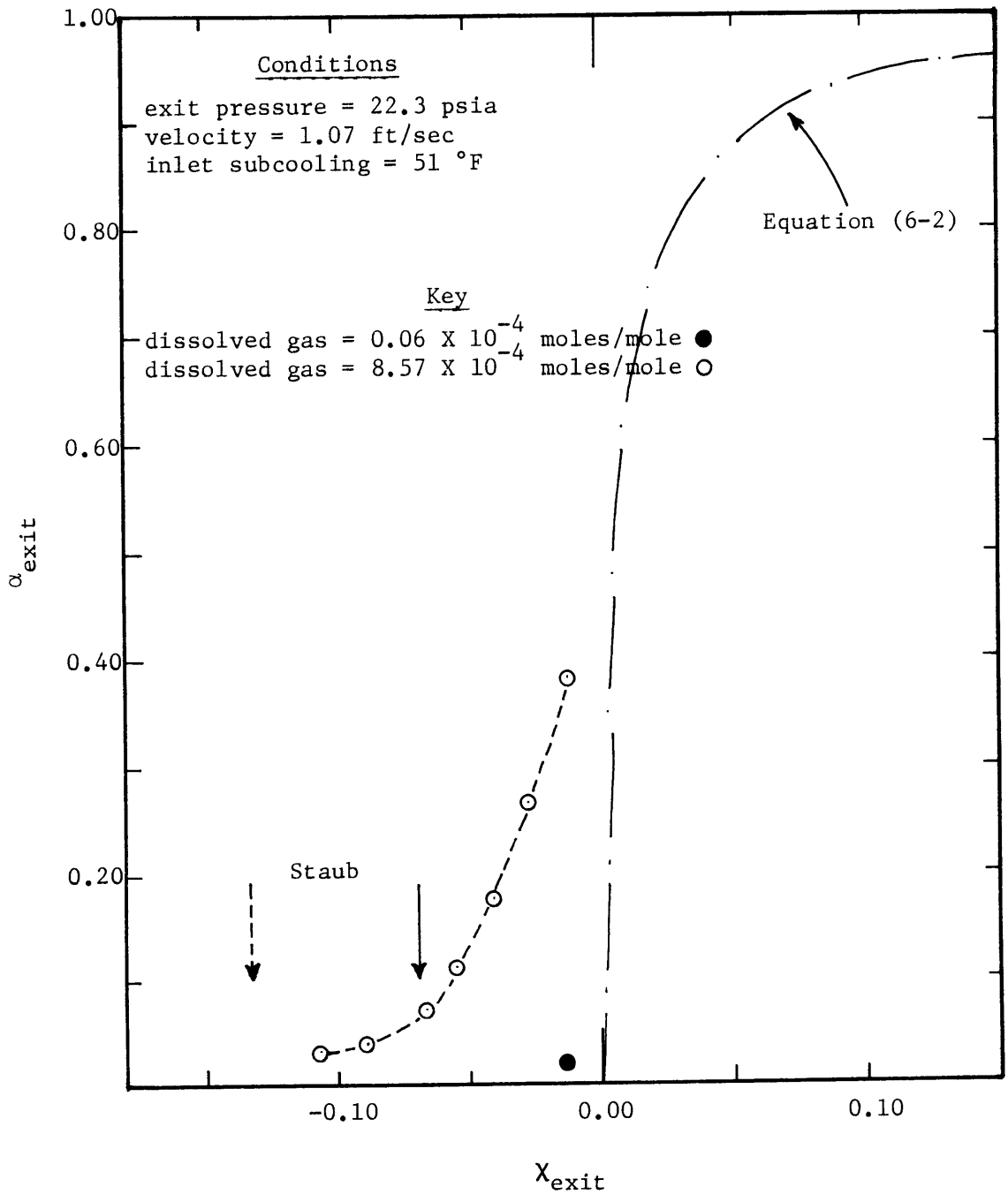

Figure 31. Dissolved Gas Effects on Exit Void Fraction — Quality Coordinates

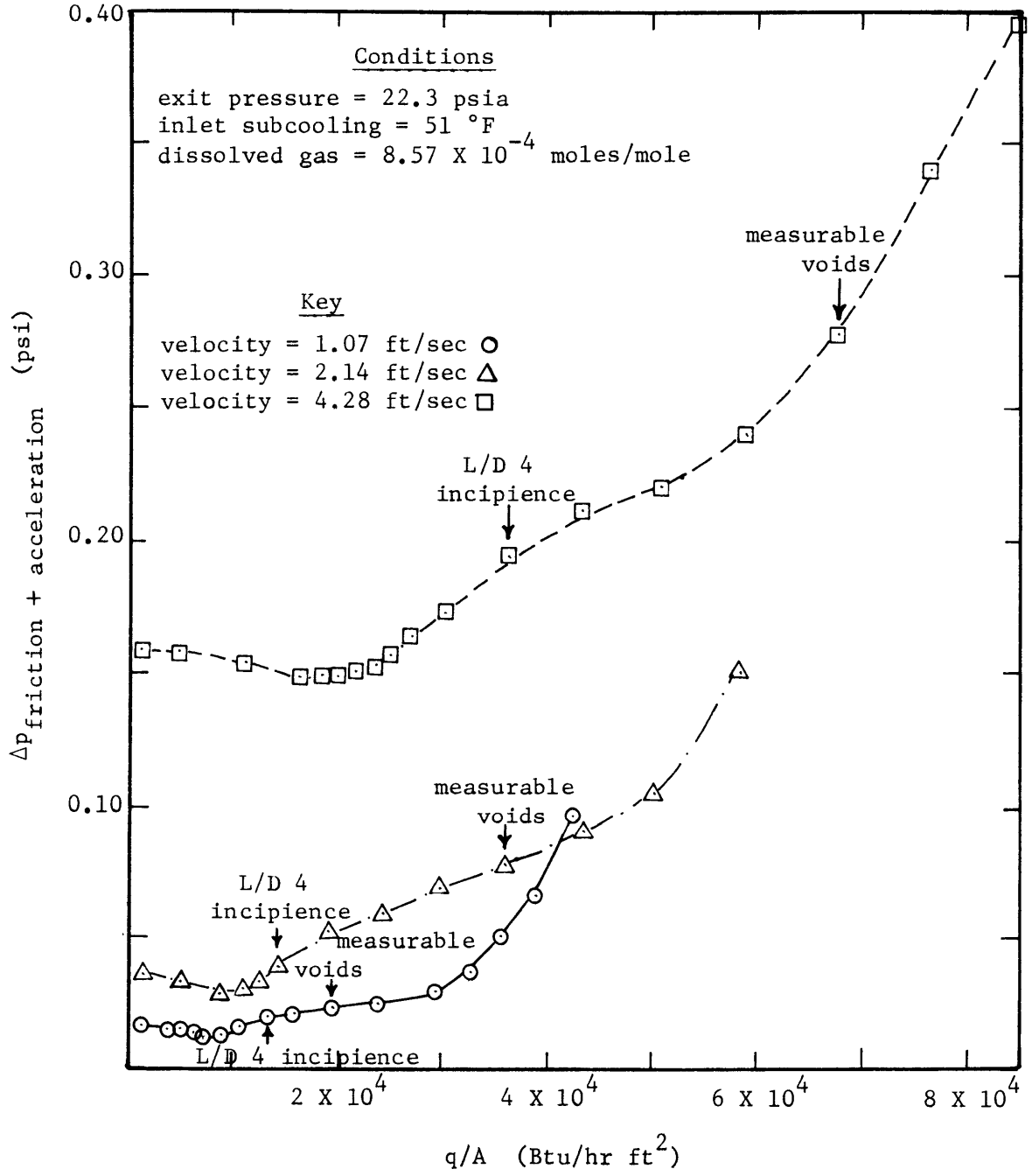

Figure 32. Mass Velocity Effects on Friction-Acceleration Component of Pressure Drop

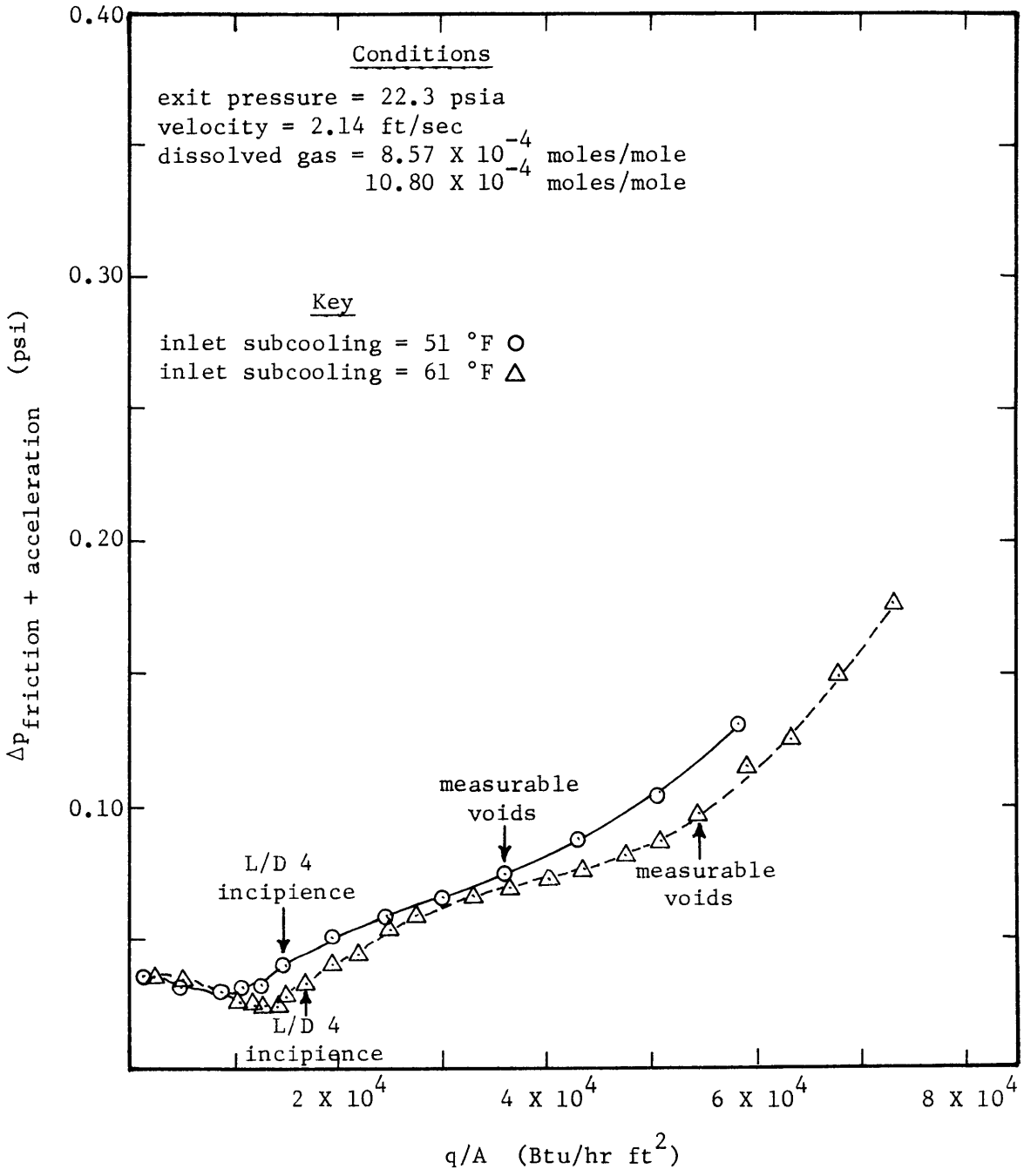

Figure 33. Inlet Subcooling Effects on Friction-Acceleration Component of Pressure Drop

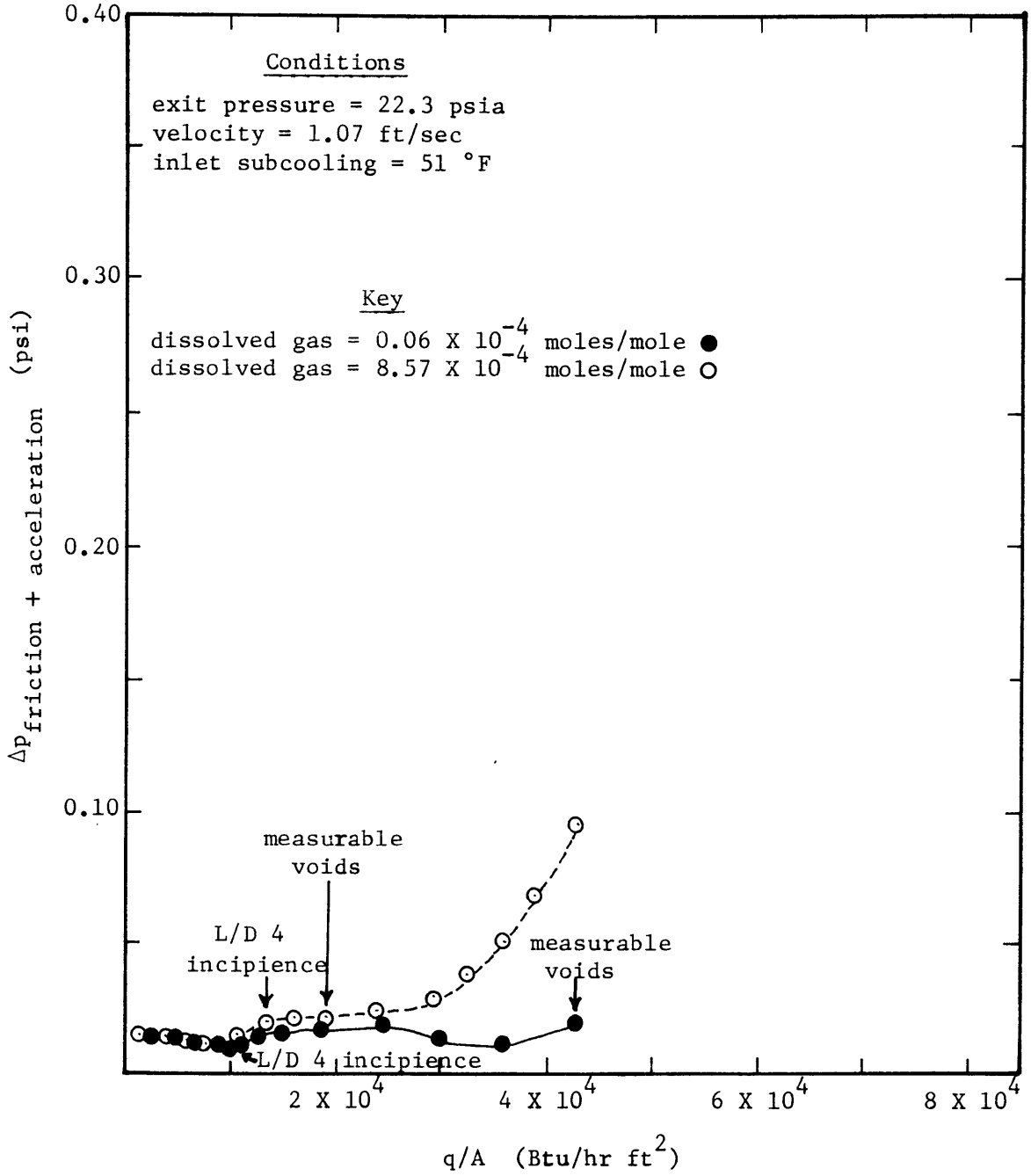

Figure 34. Dissolved Gas Effects on Friction-Acceleration Component of Pressure Drop

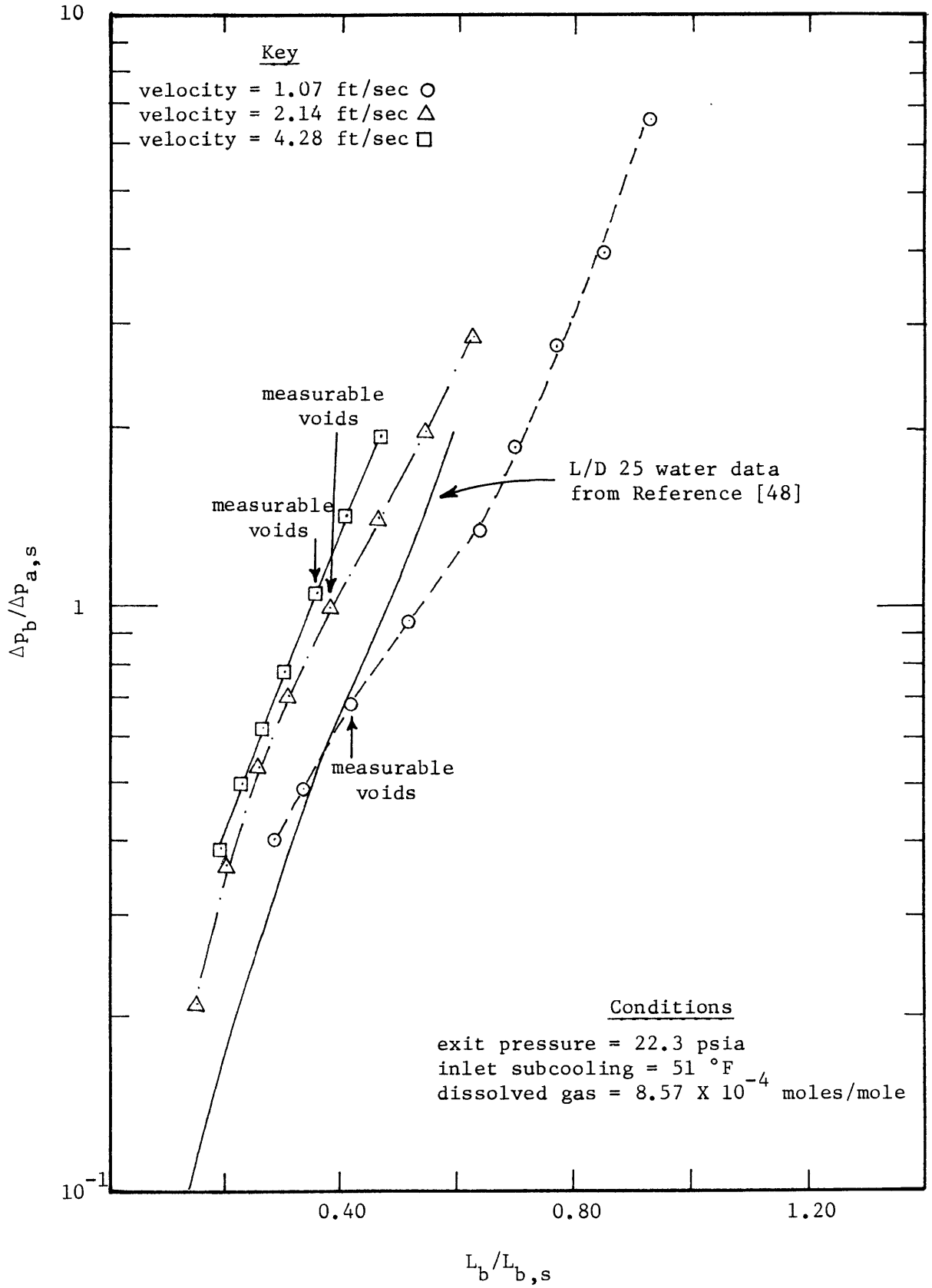

Figure 35. Mass Velocity Effects on Friction-Acceleration Component of Pressure Drop — Degassed Correlation Coordinates

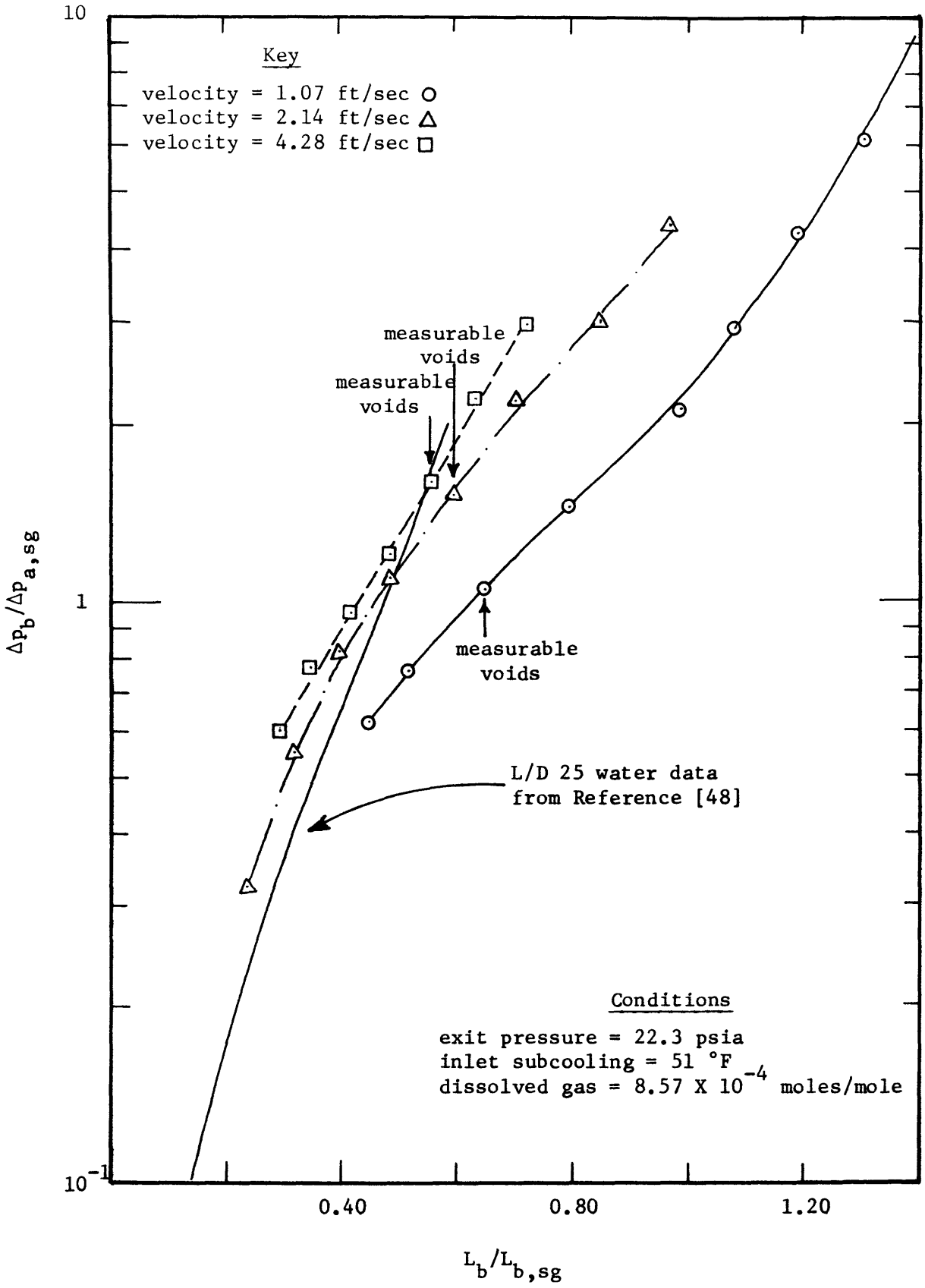

Figure 36. Mass Velocity Effects on Friction-Acceleration Component of Pressure Drop — Gassy Correlation Coordinates

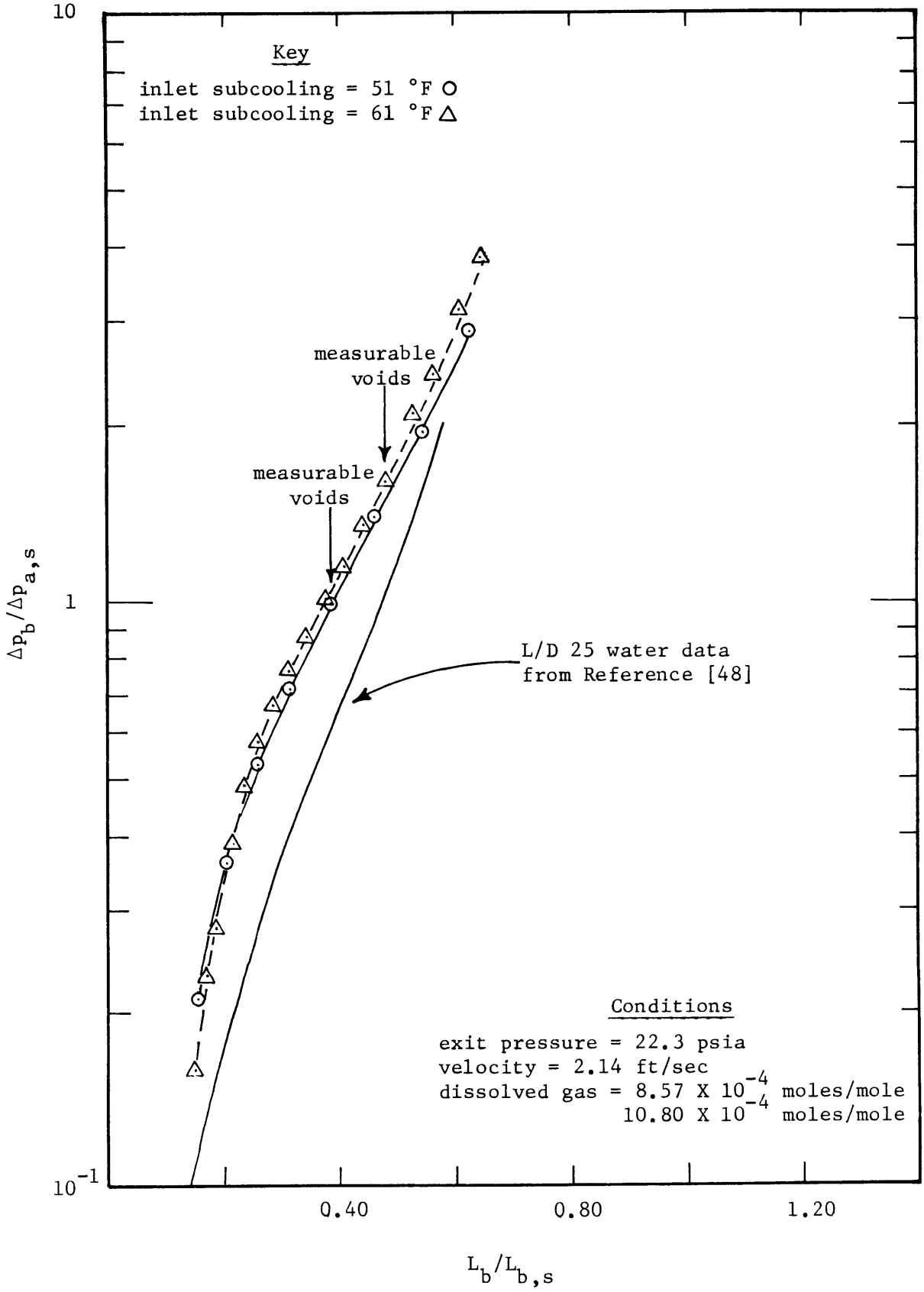

Figure 37. Inlet Subcooling Effects on Friction-Acceleration Component of Pressure Drop — Degassed Correlation Coordinates

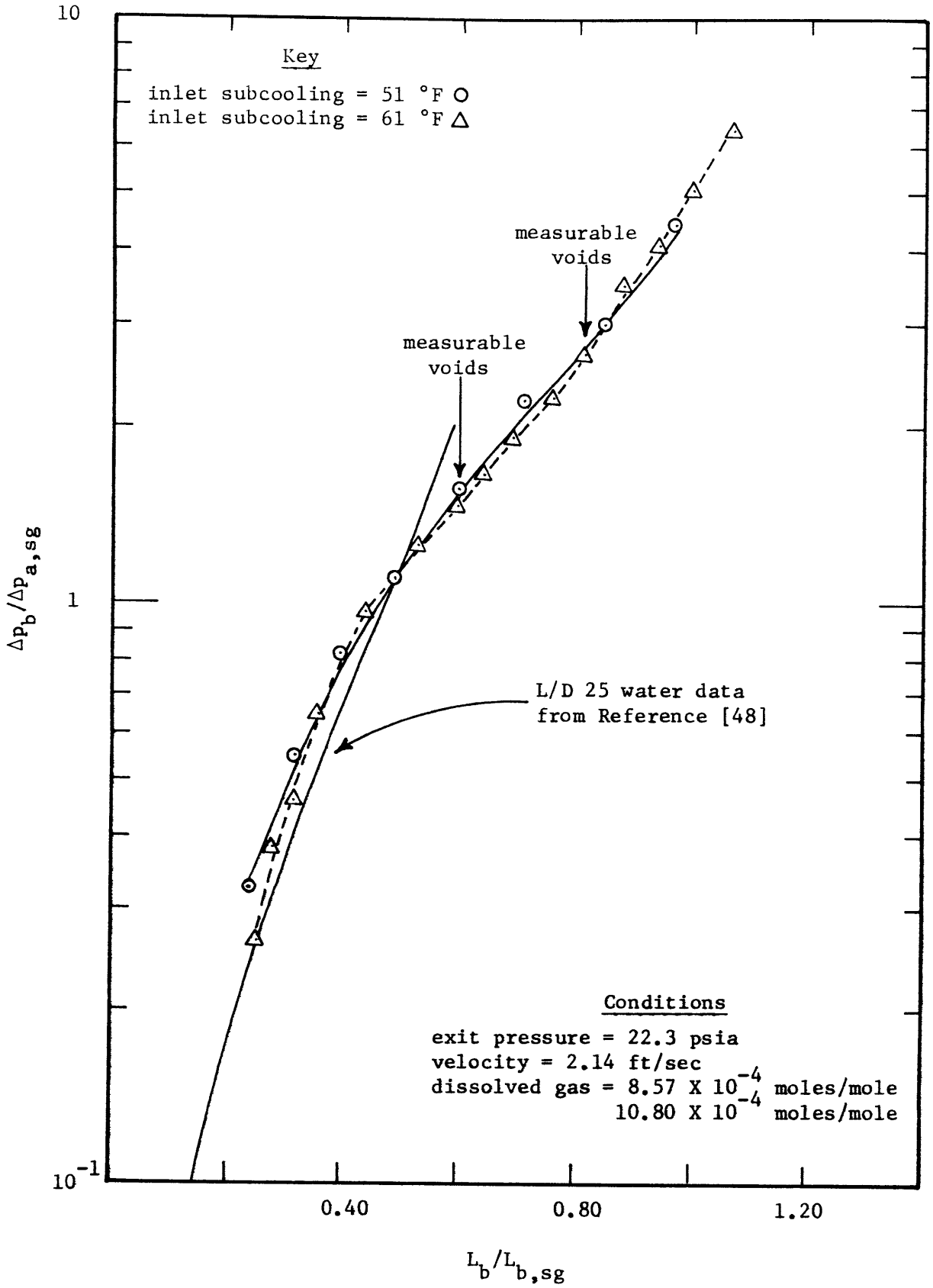

Figure 38. Inlet Subcooling Effects on Friction-Acceleration Component of Pressure Drop — Gassy Correlation Coordinates

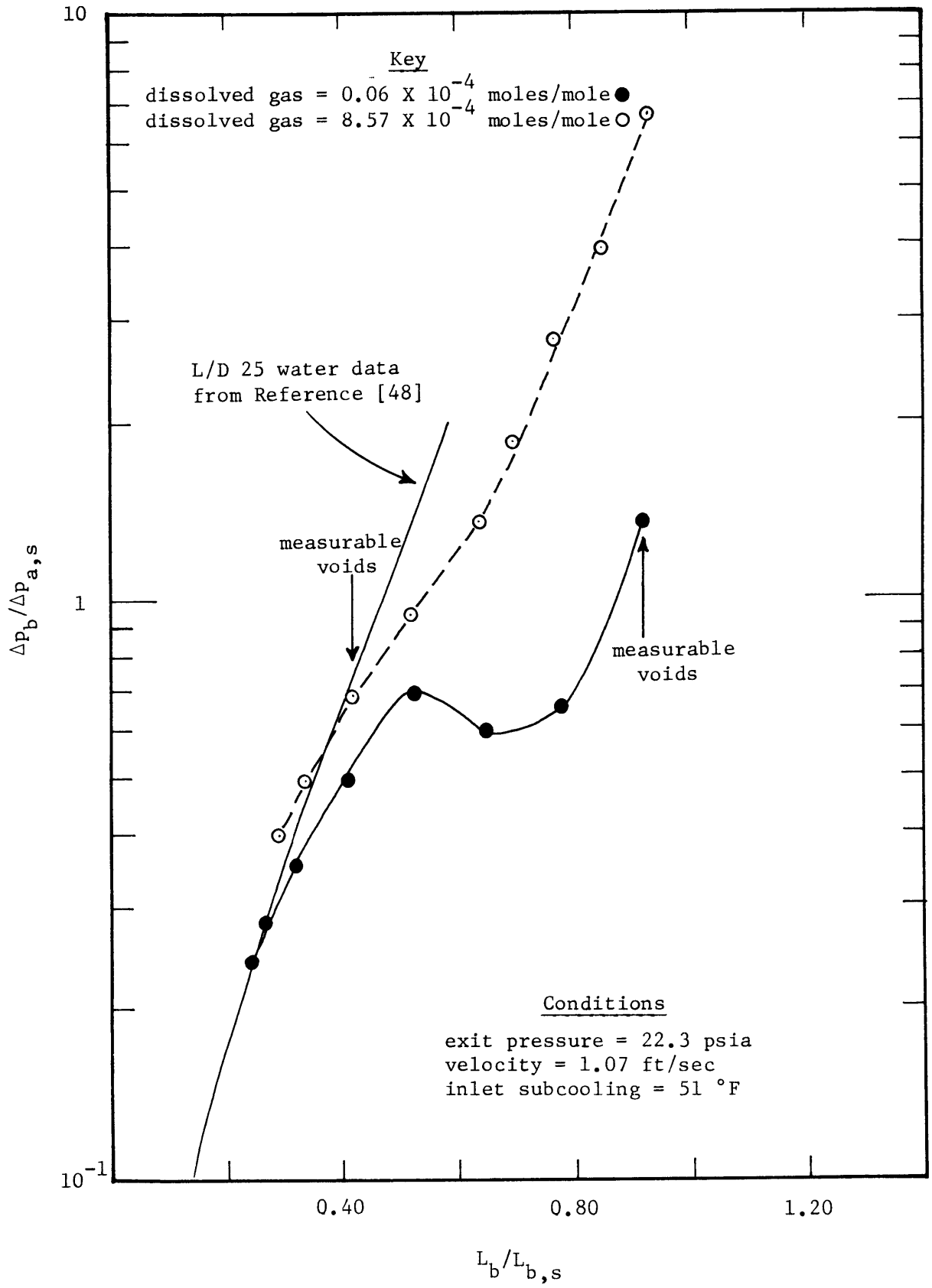

Figure 39. Dissolved Gas Effects on Friction-Acceleration Component of Pressure Drop — Degassed Correlation Coordinates

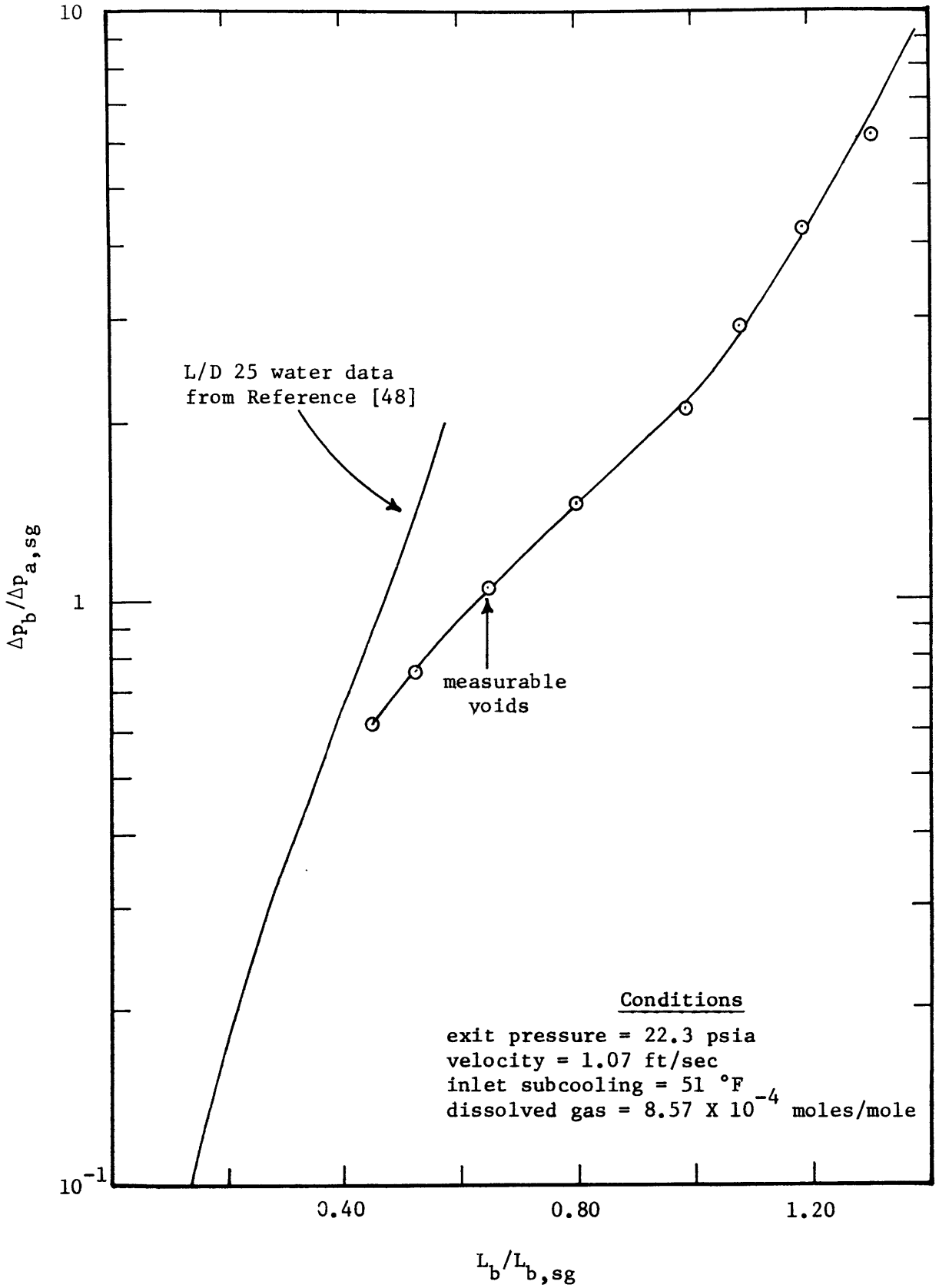

Figure 40. Dissolved Gas Effects on Friction-Acceleration Component of Pressure Drop — Gassy Correlation Coordinates

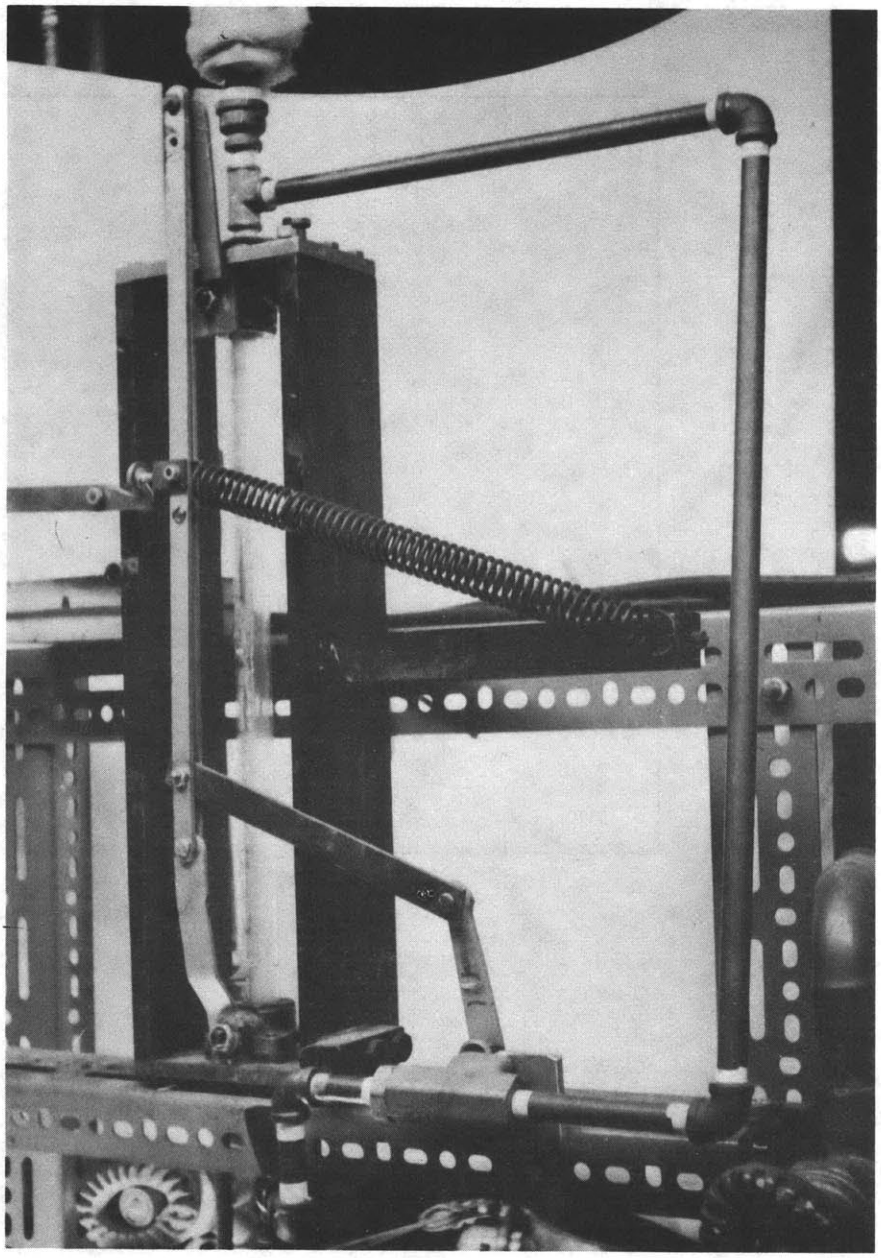

Figure 41. Photograph of Void Fraction Trap Measurement Section

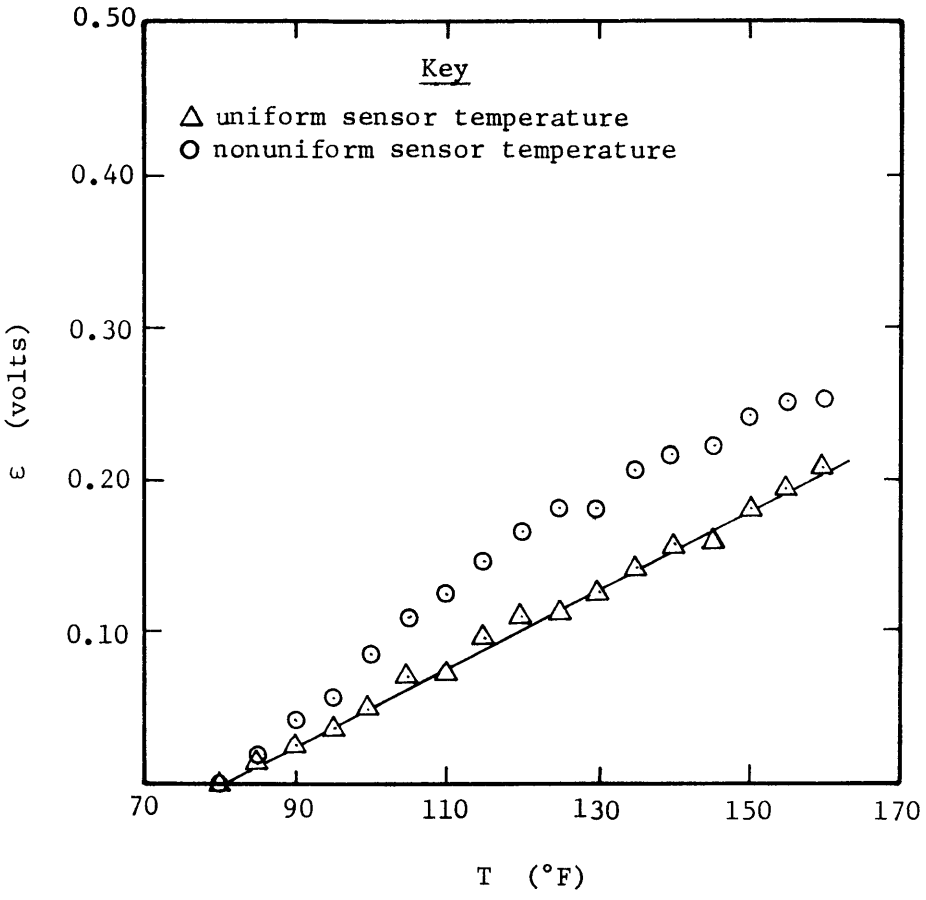

Figure 42. Gas-Phase Temperature Calibration of
of Capacitance Void Meter

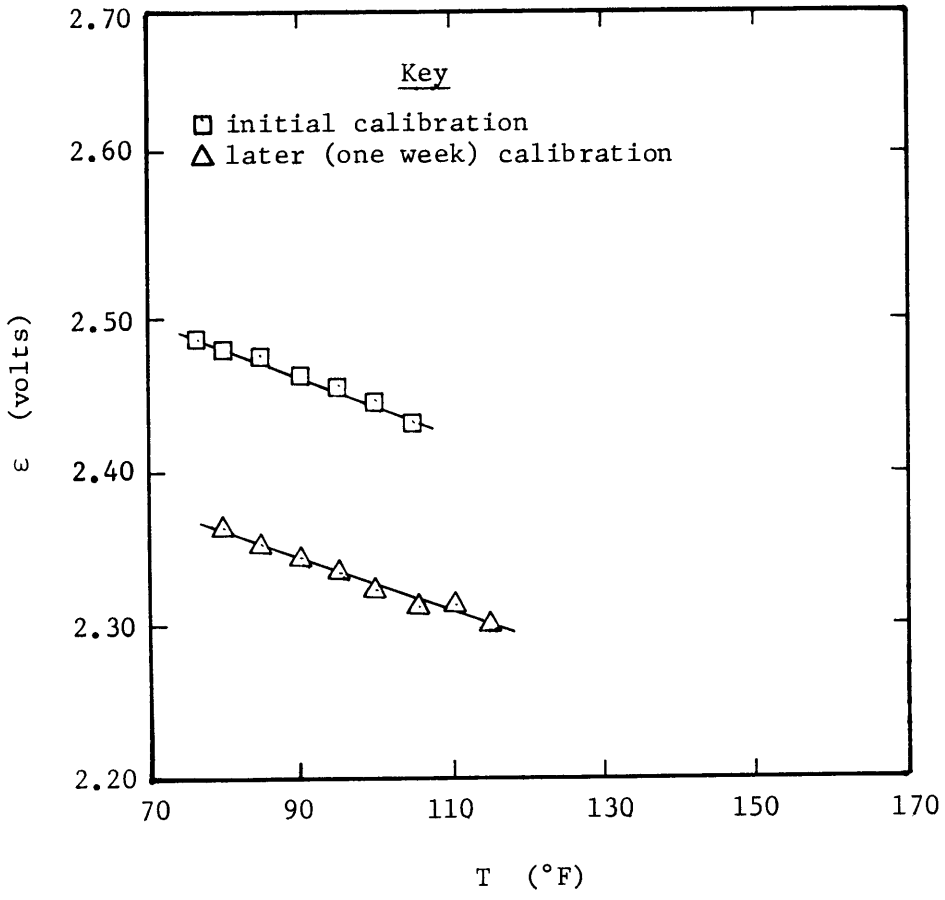

Figure 43. Liquid-Phase Temperature Calibration of Capacitance Void Meter

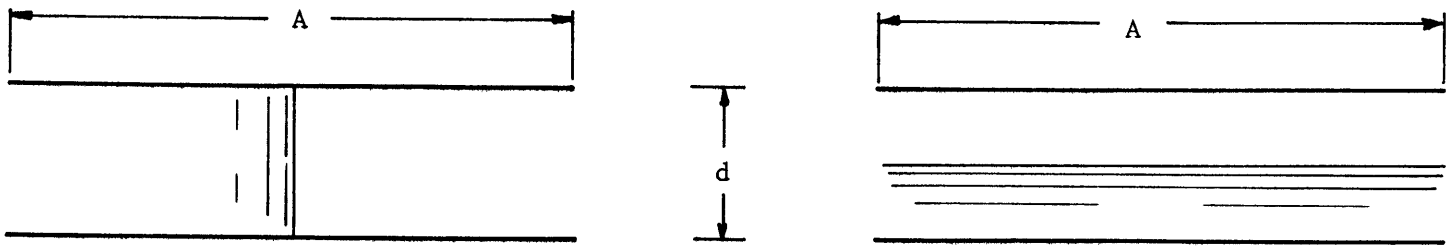

$$\alpha = 0.50$$

$$C = 0.50 \frac{A}{d} (\varepsilon_\ell + \varepsilon_g)$$

$$\varepsilon_{TP} = 0.50 (\varepsilon_\ell + \varepsilon_g)$$

$$\alpha = 0.50$$

$$C = 2.00 \frac{A}{d} \frac{\varepsilon_\ell \varepsilon_g}{\varepsilon_\ell + \varepsilon_g}$$

$$\varepsilon_{TP} = 2.00 \frac{\varepsilon_\ell \varepsilon_g}{\varepsilon_\ell + \varepsilon_g}$$

Figure 44. Comparison of Measured Capacitances of Idealized Slug Flow and Idealized Stratified Flow Situations

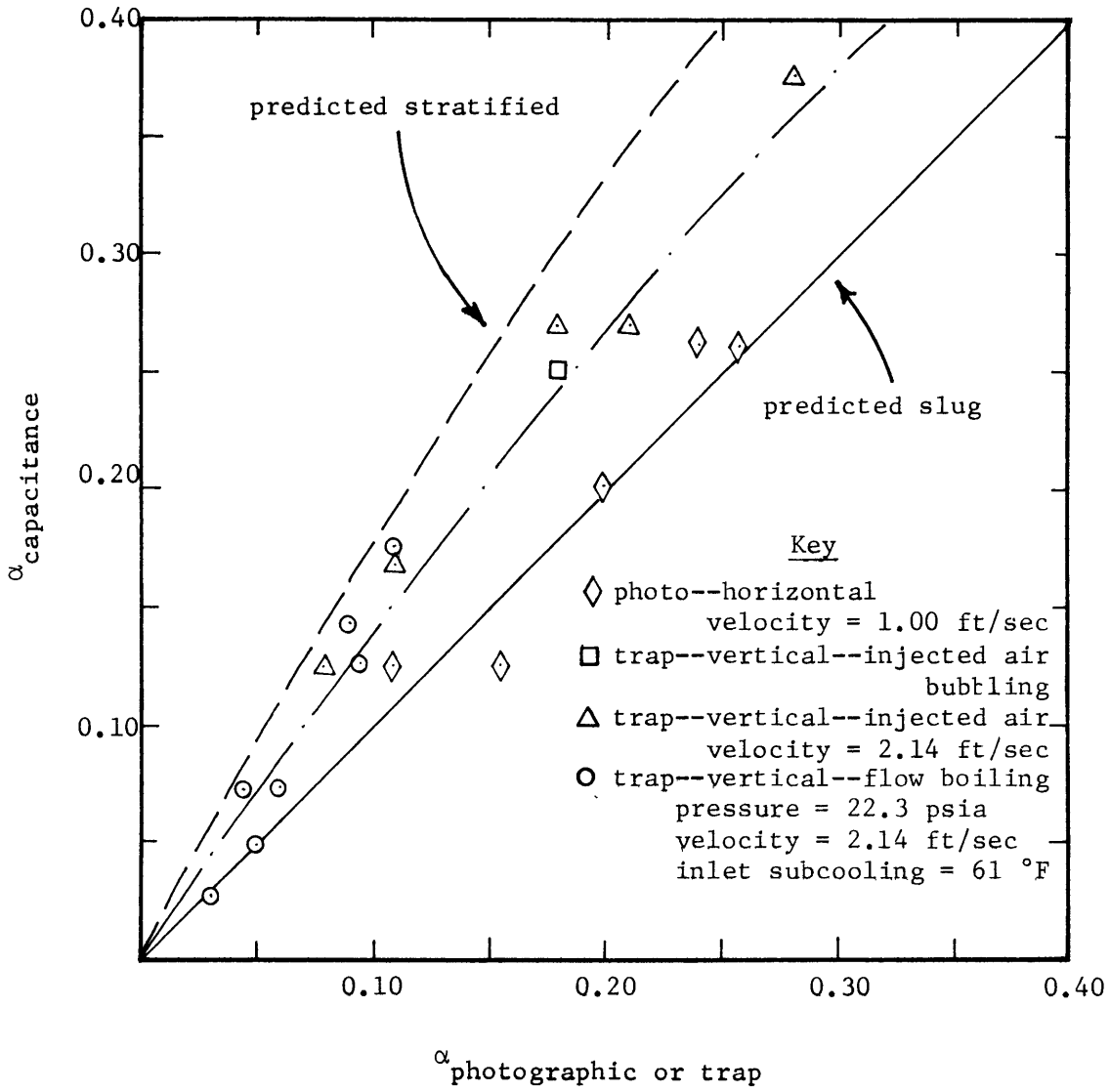

Figure 45. Comparative Predictions and Data for Various Void Fraction Measurement Techniques

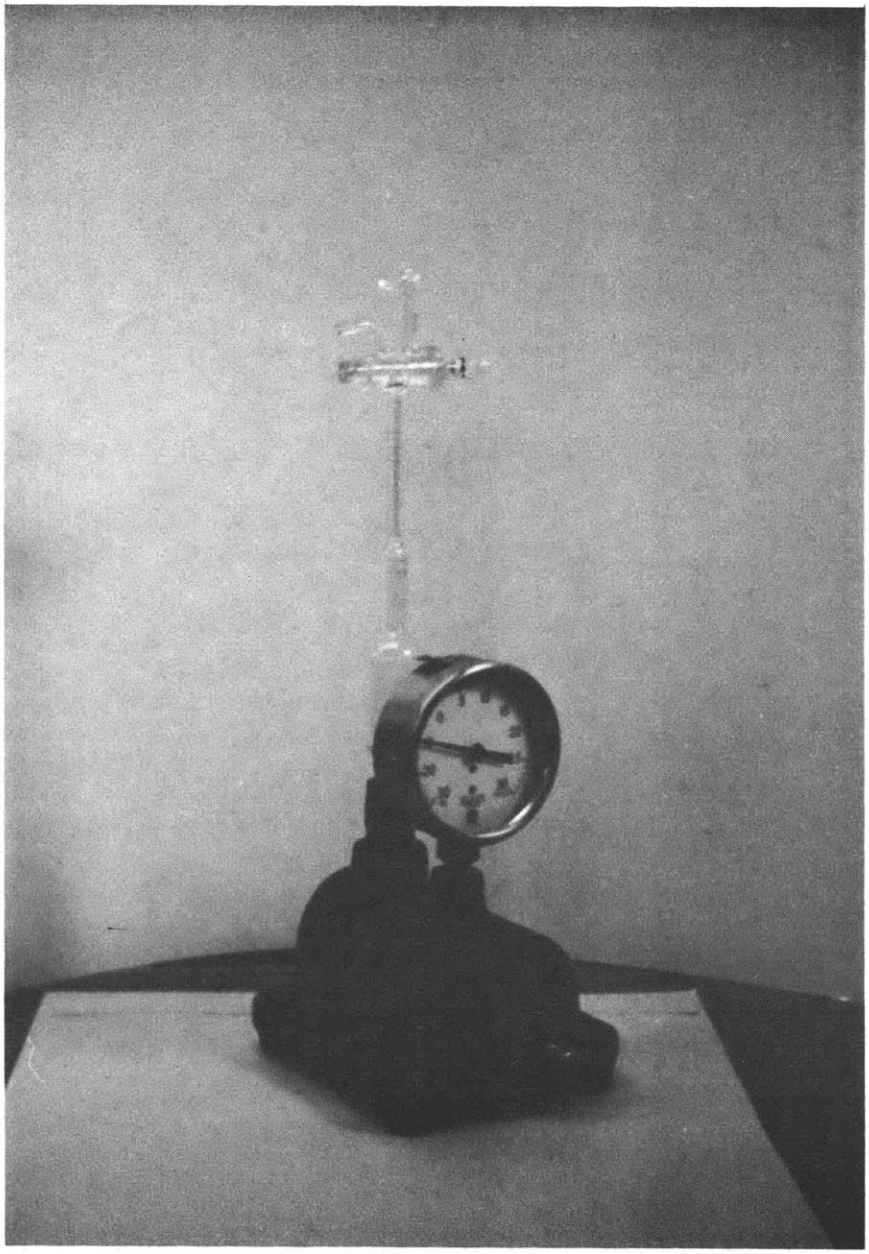

Figure 46. Photograph of the Seaton-Wilson Aire-Ometer Used for Determination of Dissolved Gas Content

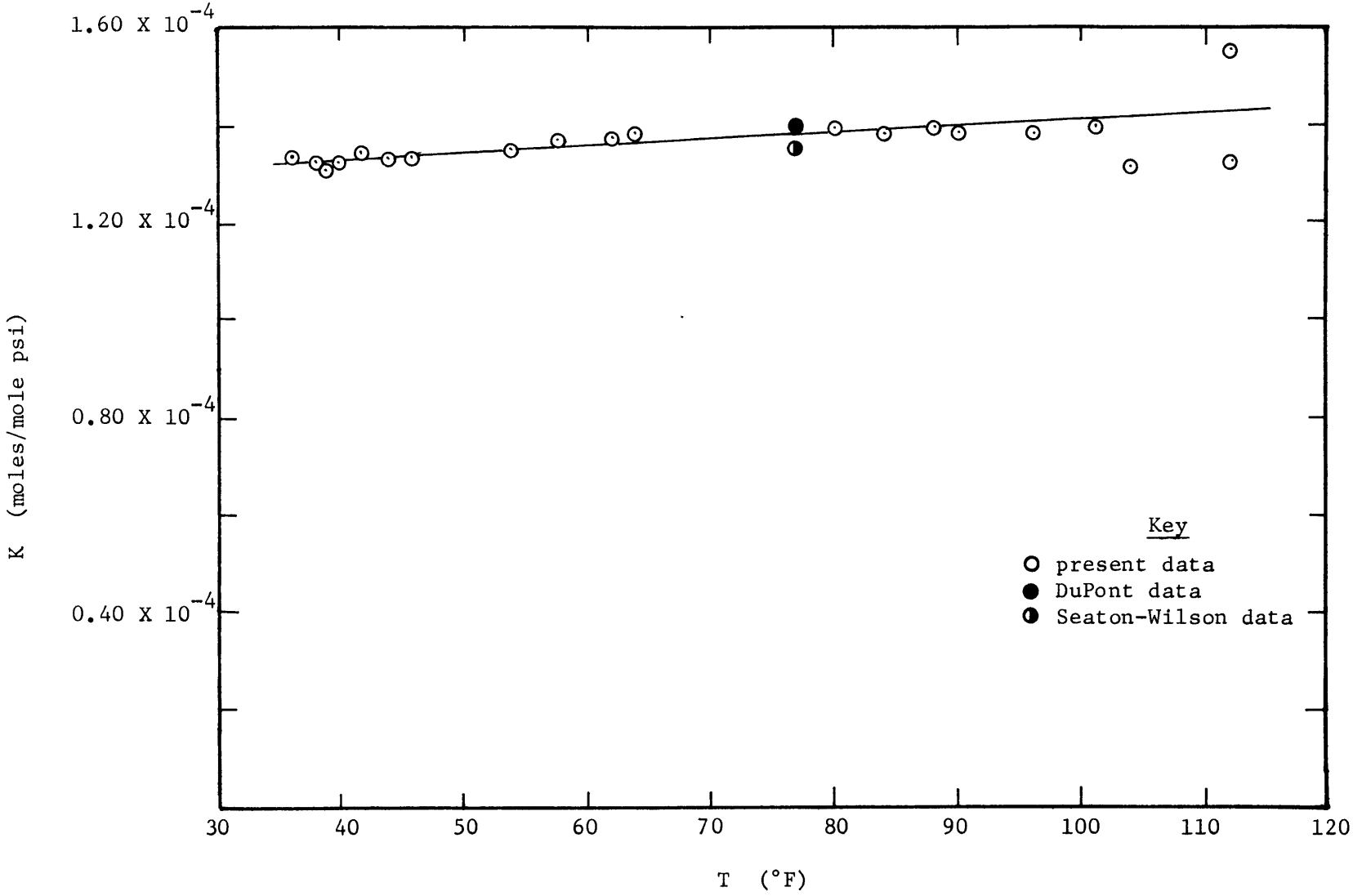

Figure 47. Temperature Dependence of Henry's Law Solubility Constant for Air in Freon-113

REFERENCES

1. Mouromtseff, I.E., "Water and Forced-Air Cooling of Vacuum Tubes," Proceedings of the Institute of Radio Engineers, Vol. 30, No. 4, pp. 190-205 (1942).

2. Levy, S., "Forced Convection Subcooled Boiling — Prediction of Vapor Volumetric Fraction," International Journal of Heat and Mass Transfer, Vol. 10, No. 7, pp. 951-965 (1967).

3. Staub, F.W., "The Void Fraction in Subcooled Boiling — Prediction of the Initial Point of Net Vapor Generation," Journal of Heat Transfer, Trans. ASME, Series C, Vol. 90, No. 1, pp. 151-157 (1968).

4. Corty, C., and A.S. Foust, "Surface Variables in Nucleate Boiling," Chemical Engineering Progress Symposium Series, Vol. 51, No. 17, pp. 1-12 (1955).

5. Haley, K.W., and J.W. Westwater, "Boiling Heat Transfer from Single Fins," Proceedings of the Third International Heat Transfer Conference, AIChE-ASME, Vol. III, pp. 245-253 (1966).

6. Armstrong, R.J., "The Temperature Difference in Nucleate Boiling," International Journal of Heat and Mass Transfer, Vol. 9, No. 10, pp. 1148-1149 (1966).

7. Danilova, G.N., "Correlation of Boiling Heat Transfer Data for Freons," Heat Transfer — Soviet Research, Vol. 2, No. 2, pp. 73-78 (1970).

8. Gouse, S.W., Jr., "The Evaporator Tube — State of the Art," M.I.T. Engineering Projects Laboratory Report No. DSR 8734-7 (1965).

9. Gouse, S.W., Jr., "Two-Phase Gas-Liquid Flow Oscillations: Preliminary Survey," M.I.T. Engineering Projects Laboratory Report No. DSR 8734-5 (1964).

10. Gouse, S.W., Jr., R.G. Evans, C.W. Deane, and J.D. Crowley, "Two-Phase Gas-Liquid Flow Dynamics: Part I - Flow Oscillations in Transparent, Parallel, Vertical, Heated Channels; Part II - Acoustic Velocity in Two-Phase Flow," M.I.T. Engineering Projects Laboratory Report No. DSR 74629-1 (1967).

11. Crowley, J.D., C.W. Deane, and S.W. Gouse, Jr., "Two-Phase Flow Oscillations in Vertical, Parallel, Heated Channels," Proceedings of the Symposium on Two-Phase Flow Dynamics, EURATOM, Vol. II, pp. 1131-1172 (1969).

12. Yadigaroglu, G., and A.E. Bergles, "An Experimental and Theoretical Study of Density-Wave Oscillations in Two-Phase Flow," M.I.T. Engineering Projects Laboratory Report No. DSR 74629-3 (1969).

13. Zuber, N., F.W. Staub, G. Bijwaard, and P.G. Kroeger, "Steady State and Transient Void Fraction in Two-Phase Flow Systems," Research and Development Center, General Electric Company, Report No. GEAP 5417, EURAEC 1949 (1967).

14. Crowley, J.D., and A.E. Bergles, "Fluid-to-Fluid Modeling of the Hydrodynamic Stability of Flow in Boiling Channels," ASME Paper 70-HT-28 (1970).

15. Barnett, P.G. and R.W. Wood, "An Experimental Investigation to Determine the Scaling Laws of Forced Convection Boiling Heat Transfer. Part 2: An Examination of Burnout Data for Water, Freon-12 and Freon-21 in Uniformly Heated Round Tubes," Report No. AEEW R-443 (1965).

16. Stevens, G.F., and R.V. Macbeth, "The Use of Freon-12 to Model Forced Convection Burnout in Water: The Restriction on the Size of the Model," ASME Paper 70-HT-20 (1970).

17. Dix, G.E., "Freon-Water Modeling of CHF in Round Tubes," ASME Paper 70-HT-26 (1970).

18. Baker, J.L.L., "Flow Regime Transitions at Elevated Pressures in Vertical Two-Phase Flow," Report No. ANL 7093 (1965).

19. Staub, F.W., G.E. Walmet, and R.O. Niemi, "Heat Transfer and Hydraulics — The Effects of Subcooled Voids," Research and Development Center, General Electric Company, Report No. NYO 3679-8, EURAEC 2120 (1969).

20. Bergles, A.E., N. Bakhru, and J.W. Shires, "Cooling of High-Power-Density Computer Components," M.I.T. Engineering Projects Laboratory Report No. DSR 70712-60 (1968).

21. Coumou, K.G., "An Investigation of Heat Transfer and Fluid Flow in a Horizontal Tube Evaporator," S.M. Thesis, M.I.T. Mechanical Engineering Department (1964).

22. Colombo, A., A. Hassid, and A. Premoli, "Steam-Water Mixture Density Measurements in Heated Channels at High Pressure by Means of a Quick-Closing Valve Method," Energia Nucleare, Vol. 15, No. 2, pp. 119-128 (1968).

23. Bergles, A.E., and W.M. Rohsenow, "Forced-Convection Surface Boiling Heat Transfer and Burnout in Tubes of Small Diameter," M.I.T. Engineering Projects Laboratory Report No. DSR 8767-21 (1962).

24. McAdams, W.H., Heat Transmission, Third Edition, McGraw-Hill (1954).

25. Deissler, R.G., "Turbulent Heat Transfer and Friction in the Entrance Regions of Smooth Passages," Trans. ASME, Vol. 74, No. 8, pp. 1221-1233 (1955).

26. Rohsenow, W.M., "A Method of Correlating Heat Transfer Data for Surface Boiling of Liquids," Trans. ASME, Vol. 74, No. 5, pp. 969-976 (1952).

27. Tong, L.S., Boiling Heat Transfer and Two-Phase Flow, John Wiley and Sons (1965).

28. Rohsenow, W.M., "Heat Transfer, A Symposium," Engineering Research Institute, University of Michigan (1952).

29. Gambill, W.R., "Generalized Prediction of Burnout Heat Flux for Flowing, Subcooled, Wetting Liquids," Chemical Engineering Progress Symposium Series, Vol. 59, No. 41, pp. 71-87 (1962).

30. Bernath, L., "A Theory of Local-Boiling Burnout and Its Application to Existing Data," Chemical Engineering Progress Symposium Series, Vol. 56, No. 30, pp. 95-116 (1960).

31. Hsu, Y.Y., and R.W. Graham, "An Analytical and Experimental Study of the Thermal Boundary Layer and Ebullition Cycle in Nucleate Boiling," NASA TN-D-594 (1961).

32. Bergles, A.E., and W.M. Rohsenow, "The Determination of Forced-Convection Surface-Boiling Heat Transfer," Journal of Heat Transfer, Trans. ASME, Series C, Vol. 86, No. 3, pp. 365-372 (1964).

33. Behar, M., M. Courtaud, R. Ricque, and R. Semeria, "Fundamental Aspects of Subcooled Boiling With and Without Dissolved Gases," Proceedings of the Third International Heat Transfer Conference, AIChE-ASME, Vol. IV, pp. 1-11 (1966).

34. Torikai, K., H. Shimamune, and T. Fujishiro, "The Effect of Dissolved Gas Content Upon Incipient Boiling Superheats," Preprints of Papers Presented at the Fourth International Heat Transfer Conference, Vol. V, Paper B 2.11 (1970).

35. Marto, P.J., and W.M. Rohsenow, "The Effect of Surface Conditions on Nucleate Pool Boiling Heat Transfer to Sodium," M.I.T. Engineering Projects Laboratory Report No. DSR 5219-33 (1965).

36. Bankoff, S.G., A.J. Hajjar, and B.B. McGlothin, Jr., "On the Nature and Location of Bubble Nuclei in Boiling from Surfaces," Journal of Applied Physics, Vol. 29, No. 12, pp. 1739-1741 (1958).

37. Hodgson, A.S., "Hysteresis Effects in Surface Boiling of Water," Journal of Heat Transfer, Trans. ASME, Series C, Vol. 91, No. 1, pp. 160-162 (1969).

38. Jordan, D.P., and G. Leppert, "Pressure Drop and Vapor Volume with Subcooled Nucleate Boiling," International Journal of Heat and Mass Transfer, Vol. 5, No. 6, pp. 751-761 (1962).

39. Jeglic, F.A., J.R. Stone, and V.H. Gray, "Experimental Study of Subcooled Nucleate Boiling of Water Flowing in 1/4-Inch-Diameter Tubes at Low Pressures," NASA TN-D-2626 (1965).

40. Ricque, R., and R. Siboul, "Ebullition Locale de l'Eau en Convection Forcée," Centre d'Etudes Nucléaires de Grenoble, Note TT No. 245 (1966).

41. McAdams, W.H., W.E. Kennel, C.S. Minden, R. Carl, P.M. Picornell, and J.E. Dew, "Heat Transfer at High Rates to Water with Surface Boiling," Industrial and Engineering Chemistry, Vol. 41, No. 9, pp. 1945-1953 (1949).

42. Pike, F.P., P.D. Miller, Jr., and K.O. Beatty, Jr., "Effect of Gas Evolution on Surfaces Boiling at Wire Coils," Chemical Engineering Progress Symposium Series, Vol. 51, No. 17, pp. 13-19 (1955).

43. Rohsenow, W.M., and H.Y. Choi, Heat, Mass, and Momentum Transfer, Prentice-Hall (1961).

44. Wallis, G.B., One-Dimensional Two-Phase Flow, McGraw-Hill (1969).

45. Florschuetz, L.W., and B.T. Chao, "On the Mechanics of Vapor Bubble Collapse," Journal of Heat Transfer, Trans. ASME, Series C, Vol. 87, No. 2, pp. 209-220 (1965).

46. Wittke, D.D., and B.T. Chao, "Collapse of Vapor Bubbles with Translatory Motion," Journal of Heat Transfer, Trans. ASME, Series C, Vol. 89, No. 1, pp. 17-24 (1967).

47. Isenberg, J., and S. Sideman, "Direct Contact Heat Transfer with Change of Phase: Bubble Condensation in Immiscible Liquids," International Journal of Heat and Mass Transfer, Vol. 13, No. 6, pp. 997-1011 (1970).

48. Bergles, A.E., and T. Dormer, Jr., "Subcooled Boiling Pressure Drop with Water at Low Pressure," International Journal of Heat and Mass Transfer, Vol. 12, No. 4, pp. 459-470 (1969).

49. Gouse, S.W., Jr., "Void Fraction Measurement," M.I.T. Engineering Projects Laboratory Report No. DSR 8734-2 (1964).

50. Downing, R.C., "Solubility of Inert Gases in the Liquid Phase of Freon Compounds," E.I. DuPont de Nemours and Company, Technical Bulletin No. B-14B (1967).

51. Huffman, J., "Technical Data from Aire-Ometer Measuring Device," Seaton-Wilson, Incorporated, Manual AD-4002 (1970).

52. Downing, R.C., "Transport Properties of Freon Fluorocarbons," E.I. DuPont de Nemours and Company, Technical Bulletin No. C-30 (1967).

53. Benning, A.F., and R.C. McHarness, "Thermodynamic Properties of Freon-113 (Trichlorotrifluoroethane)," E.I. DuPont de Nemours and Company, Technical Bulletin No. T-113A (1938).

54. Fischer and Porter Company, "Variable Area Flowmeter Handbook, Volume II — Rotameter Calculations," Catalog 10A1022 (1968).

55. Hynek, S.J., W.M. Rohsenow, and A.E. Bergles, "Forced-Convection Dispersed-Flow Film Boiling," M.I.T. Engineering Projects Laboratory Report No. DSR 70586-63 (1969).

56. Leeds and Northrup Company, "Conversion Tables for Thermocouples," No. 077989, Issue 4 (1965).

57. Schlicting, H., Boundary Layer Theory, Fourth Edition, McGraw-Hill (1960).